IMAGE SEGMENTATION BASED ON VARIATIONAL TECHNIQUES

A THESIS SUBMITTED TO
THE GRADUATE SCHOOL OF NATURAL AND APPLIED SCIENCES
OF
THE MIDDLE EAST TECHNICAL UNIVERSITY

BY

METİN BURAK ALTINOKLU

IN PARTIAL FULFILLMENT OF THE REQUIREMENTS
FOR
THE DEGREE OF MASTER OF SCIENCE
IN
ELECTRICAL AND ELECTRONICS ENGINEERING

FEBRUARY 2009

Approval of the thesis:

IMAGE SEGMENTATION BASED ON VARIATIONAL TECHNIQUES

submitted by **METİN BURAK ALTINOKLU** in partial fulfillment of the requirements for the degree of **Master of Science in Electrical and Electronics Engineering** by,

Prof. Dr. Canan Özgen
Dean, Graduate School of **Natural and Applied Sciences** _____

Prof. Dr. İsmet Erkmen
Head of Department, **Electrical and Electronics Engineering** _____

Prof. Dr. Zafer Ünver
Supervisor, **Electrical and Electronics Engineering Dept., METU** _____

Prof. Dr. Kemal Leblebicioğlu
Co-Supervisor, **Electrical and Electronics Engineering Dept., METU** _____

Examining Committee Members:

Prof. Dr. Mete Severcan
Electrical and Electronics Engineering Dept., METU _____

Prof. Dr. Zafer Ünver
Electrical and Electronics Engineering Dept., METU _____

Prof. Dr. Kemal Leblebicioğlu
Electrical and Electronics Engineering Dept., METU _____

Assoc. Prof. Dr. Aydın Alatan
Electrical and Electronics Engineering Dept., METU _____

Assoc. Prof. Dr. Sibel Tarı
Computer Engineering Dept., METU _____

Date: 10.02.2009

I hereby declare that all information in this document has been obtained and presented in accordance with academic rules and ethical conduct. I also declare that, as required by these rules and conduct, I have fully cited and referenced all material and results that are not original to this work.

Name, Last name : Metin Burak Altınoklu

Signature :

ABSTRACT

IMAGE SEGMENTATION BASED ON VARIATIONAL TECHNIQUES

Altınoklu, Metin Burak

M.S., Department of Electrical and Electronics Engineering

Supervisor : Prof. Dr. Zafer Ünver

Co-Supervisor: Prof. Dr. Kemal Leblebicioğlu

February 2009, 115 pages

In this thesis, the image segmentation methods based on the Mumford–Shah variational approach have been studied. By obtaining an optimum point of the Mumford-Shah functional which is a piecewise smooth approximate image and a set of edge curves, an image can be decomposed into regions. This piecewise smooth approximate image is smooth inside of regions, but it is allowed to be discontinuous region wise. Unfortunately, because of the irregularity of the Mumford Shah functional, it cannot be directly used for image segmentation. On the other hand, there are several approaches to approximate the Mumford-Shah functional. In the first approach, suggested by Ambrosio-Tortorelli, it is regularized in a special way. The regularized functional (Ambrosio-Tortorelli functional) is supposed to be gamma-convergent to the Mumford-Shah functional. In the second approach, the Mumford-Shah functional is minimized in two steps. In the first minimization step, the edge set is held constant and the resultant functional is minimized. The second minimization step is about updating the edge set by using level set methods. The second approximation to the Mumford-Shah functional is known as the Chan-Vese method. In both approaches, resultant PDE equations (Euler-Lagrange equations of associated functionals) are solved

by finite difference methods. In this study, both approaches are implemented in a MATLAB environment. The overall performance of the algorithms has been investigated based on computer simulations over a series of images from simple to complicated.

Keywords: Image segmentation, variational techniques, Mumford-Shah functional, image smoothing, level set methods, texture segmentation, diffusion filters, curve evolution.

ÖZ

DEĞİSİMSEL TEKNİKLERE DAYALI GÖRÜNTÜ BÖLÜTLEME

Altınoklu, Metin Burak

Yüksek Lisans, Elektrik ve Elektronik Mühendisliği Bölümü

Tez Yöneticisi : Prof. Dr. Zafer Ünver

Ortak Tez Yöneticisi: Prof. Dr. Kemal Leblebicioğlu

Şubat 2009, 115 sayfa

Bu tezin konusu, Mumford-Shah fonksiyonelini temel alan yöntemlerle görüntü bölütleme problemini çözmektir. Mumford-Shah enerji fonksiyonelinin parçalı pürüzsüz görüntü fonksiyonu ve kenar kümesine göre enazlanmasıyla, görüntü çeşitli bölgelere ayrılır. Parçalı pürüzsüz görüntü fonksiyonu, bölge içlerinde pürüzsüzdür fakat farklı bölgeler arasında kesintilidir. Ne yazık ki, Mumford-Shah fonksiyoneli düzenli olmadığı için, doğrudan görüntü bölütleme problemine uygulanamaz. Öte yandan, Mumford-Shah fonksiyoneline yaklaşamaya dayalı iki ayrı yöntemle görüntü bölütleme problemi çözülebilir. Birinci yöntem, Mumford-Shah fonksiyoneli yerine ona gamma yaklaşan düzenli bir fonksiyonel olan Ambrosio-Tortorelli fonksiyonelini kullanmaktır. Chan-Vese yötemi olarak bilinen ikinci yöntem ise, Mumford-Shah fonksiyonelini iki aşamada enazlayamaya dayanır. İlk enazlama adımında, kenar kümesi sabit tutularak, parçalı pürüzsüz görüntü fonksiyonuna göre enazlama yapılır. İkinci enazlama adımında ise, seviye kümeleri yöntemiyle kenarlara göre fonksiyonel enazlanır. Sonlu fark şemaları ile elde edilen kısmi türevsel denklemler (fonksiyonellerin Euler-Lagrange denklemleri) çözülür. Bu tez çalışmasında, her iki yöntem için de MATLAB ortamında yazılım geliştirilmiştir. Bilgisayarda yapılan benzetim çalışmalarıyla, hem basit

görüntüler için hem de karmaşık görüntüler için algoritmaların genel başarımı sınanmıştır.

Anahtar Kelimeler: Görüntü bölütleme, değişimsel teknikler, Mumford-Shah fonksiyoneli, görüntü yumuşatma, seviye kümesi yöntemleri, difüzyon süzgeçleri, eğri evrimi.

ACKNOWLEDGMENTS

I would like to express my sincere gratitude to my supervisor Prof. Dr. Zafer ÜNVER and my co-supervisor Prof. Dr. Kemal LEBLEBİCİOĞLU for their supervision, guidance and encouragement throughout this study.

Special thanks goes to my mother for her love and support throughout my life. I would like to thank all members of my family for supporting me.

I am indebted to all of my friends and colleagues for their support and encouragements. Finally, I would like to thank to the members of Computer Vision and Intelligent Systems Laboratory, namely, Erdem Akagündüz, Tülay Akbey, Yasemin Özkan Aydın, Örsan Aytekin, Ömer Eskizara, Neslihan Özmen and Mehmet C. Yılmaztürk.

This work is partially supported by the TÜBİTAK-BAYG M.Sc. scholarship program.

dedicated to the memory of my father

TABLE OF CONTENTS

LIST OF FIGURES

FIGURES

CHAPTER 1

INTRODUCTION

Image segmentation is a fundamental problem of low level image processing. It is the process of decomposing an image into areas corresponding to different objects in the observed scene. In high level image processing applications, the accuracy of image segmentation step is very critical. Some application areas of image segmentation are medical imaging, thermal imaging, locating objects in satellite images (roads, forests, etc.), face recognition, automated detection of targets in synthetic aperture radar imagery, and machine vision.

Edge detection by local derivatives of intensity is a naive way to perform image segmentation. The primary difficulty in edge detection is that image smoothing dislocates the edges but without image smoothing it is very hard to determine the edges due to noise. In addition, edge detection algorithms do not enclose the objects in the image by closed contours. In the last 25 years, computer vision community has produced a number of sophisticated segmentation methods. Geman and Geman [1] suggested an efficient image segmentation method via Markov random field model based discrete energy functional minimization. In this approach, an image is segmented concurrently with image smoothing. Later, Mumford-Shah [2] put the energy of Geman and Geman into a continuous form. Another efficient image segmentation technique is the graph-based *normalized cuts* method [3] that uses approximate spectral analysis techniques.

This thesis is focusing its attention on variational and partial differential equations (PDEs)-based image segmentation techniques. In a variational approach, image segmentation problem is posed in the form of minimizing an energy functional. The minimizer of the energy functional is given by a differential equation

(the Euler-Lagrange equation). One can try to find a local minimum of this energy functional by applying steepest decent algorithm in the distributed sense. The resultant set of PDE equations can be solved approximately using finite difference schemes.

One of the useful variational methods for localizing objects in the image is *classical active contour (snakes)* method of Kaas et al [4]. By this technique, a closed curve called the *Active Contour* is evolved until it encloses the object in the image. The evolution of the active contour is based on the minimization of a boundary-based energy functional which consists of three terms. The external term measures how near the curve is located to the vicinity of high image gradients. The two internal energy terms measure the smoothness of the closed curve. However, there are some limitations of the classical active contour method like poor convergence into boundaries of non-convex objects and dependency on initial contour placement. In order to overcome these difficulties, an extension of classical active contour technique known as the *gradient vector flow* (GVF) method [5] has been proposed. In the GVF method, the external energy term is replaced with a GVF field which is equal to edge map when gradient is large, but it is forced to be slowly varying in homogeneous regions. These approaches are also known as *parametric active contour methods* since the contour curve is represented explicitly in a parametric form and the snake is composed of a set of control points. The main disadvantages of parametric active contours are dependency on the parametrization and impossibility to handle topology changes.

The level set method (LSM) invented by Osher and Sethian [6] is a powerful numerical technique for capturing boundaries or tracking interfaces. An active contour method implemented by the level set methods is called geometric active contour method. Curves are represented by embedding them as the zero level set of a two-dimensional auxiliary level set function. Implementation of the level set methods is quite easy and topology changes are automatically handled. The main disadvantage of level set methods is the increased computational time. Therefore, it can be advantageous to use parametric active contour methods in real time

applications. Furthermore, computational complexity of the level set methods can be decreased by so called narrow band algorithms in which a closed curve is evolved only on regions whose level set function value stays in a narrow band around the closed curve. An example of geometric active contour methods is the *geodesic active contour* method [7], where the curve length is defined in a different way: it is weighted by an edge detector function.

The main variational model for image segmentation is the *Mumford-Shah(MS) model* in which image smoothing is done simultaneously with image segmentation. The MS model approximates the original image with a piecewise smooth function and boundary set such that the original image is decomposed into homogeneous regions in terms of intensity. This piecewise smooth function varies smoothly in each sub domain but it is allowed to be discontinuous from domain to domain. It is a new *cartoon* image with edges drawn sharply and the objects are drawn smoothly without texture. Such cartoons are perceived correctly as a simplification of the scene containing most of its essential features. The aim of the MS model can be achieved by minimizing the MS functional which consists of three terms. The first term measures how well the piecewise smooth function approximates the original function. The second term measures the smoothness of the piecewise smooth function in each sub domain. The third term requires that the length of the edge set should be as short as possible. The MS model is a region-based model since the terms in the MS functional integrate certain quantities over the whole image domain to control the evolution of the curve. Being a region-based model, there are some advantages of using the MS model in image segmentation like robustness with respect to noise and initial contour placement; as opposed to the boundary-based active contour methods which depend only on local gradient information to stop the curve evolution.

The MS functional is irregular due to the existence of unknown edge set of lower dimension thus one cannot obtain the Euler-Lagrange equation directly. There are two approaches to obtain an approximation of the MS functional.

In the first approach, the MS functional is minimized in a two step procedure. The first step consists of minimizing the MS functional with respect to the piecewise smooth approximating function while holding the edge set fixed. In the second step, the piecewise smooth function is fixed but the closed curve is updated by level set methods. After the first step, in each region optimal estimation PDEs are obtained. Solving these PDE equations, a piecewise smooth approximation to the original image is obtained in each sub-domain. There are two ways for minimization of the MS functional with respect to boundary set. The first way is called the *Chan-Vese(CV) method* which is based on a variational formulation in terms of level sets [8]. The second way is the method proposed by Tsai. et. al., which finds the curve evolution equation by computing the first variation of a MS like functional and then derives the curve evolution PDEs in terms of level set function [9]. Even though both ways are quite similar, rather than using the piecewise smooth MS model as in [9], in the CV model a piecewise constant approximating term is constructed. In the piecewise constant model, approximating term is assumed to be constant in each region and the optimal constants are given by intensity means in the corresponding regions. Piecewise constant model simplifies the implementation of the problem and reduces the computational cost. In [9], it is noted that detecting objects with different intensity sub regions is easier by using the piecewise smooth model. However, the piecewise smooth version of CV model and the piecewise constant version of Tsai et. al.'s model, are also proposed in [10] and [9], respectively. If the same versions of both methods are used, the only difference between them is that the Dirac function used in the CV method is replaced with the magnitude of the gradient function in Tsai et. al.'s method. For segmentation of images with two regions with separate intensities only one level set is needed. This is known as the two-phase approach. Two-phase approach is not successful for segmentation of complex images with more than two regions. Multiphase level set method proposed in [10] or hierarchical approaches proposed in [9, 11] should be used for segmentation of these type of images. In the multiphase approach, multiple level sets are used and a region is represented

by a vector holding signs of level set functions. It decomposes the image into an arbitrary number of regions in such a way that no neighbouring regions receive the same vector. In a four–phase segmentation, two level set functions are used. Theoretically, two level set functions are enough to segment the image into an arbitrary number of regions. The reason behind that is the Four Color Theorem. In the hierarchical approaches, image is segmented into two regions; these regions are further segmented if necessary, in a recursive way.

Second approach consists of using Γ- convergence framework [12] to approximate the MS functional by a regular functional in which the edge set is represented by a boundary function of the same type as the image function. The most well-known such functional is the *Ambrosio-Tortorelli(AT) functional* introduced in [13]. In the AT functional, unknown edge set is represented by a boundary function taking values between zero and one such that at the edges boundary function is near zero and otherwise it is near one. Since the AT functional is regular, the coupled PDE equations which minimize the AT functional with respect to image and boundary functions can be obtained by standard variational techniques.

The MS model segments images based on the piecewise smoothness assumption: distinct objects have different mean intensities. The main limitation of the MS model is that an image is accurately segmented only if piecewise smoothness assumption holds. This assumption generally holds for medical images. However, methods based on the MS model are not applicable to the segmentation of some textured natural images, for which piecewise smoothness assumption does not hold.

Another limitation of the MS model is the elimination of textural part of the image by smoothing. The model assumes that noise corresponds to the high-frequency part and the denoised image is piecewise smooth. However, this assumption fails for textured natural images, e.g., textures are as oscillatory as the noise. As a result, the texture is wiped out by the MS image smoothing and segmentation model. In order to overcome these problems, texture-preserving denoising models are suggested are based on the Rudin-Osher-Fatemi (ROF) [14]

image denoising model which consists of data fidelity and smoothness terms. Recently, some methods [15, 16] are developed by replacing the L_2 norm in data fidelity term of the ROF model with suitable norms for describing the textural part. These methods denoise the image with texture preservation by decomposing the image into three parts: cartoon representation of the original image, textural part and noise. A different variational formulation for texture-preserving denoising has been proposed in [17]. In this formulation, spatially varying fidelity term controls the extent of denoising over image regions based on local variance measures.

Another possibility for image smoothing is to use a PDE-based method which starts directly with a PDE equation without considering any energy functional. The oldest example of PDE-based methods is the linear diffusion filtering in which the image is smoothed linearly with heat equation. In fact, this procedure is almost equivalent to linear Gaussian filtering. In nonlinear diffusion filtering, smoothing is space dependent such that image is smoothed in each homogeneous region but smoothing is inhibited at edges. In isotropic nonlinear diffusion [18, 19] edges are detected only by magnitude of gradient, but in anisotropic nonlinear diffusion [20, 21] gradient orientation is also taken into account for edge detection. Interestingly, idea and performance of nonlinear diffusion filters are very similar to optimal estimation PDEs in the active contour implementations of the MS model.

In this thesis, mainly image segmentation methods based on the MS model are studied. The MS active contour methods are tested using noisy synthetic images and lowly textured natural images. These images are successfully segmented. However, applying the CV active contour method to some highly textured natural images does not give us satisfactory results. In this case, using nonlinear diffusion as a pre-filtering scheme in the CV active model, textured images which can be separated by intensity variation is accurately segmented. Unfortunately, pre-filtering scheme did not help segmentation of textured images which does not consist of objects with distinct mean intensities. In addition, some segmentation

experiments with Gabor-based extensions of the CV model [22] and the geodesics active contour model [23] are done on textured images. In the former case, segmentation results are unsatisfactory, but in the latter case, satisfactory results are obtained. The other effective approximation of the MS model, namely the AT model is also studied. Experiments show that using the intensity homogeneity requirement is not sufficient for segmentation of the textured images. In order to obtain better segmentation results for textured and noisy images, a modification is proposed by treating the edge and image function as states and adding feedback terms to right hand side of the AT PDE equations. However, we did not get satisfactory results and we concluded that unless constructing the feedback term using a higher level information than simply the image gradient, this operation does not bring better results.

The work is organized as follows. In Chapter 2, the MS functional is analyzed. In Chapter 3, implementation of the MS model by active contour methods is investigated and some results are shown. In chapter 4, image smoothing by diffusion filters is analyzed and experimental results are shown. In chapter 5, textured image segmentation by active contour methods and their extensions is analyzed and the results are shown. In Chapter 6, the AT model is analyzed and some experimental results are shown. Finally, in Chapter 7, the conclusions are provided.

CHAPTER 2

MUMFORD-SHAH FUNCTIONAL

Let u_0: $\Omega \rightarrow \mathbb{R}$ denote the given gray level image where $\Omega \subset \mathbb{R}^2$ denotes the domain of the given image. The solution of the image segmentation problem can be found by the minimization of the MS functional that constructs a piecewise smooth approximation of u_0. The piecewise smooth function (u) can be modeled by a set of smooth functions defined on a set of disjoint regions Ω_i covering Ω. Each disjoint region has a piecewise smooth boundary. The edge set of image $\Gamma \subset \Omega$ is given by entire boundary of Ω_i's inside Ω. The image domain Ω is decomposed into m regions and the boundary set by $\Omega = \Omega_1 \cup ... \cup \Omega_m \cup \Gamma$ such that u varies smoothly within each region Ω_i but it is allowed to be discontinuous across boundaries of Ω_i inside Ω. The pair (u, Γ) can be interpreted as a *cartoon* of actual image in which edges are drawn sharply and precisely and the objects surrounded by edges are drawn smoothly without textures [2]. Image segmentation is achieved by finding the pair (u, Γ) which minimizes the MS functional given in equation 2.1.

$$E_{MS}(u, \Gamma) = \beta \int_{\Omega} (u - u_0)^2 dxdy + \alpha \int_{\Omega \setminus \Gamma} |\nabla u|^2 dxdy + \nu |\Gamma| \tag{2.1}$$

The first term of the MS functional measures how well the u fits u_0. The second term measures the piecewise smoothness of u in each Ω_i. The third term requires that the length of edge set $|\Gamma|$ should be as short as possible. If any of the three terms is omitted, then trivial solutions are obtained. The pair (u, Γ) give the solution of image segmentation problem only if all three terms are kept. The entities in the MS functional are weighted by the non-negative parameters

α, β and ν. The larger the parameter of any term in the MS functional, the more that term accomplishes its aim. Of course, one of these three parameters can be set to 1.

The two optimization variables are of different kind. The first variable u belongs to $B(\Omega \setminus \Gamma)$(appropriate Banach space of functions defined on $\Omega \setminus \Gamma$). Edge set Γ is removed from the domain of integration for the second integral allowing u to be discontinuous across boundaries of Ω_i inside Ω. For Γ, there is not an underlying Banach space structure as noted by [24].

The minimization of the MS functional is not straightforward. Since the domain of integration is defined on $\Omega \setminus \Gamma$, standard methods of the calculus of variations cannot be applied directly. However, by holding Γ fixed, the functional can be minimized with respect to u and the differential equation that u satisfies on $\Omega \setminus \Gamma$ can be found by standard variational techniques. Let δu represent a function of the same type as u. Then,

$$E_{MS}(u + t\delta u, \Gamma) - E_{MS}(u, \Gamma) = t\left[\beta \int 2\delta u \cdot (u - u_0)\, dxdy + \alpha \int 2\left(\nabla u \cdot \nabla \delta u\right) dxdy\right] + t^2\left[\beta \int (\delta u)^2\, dxdy + \alpha \int \|\nabla \delta u\|^2\, dxdy\right]$$

Therefore,

$$\begin{aligned}\frac{\delta E}{\delta u}(u, \Gamma) &= \lim_{t \to 0} \frac{E_{MS}(u + t\delta u, \Gamma) - E_{MS}(u, \Gamma)}{t} \\ &= \beta \int 2\delta u \cdot (u - u_0)\, dxdy + \alpha \int 2\left(\nabla u \cdot \nabla \delta u\right) dxdy\end{aligned}$$

By Green's formula [12], $\int \left(\nabla u \cdot \nabla \delta u\right) dxdy = -\int \left(\nabla^2 u \cdot \delta u\right) dxdy + \int_B \delta u \frac{\partial u}{\partial n} ds$ where B is the entire boundary of $\Omega \setminus \Gamma$, i.e., $\partial\Omega$ and each side of Γ. Outer normal to the boundary B is denoted by n. Thus we obtain

$$\frac{1}{2}\frac{\delta E_{MS}}{\delta u}(u, \Gamma) = \int \delta u \left(\beta (u - u_0) - \alpha \nabla^2 u\right) dxdy + \int_B \alpha \delta u \frac{\partial u}{\partial n} ds.$$

Taking δu as a test function which is non-zero near one point of $\Omega \setminus \Gamma$, zero elsewhere taking limit over such δu, we obtain optimal estimation PDEs that u satisfies on $\Omega \setminus \Gamma$ given in equation 2.2.

$$\nabla^2 u = \frac{\beta}{\alpha}(u - u_0) \tag{2.2}$$

Now, taking δu to be nonzero near one point of B and zero elsewhere, taking limit over such δu, we obtain Neumann boundary conditions on $\partial\Omega$ and two sides of Γ given in equation 2.3.

$$\frac{\partial u}{\partial n} = 0 \tag{2.3}$$

Finding the differential equation that u satisfies on $\Omega \setminus \Gamma$ eliminates u from the functional, then next step is to minimize functional with respect to the edge set Γ. But this is not possible by standard optimization methods since there is no underlying Banach space structure for Γ. Minimizing the MS functional with respect to Γ with u fixed is a *shape optimization* problem. The problem can be solved by evolving the boundary with level set methods which is an effective numerical technique for tracking shapes.

There is another possibility for the numerical minimization of the MS functional by modifying it into a form in which Γ does not appear explicitly. A popular example is the approximation of the MS functional by elliptic functionals obtained by [13]. In this approximation, the edge set is approximated in terms of a functional variable, $v \in B(\Omega)$ which takes values between zero and one. This variable depends on a parameter ρ such that the elliptic functional Γ- converges to E_{MS} as $\rho \to 0$. Since this functional is regular, standard variational techniques are applicable.

In order to simplify the implementation of the MS method, a reduced (piecewise constant) MS model is also proposed in [2]. In this model, the image u is equal to constant a_i in the ith region. The reduced MS model is given in equation 2.4.

$$E_{MS,reduced}(u,\Gamma) = \sum_i \beta_i \int_{\Omega_i} (u - a_i)^2 \, dxdy + +\nu|\Gamma| \tag{2.4}$$

It is straightforward to see that reduced MS functional is minimized when $a_i = \frac{\int_{\Omega_i} u dxdy}{|\Omega_i|}$.

CHAPTER 3

MUMFORD-SHAH ACTIVE CONTOUR METHOD

Even though, the MS model is an effective model for image segmentation, minimization of it is not straightforward as discussed in Chapter 2. Recently, active contour techniques are used for the implementation of the MS model for image segmentation by Chan-Vese in [8] and Tsai. et. al. in [9]. The aim of active contour methods is object detection in images, by curve evolution. Starting from an initial curve, the active contour moves toward the object based on a energy minimization until it encloses the object and it partitions the image into two regions: "object" and background". In this chapter, these techniques are reviewed and some implementation results are shown.

The active contour methods are developed by the original work of Kass et. al in [4]. In these methods, a curve is evolved to minimize the boundary-based snake energy which consists of internal and external energy terms. The curves are located near high image gradients, i.e., edges by external energy term and the curves are smoothed by internal energy terms. However, there are some limitations of boundary-based active contour methods. Main limitation of the boundary based active contour methods is that, one must place the starting curve near the object to be detected; otherwise the active contour cannot enclose the object. In addition, it is very hard to extract objects with smooth or discontinuous boundaries; since discrete gradients are bounded and the external energy term is not always minimized at the edges of these objects.

The CV active contour model is a region based active contour model, since it is the implementation region-based MS image segmentation model within a level set framework. Since the CV active contour method is less local than edge-based

active contours, it is less dependent on the starting curve. In addition, having the property that its stopping criterion is not dependent on image gradients, it is possible to extract objects with smooth or discontinuous boundaries with the CV active contour method.

3.1 LEVEL SET METHOD

Implementation of the curve evolution PDE equations of the MS active contour models are done by the level set method which is proposed in [6] for capturing boundaries or tracking interfaces. An active contour model implemented by the level set method is called geometric or implicit active contour model, since the curve Γ is represented implicitly by the zero level set of a scalar Lipschitz continuous function $\phi(x, y) : \overline{\Omega} \rightarrow \mathbb{R}$ where $\Omega \subset \mathbb{R}^2$. The level set function $\phi(x, y)$ satisfies the following:

$$\begin{aligned} \phi(x,y) > 0 \, in \, \omega (inside \, of \, \Gamma) \\ \phi(x,y) < 0 \, in \, \Omega \setminus \overline{\omega} (outside \, of \, \Gamma) \\ \phi(x,y) = 0 \, on \, \partial\omega, (\partial\omega = \Gamma) \end{aligned} \tag{3.1}$$

The curve is represented by a auxiliary level set function holding 3.1. In the numerical implementations, level set function is initialized as a signed Euclidean distance to the curve since this level set function evolves fast. Signed distance functions can be created by using MATLAB function bwdist.

There are two ways of finding the partial differential equation that evolves the level set. In the first way, the curve evolution equation is found by calculus of variations and it is transformed it into a level set equation as done in [9]. In the second way (the CV Method), the PDE equation is found by formulating a energy functional that involves the level set function and by solving the Euler-Lagrange equations which minimizes this functional with a gradient descent technique.

Until convergence, the level-set evolution equations are solved. The curve is found by solving $\Gamma = \{(x, y)|\phi(x, y) = 0\}$ only after the convergence of the algorithm.

The advantage of the level set method is that topological changes in the curve are easily performed. Also, one can perform numerical computations without contour parametrization and control point regridding which are needed in parametric active contour models. The main disadvantage of level set method is the increased computational cost due to representation of the edge set by a two-dimensional function $\overline{\Omega} \rightarrow \mathbb{R}$.

3.2 CHAN-VESE METHOD

There are two different CV models. The first model which is known as the piecewise constant CV model [8] is equivalent to the reduced MS model. The second model which is known as the piecewise smooth CV model [10] is equivalent to the MS model.

3.2.1 Piecewise Constant Chan-Vese Model

The MS functional is given in equation 2.1. The piecewise constant CV model is equivalent to the reduced MS model which is obtained as follows: u is restricted to be constant in the regions. Optimally, value of u in the i^{th} region is given by mean of u_0 (c_i) in that region. The CV energy functional is proposed in [8, 10] and it is given in equation 3.2. The CV functional has two terms, one term measures how well c_i approximates u in region i and second term is a length penalty term which keeps the curve length short. Since the optimal estimates of u in each region is computed by averaging at every iteration, smoothing term $\alpha \int_{\Omega \setminus \Gamma} |\nabla u|^2 dx$ in the MS functional is omitted. The parameters are, β_i for i^{th} phase $|u - c_i|^2$ term, ν for the length term and they are fixed to a suitable value experimentally.

$$E_{CV}(u, \Gamma) = \sum_i \int_{\Omega_i} \beta_i |u - c_i|^2 dxdy + \nu|\Gamma| \tag{3.2}$$

3.2.1.1 Two-Phase Piecewise Constant Chan-Vese Model

In the two-phase piecewise constant CV model, two segments (phases) are represented by one level function. This model is only suitable for images that do not contain triple junctions. In this simple case, the image domain is partitioned into two open sets ω (inside of the curve) and $\Omega \setminus \overline{\omega}$ (outside of the curve). u is equal to mean of the pixel values (c_1) on ω and it is equal to mean of the pixel values (c_2) on $\Omega \setminus \overline{\omega}$. Keeping the length term in the functional, the two-phase piecewise constant CV functional is given by

$$E_{CV_2}(c_1, c_2, \Gamma) = \int_{\omega} |u_0 - c_1|^2 dxdy + \int_{\Omega \setminus \omega} |u_0 - c_2|^2 dxdy + \nu|\Gamma|. \tag{3.3}$$

Numerical minimization of this functional is implemented via the level set method. The curve Γ is represented implicitly by the zero level set of a scalar function $\phi(x, y)$ which is given by:

$$\phi(x, y) > 0 \; in \; \omega (inside \; of \; \Gamma)$$
$$\phi(x, y) < 0 \; in \; \Omega \setminus \overline{\omega} (outside \; of \; \Gamma)$$
$$\phi(x, y) = 0 \; on \; \partial\omega, (\partial\omega = \Gamma)$$

When represented by level set function ϕ, the CV energy is equivalent to

$$E_{CV_2}(c_1, c_2, \Gamma) = \int_{\phi>0} |u_0 - c_1|^2 dxdy + \int_{\phi<0} |u_0 - c_2|^2 dxdy + \nu|\Gamma|. \tag{3.4}$$

Using Heaviside function H as a characteristics function where $H(z) = 1$ if $z > 0$ and $H(z) = 0$ otherwise, the functional is expressed in a different form. In this form, the domain of integration is Ω as given in equation 3.5.

$$\int_{\phi>0} |u_0 - c_1|^2 dxdy = \int_{\Omega} |u_0 - c_1|^2 H(\phi) dxdy \tag{3.5}$$

In distributional sense, the curve length term of the functional is represented by $|\Gamma| = \int_\Omega |\nabla H(\phi)| = \int_\Omega \delta(\phi)|\nabla\phi|$. In order to get a numerical implementation, all terms of the functional should be Gateaux differentiable (see Appendix A). Therefore, undifferentiable Heaviside and Dirac functions in the CV functional should be replaced by C^1 approximations H_ϵ and δ_ϵ. Regularized versions of Heaviside and Dirac functions are given in equations 3.6 and 3.7, respectively. If the parameter ϵ is chosen as $h = 1$, then the Dirac and Heaviside functions shown in Figure 3.1 are obtained. The differentiable two-phase piecewise constant CV functional is given in equation 3.8.

$$H_\epsilon(x) = \frac{1}{2}\left[1 + \frac{2}{\pi} arctan\left(\frac{x}{\epsilon}\right)\right] \tag{3.6}$$

$$\delta_\epsilon(x) = H'_\epsilon(x) = \frac{1}{\pi}\frac{\epsilon}{\epsilon^2 + x^2} \tag{3.7}$$

$$\begin{aligned} E_{CV_2}(c_1, c_2, \Phi) = & \int_\Omega |u_0 - c_1|^2 H_\epsilon(\phi) + |u_0 - c_2|^2 (1 - H_\epsilon(\phi)) dxdy \\ & + \mu \int_\Omega \delta_\epsilon(\phi)|\nabla\phi| dxdy \end{aligned} \tag{3.8}$$

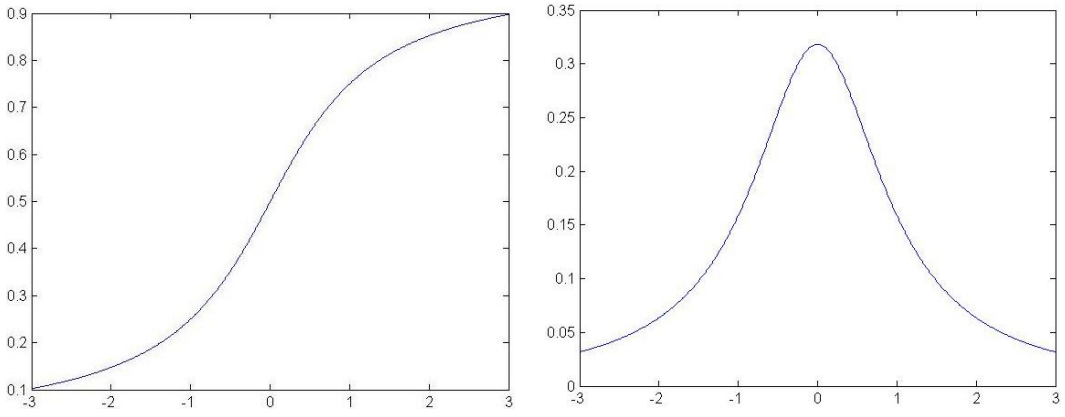

(a) (b)

Figure 3.1: Regularized (a)Heaviside and (b)Dirac functions.

By formal methods of calculus of variations, the associated Euler-Lagrange equations which minimize the two-phase constant CV energy functional can be found. First, ϕ is keep fixed and the functional is minimized with respect to c_1, c_2. Then, c_1, c_2 are kept fixed and the functional is minimized with respect to ϕ. The Gateaux derivative of functional with respect to ϕ can be found and the Euler-Lagrange equations can be deduced. Gateaux derivative of $F\epsilon$ in direction ψ is defined as: $lim_{t\to 0}\frac{F\epsilon(\phi+t\psi,c_1,c_2)-F\epsilon(\phi,c_1,c_2)}{t}$, where ψ is a test function of the same type as ϕ. Details of the derivation are given in Appendix C.

Euler-Lagrange equations of the CV functional are given below with associated Neumann boundary conditions:

$$\delta_\epsilon(\phi)\left(\mu\nabla\bullet\left(\frac{\nabla\phi}{|\nabla\phi|}\right)-\lambda_1\left|u_0-c_1\right|^2+\lambda_2\left|u_0-c_2\right|^2\right)=0 \text{ in } \Omega$$

$$\mu\frac{\delta_\epsilon(\phi)}{|\nabla\phi|}\frac{\partial\phi}{\partial n}=0 \text{ on } \partial\Omega$$

Euler-Lagrange equations are solved by a gradient descent technique, where c_1 and c_2 are given by mean intensities in the two regions. Curve evolution PDE equation for the two-phase constant CV model is given in 3.9.

$$\frac{\partial\phi}{\partial t}=\delta_\epsilon(\phi)\left[\mu div\left(\frac{\nabla\phi}{|\nabla\phi|}\right)-|u_0-c_1|^2+|u_0-c_2|^2\right] \tag{3.9}$$

The initial and boundary conditions are given by:

$$\phi(x,y,0)=\phi_0(x,y) \quad in\ \Omega \tag{3.10}$$

$$\frac{\partial\phi}{\partial n}=0 \quad on\ \partial\Omega \tag{3.11}$$

3.2.1.2 Multi-Phase Piecewise Constant Chan-Vese Model

Two-phase approach is not sufficient for segmentation of images which cannot be reduced to two regions, or images with edges like triple junctions with 120^o angle. A multi-phase level set approach is proposed by Chan-Vese in [10] for segmentation of these type of images. By considering phases as colors and using only four phases, each image region can be represented by one of four different

colors. It is possible to segment the image into an arbitrary number of regions in such a way that no neighbouring regions receive the same color based on the four-color theorem. However, in practice more phases can be needed. In the experiments throughout the thesis, the four-phase model is used for complicated images.

The algorithm needs $log_2 n$ level set functions for n phases. I represents a class, there are totally $n = 2^m$ phases, where m is the number of level set functions. Introducing a characteristic function χ_I, where c_I is the mean of u_0 in each class, the reduced form of MS functional is obtained in equation 3.12, where $\Phi = \phi_1, ..., \phi_m$. Using a regularized Heaviside function as a characteristics function, the CV functional can be constructed with any number of phases.

$$E_{MS}(c, \Phi) = \sum_{1<I<n} \int_\Omega |u_0 - c_I|^2 dxdy + \upsilon \sum_{1<I<n} \int_\Omega |\nabla \chi_I| \tag{3.12}$$

The four-phase CV energy functional is given by equation 3.13, where Heaviside and Dirac functions are to be replaced with regularized versions in implementations. Two level set functions are denoted by $\Phi = \phi_1, \phi_2$ and four phases are denoted by $c = (c_{11}, c_{10}, c_{01}, c_{00})$ in our work. In equations 3.14a-3.16, the associated coupled Euler-Lagrange equations obtained after Gateaux differentiation of the functional in equation 3.13 with respect to $c = (c_{11}, c_{10}, c_{01}, c_{00})$ and $\Phi = \phi_1, \phi_2$ are shown.

$$\begin{aligned} E_{CV_4}(c, \Phi) = \int_\Omega \big\{ & |u_0 - c_{00}|^2 (1 - H(\phi_1))(1 - H(\phi_2)) + |u_0 - c_{11}|^2 H(\phi_1) H(\phi_2) \\ & + |u_0 - c_{10}|^2 H(\phi_1)(1 - H(\phi_2)) dx + |u_0 - c_{01}|^2 (1 - H(\phi_1)) H(\phi_2) \\ & + \upsilon \left[|\nabla H(\phi_1)| + |\nabla H(\phi_2)| \right] \big\} dxdy \end{aligned} \tag{3.13}$$

$$c_{11} = mean(u_0) \text{ in } \{\phi_1 > 0, \phi_2 > 0\} \tag{3.14a}$$

$$c_{10} = mean(u_0) \text{ in } \{\phi_1 > 0, \phi_2 < 0\} \tag{3.14b}$$

$$c_{01} = mean(u_0) \text{ in } \{\phi_1 < 0, \phi_2 > 0\} \tag{3.14c}$$

$$c_{00} = mean(u_0) \text{ in } \{\phi_1 < 0, \phi_2 < 0\} \tag{3.14d}$$

$$\begin{aligned}\frac{\partial \phi_1}{\partial t} = \delta\epsilon(\phi_1) \Bigg\{ v div \left(\frac{\nabla \phi_1}{|\nabla \phi_1|} \right) - \big[\left((u_0 - c_{11})^2 - (u_0 - c_{01})^2 \right) H(\phi_2) \\ - \left((u_0 - c_{10})^2 - (u_0 - c_{00})^2 \right) (1 - H(\phi_2)) \big] \Bigg\}\end{aligned} \tag{3.15}$$

$$\begin{aligned}\frac{\partial \phi_2}{\partial t} = \delta\epsilon(\phi_2) \Bigg\{ v div \left(\frac{\nabla \phi_2}{|\nabla \phi_2|} \right) - \big[\left((u_0 - c_{11})^2 - (u_0 - c_{01})^2 \right) H(\phi_1) \\ - \left((u_0 - c_{10})^2 - (u_0 - c_{00})^2 \right) (1 - H(\phi_1)) \big] \Bigg\}\end{aligned} \tag{3.16}$$

3.2.2 Piecewise Smooth Chan-Vese Model

3.2.2.1 Two-Phase Piecewise Smooth Chan-Vese Model

In the two-phase piecewise smooth CV model, a piecewise smooth approximation u of u_0 and an edge set Γ is computed by minimizing the CV functional given in equation 3.17. Image is segmented into two regions and u is equal to u^+ inside the curve and u^- outside the curve . Unknown edge set is represented by $\Gamma = \{(x, y) | \phi(x, y) = 0\}$ in level set framework.

$$\begin{aligned}\inf_{u^+, u^-, \Gamma} \Big\{ E_{CV2s}\left(u^+, u^-, \Gamma\right) = & \int_\Omega |u^- - u_0|^2 (1 - H(\phi)) dxdy \\ & + \int_\Omega |u^+ - u_0|^2 H(\phi) dxdy + \beta \int_\Omega |\nabla u^+|^2 H(\phi) dxdy \\ & + \beta \int_\Omega |\nabla u^-|^2 (1 - H(\phi)) dxdy + \nu \int |\nabla H(\phi)| \Big\}\end{aligned} \tag{3.17}$$

By minimizing 3.17, using the formal methods of calculus of variations, the Euler-Lagrange equations are obtained as given in 3.18, 3.19, 3.20. The differential equations for u^+, u^- are called damped Poisson equations, or optimal

estimation PDE's and they have a denoising effect on the image u_0 inside each region, but not across the edges. But, solving these equations are computationally not efficient, its denoising capability is not perfect.

$$\begin{aligned} u^+ - u_0 &= \beta \triangle u^+ \text{ in } \{(x,y) : \phi(t,x,y) < 0\} \\ \frac{\partial u^+}{\partial \vec{n}} &= 0 \text{ in } \{(x,y) : \phi(t,x,y) = 0\} \cup \partial\Omega \end{aligned} \tag{3.18}$$

$$\begin{aligned} u^- - u_0 &= \beta \triangle u^- \text{ in } \{(x,y) : \phi(t,x,y) > 0\} \\ \frac{\partial u^-}{\partial \vec{n}} &= 0 \text{ in } \{(x,y) : \phi(t,x,y) = 0\} \cup \partial\Omega \end{aligned} \tag{3.19}$$

$$\frac{\partial \phi}{\partial t} = \delta_\epsilon(\phi) \left[\nu \nabla \left(\frac{\nabla \phi}{|\nabla \phi|} \right) - |u^+ - u_0|^2 - \beta |\nabla u^+|^2 + |u^- - u_0|^2 + \beta |\nabla u^-|^2 \right] \tag{3.20}$$

3.2.2.2 Multi-Phase Piecewise Smooth Chan-Vese Model

The multi-phase piecewise smooth CV Model is also obtained in [10]. Like the multi-phase piecewise constant CV Model, an image is divided into 2^n regions, with n level set functions. The only difference between the two models is that mean intensities are calculated in each region in the piecewise smooth case and optimal estimation PDEs are solved in each region in the piecewise smooth case.

3.3 TSAI ET. AL.'S METHOD

In [9], Tsai et. al. independently proposed a very similar approach to the piecewise-smooth CV model for the implementation of the MS image segmentation method by level set methods. In the simplified functional proposed by Tsai et. al. shown in equation 3.21, the smoothing term is kept and the general term representing length of edge set $|\Gamma|$ is replaced by $\oint_\Gamma ds$ since a curve embedded in level set is automatically smooth.

$$\inf_{u^+,u^-,\Gamma}\Big\{E\left(u^+,u^-,\Gamma\right)=\int_{\phi<0}|u^- - u_0|^2dxdy + \int_{\phi>0}|u^+ - u_0|^2dxdy+\beta\int_{\phi>0}|\nabla u^+|^2dxdy + \beta\int_{\phi<0}|\nabla u^-|^2dxdy+\nu\oint_\Gamma ds\Big\} \tag{3.21}$$

Minimizing the functional with respect to smooth functions u^- and u^+, the optimal estimation PDEs are obtained as given in 3.18 and 3.19.

The curve evolution equation is obtained by minimizing the functional with respect to boundary set. Let H be of same type as u_0 and n denote the outer normal of the curve. There are five different terms in the functional. The first four terms in 3.21 are of type $\int_D H dxdy$ and the gradient flow that minimizes these functionals found as $\Gamma_t = -Hn$. Details of derivations are given in Appendix D. This derivation is originally provided in [25]. The fifth term is the arc length of the curve and the gradient flow that minimizes it is found as $\Gamma_t = -\kappa n$. As examined in Appendix B, κ denotes the curvature of the curve. This gradient flow is derived in Appendix E. This derivation follows the derivation of the gradient flow of functionals of type $\int_D H dxdy$. Curve evolution equation $\Gamma_t = F \bullet n$, can be implemented by level set methods as:

$$\phi\left(\Gamma\left(t\right),t\right)=0 \tag{3.22}$$

$$\frac{\partial\Gamma}{\partial t}=F\bullet n \tag{3.23}$$

$$\frac{d}{dt}\phi\left(\Gamma\left(t\right),t\right)=\nabla\phi\frac{\partial\Gamma}{\partial t}+\frac{\partial\phi}{\partial t}=\nabla\phi F\bullet n+\frac{\partial\phi}{\partial t}=0 \tag{3.24}$$

$$n=\frac{\nabla\phi}{|\nabla\phi|}$$

$$\frac{\partial\phi}{\partial t}=-\left|\nabla\phi\right|F \tag{3.25}$$

Obtained PDE equation in Tsai et. al's method and in the piecewise-smooth CV model are the same, except in the Euler- Lagrange equations (equation 3.20) of Tsai's method, $\delta_\epsilon(\phi)$ is replaced with $|\nabla\phi|$. If $\delta_\epsilon(\phi)$ in equation 3.20 is replaced with $|\nabla\phi|$, then obtained PDE equation is called the MS gradient flow.

It is noted that using smooth regions, it is easier to find objects with different intensity sub regions. It is also noted that solving optimal estimation PDE's at every iteration is not efficient and some approximations are proposed. Taking several iterations of optimal estimation PDE equation and few iterations of curve evolution PDE equation is enough to get an estimate without convergence at each step. At the final step, optimal estimation PDE equation are solved until convergence to find the piecewise smooth image.

For images with more complex edges and multiple regions, a hierarchical approach to implement the MS model by active contours is used in [9] instead of resorting to the coupled multiphase level set functions as proposed by Chan-Vese. In the hierarchical approach, an image is segmented into two regions by the MS active contour method. This segmentation is followed by user's selection of the regions in which further segmentation is needed. Then, the selected regions are segmented by the MS active contour method again. Hierarchical implementations are further developed by Gao and Bui in [11].

The PDE equations for two-phase image segmentation by Tsai et.al.'s method's are given below:

$$\begin{aligned} u^+ - u_0 &= \beta\triangle u^+ \text{ in } \{(x,y) : \phi(t,x,y) < 0\} \\ \frac{\partial u^+}{\partial \vec{n}} &= 0 \text{ in } \{(x,y) : \phi(t,x,y) = 0\} \cup \partial\Omega \end{aligned} \tag{3.26}$$

$$\begin{aligned} u^- - u_0 &= \beta\triangle u^- \text{ in } \{(x,y) : \phi(t,x,y) > 0\} \\ \frac{\partial u^-}{\partial \vec{n}} &= 0 \text{ in } \{(x,y) : \phi(t,x,y) = 0\} \cup \partial\Omega \end{aligned} \tag{3.27}$$

$$\frac{\partial\phi}{\partial t} = |\nabla\phi| \left[\nu\nabla\left(\frac{\nabla\phi}{|\nabla\phi|}\right) - |u^+ - u_0|^2 - \beta|\nabla u^+|^2 + |u^- - u_0|^2 + \beta|\nabla u^-|^2\right] \tag{3.28}$$

These PDE equations can be transformed into piecewise constant case if u is restricted to take constant values in each region similar to the approach in the piecewise constant CV model.

3.4 NUMERICAL SCHEMES

The PDE equation in 3.9 is solved by a semi-implicit numerical scheme. The scheme in the ROF model [14] is used for the discretization of the divergence term.

Let $h = \triangle x = \triangle y$ be the space steps, let $\triangle t$ be the time step, $\epsilon = h$. In our experiments, we choose $h = 1$ and $\triangle t = 0.1$. We recall the following notations:

$$(x_i, y_j) = (ih,\ jh) \quad for\ 1 \leq i \leq M,\ 1 \leq j \leq N \tag{3.29}$$

$$u_{0i,j} = u_0\left(x_i, y_j\right) \tag{3.30}$$

$$\phi^n_{i,j} = \phi(n\triangle t, x_i, y_j) \tag{3.31}$$

$$\triangle^x_{\pm}\phi_{i,j} = \pm\left(\phi_{i\pm1,j} - \phi_{i,j}\right) \tag{3.32}$$

$$\triangle^y_{\pm}\phi_{i,j} = \pm\left(\phi_{i,j\pm1} - \phi_{i,j}\right) \tag{3.33}$$

$$\triangle^x_0\phi_{i,j} = \pm\left(\phi_{i+1,j} - \phi_{i-1,j}\right)/2 \tag{3.34}$$

$$\triangle^y_0\phi_{i,j} = \pm\left(\phi_{i,j+1} - \phi_{i,j-1}\right)/2 \tag{3.35}$$

Constant values c_1 and c_2 corresponding to the regions inside the curve and outside the curve respectively are estimated by the mean intensities of that regions:

$$c_1(\phi) = \frac{\int u_0 H_\epsilon(\phi)dx}{\int H_\epsilon(\phi)dx} = average(u_0) \quad \text{in} \quad \phi > 0 \tag{3.36}$$

$$c_2(\phi) = \frac{\int u_0(1 - H_\epsilon(\phi))dx}{\int(1 - H_\epsilon(\phi))dx} = average(u_0) \quad \text{in} \quad \phi < 0 \tag{3.37}$$

Using the numerical scheme in the ROF model[14], the discrete form of the Euler-Lagrange equation of the CV functional can be obtained as:

$$\begin{aligned}\frac{\phi_{i,j}^{n+1}-\phi_{i,j}^{n}}{\triangle t} = \delta_\epsilon\left(\phi_{i,j}^{n}\right)\Bigg[&\frac{\mu}{h^2}\triangle_-^x\cdot\left(\frac{\triangle_+^x\phi_{i,j}^{n+1}}{\left(\triangle_+^x\phi_{i,j}^{n}\right)^2/h^2+\left(\triangle_0^y\phi_{i,j}^{n}\right)^2/(2h)^2}\right)\\&+\frac{\mu}{h^2}\triangle_-^y\cdot\left(\frac{\triangle_+^y\phi_{i,j}^{n+1}}{\left(\triangle_0^x\phi_{i,j}^{n}\right)^2/(2h)^2+\left(\triangle_+^y\phi_{i,j}^{n}\right)^2/h^2}\right)\\&-\lambda_1\left(u_{0i,j}-c_1\right)^2+\lambda_2\left(u_{0i,j}-c_2\right)^2\Bigg]\end{aligned} \tag{3.38}$$

In the piecewise constant case of the MS Gradient Flow, $\delta_\epsilon(\phi)$ in equation 3.38 is replaced with $|\nabla\phi|$ and there is no other difference between them.

After evolving for many iterations, level set function becomes flat, therefore gradient may blow up or vanish. In order to prevent instabilities caused by the blowing up or vanishing of gradient, reinitialization of the level set function to a signed distance distance function after some iterations is necessary in numerical implementations. Level set is re-initialized by solving equation 3.39. After solving this equation for 10-20 iterations, ϕ is replaced by a signed distance level set function ψ. However, reinitialization step is not necessary in some images for which only a few iterations of level set evolutions are performed.

$$\psi_t = sign(\phi(t))(1-|\nabla\psi|) \tag{3.39}$$

$$\psi(0,.) = \phi(t,:)$$

3.5 RESULTS

The two-phase constant CV model can be implemented by using Algorithm 1. In general, after solving the CV PDE equations for 10 iterations, the re-initialization PDE equation is solved for 10 iterations. For gradient flows method, the same algorithm is used, but in the PDE equations, $\delta_\epsilon(\phi)$ is replaced with $|\nabla\phi|$. The MS image segmentation methods are implemented in a MATLAB environment.

Algorithm 1 Chan-Vese Algorithm (Two-phase piecewise constant case)

1. First construct level set function as Euclidean distance to a given initial curve.
2. Compute c_1, c_2 by equations 3.36 and 3.37.
3. Solve PDE equation 3.38.
4. If, a suitable segmentation is found, stop iterations and draw the final curve using final level set function.

Else, return to step 2. (At every 10 or 20 iterations, reinitialize the level set function before returning to step 2.)

Although, the CV model is less dependent on initialization than the boundary based active contour methods, it is still dependent on initialization. In the CV model based image segmentation, there are two different ways of initialization. In one way, user draws the initial curve user near to the object to be segmented. In our implementation, initially user places a rectangle near the objects in the image. But, if the initial curve is not suitable, then algorithm converges to an undesirable local minima. There are ways to reduce the dependency on initial contour placement, like the seed initialization technique proposed by Chan-Vese in [10]. In this technique, algorithm starts with small circles equally distributed around the image. An example of a level set function which is created by calculating the distance of each point in the image to curve is given in Figure 3.2, in which the initial curve is created by small circles distributed equally on the image plane.

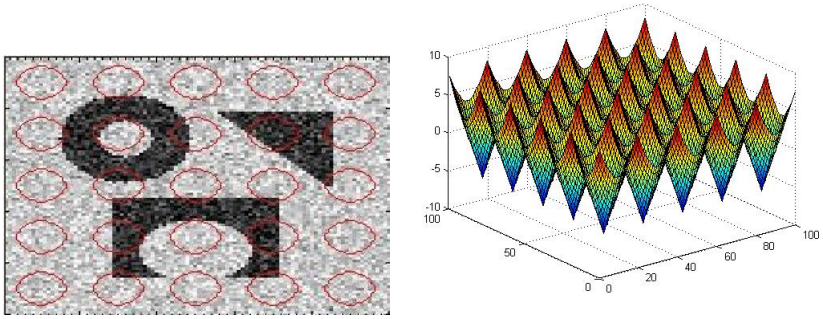

(a) (b)

Figure 3.2: (a) Seed initialization of the curve. (b)Starting level set function.

Some experiments are done on some geometric test images with the CV active contour method. Experiments are done on a Pentium 4, 3 Ghz, 512 MB RAM desktop computer. Reinitialization is not used in many of these experiments, and algorithm still works.

3.5.1 Experiments on Simple Geometric Piecewise Constant Images

Some experiments are done with geometric piecewise smooth images. This section starts with experiments done for testing the CV method's dependency on initial curve placement. In Figure 3.3, a rectangle outside all 3 objects is used, in Figure 3.4, a rectangle inside one of the objects is used, and in Figure 3.5, a rectangle around 2 objects is used. Result in the first one is satisfactory, but in the second one, algorithm is stuck into an undesired local minima, and it cannot find 3 objects even at 1000 iterations. Best performance is observed in Figure 3.5, in which active contour does not find any noisy image spikes in the final contour.

The result of the one-phase CV active contour method is given in Figure 3.7 for a simple geometric image with 50 iterations. Notice that in this case, seed initialization technique is used for initial curve placement. As seen in Figure 3.7, results are satisfactory, and algorithm does not find any noisy spikes as objects. In order to find big objects, but not to find small noisy image spikes, μ should be kept large (for example, $\mu = 3000$ in this experiment).

Next, the effect of reinitialization on the CV Method is tested. Reinitialization at every 10 iterations, is used in this experiment. Algorithm run time increased from 0.9 s in implementation without reinitialization shown in Figure 3.6 (60 iterations were performed), to 4.4 s in implementation with reinitialization (60 iterations were performed). Result of the case with reinitialization is shown in Figure 3.7. In this test image, algorithm is successful even without reinitialization procedure.

Piecewise constant case of Tsai et. al.'s method is implemented and some experiments are done. In our implementation, we do not solve optimal estimation PDEs but the values of u in each region are calculated by the mean intensity of that region assuming that image is composed of piecewise constant regions. In Figure 3.8, we show the satisfactory result after 50 iterations for the same image. More iterations do not make the result better, and a noisy image spike is still found by active contour for example, at 300 iterations as seen in Figure 3.8. If iterations exceeds a certain number, level set function is bigger than zero in all image, and the contour is not drawn on the image as also noted by Duramaz in [26]. Thus, if 550 iterations are done, the level set function becomes greater than zero on the whole image domain, the curve is outside of the image. Therefore, the curve is not plotted by MATLAB. Since the level set function evolves faster with the MS gradient flow, iteration number should not be kept as high as the iteration number of the CV model. Otherwise, the curve disappears.

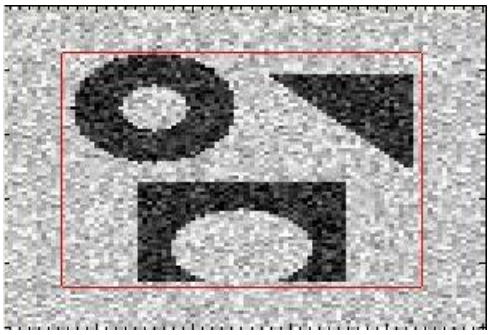

(a)

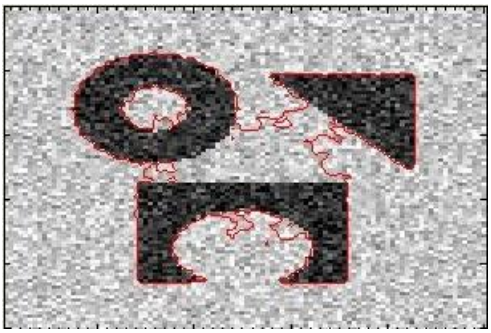

(b)

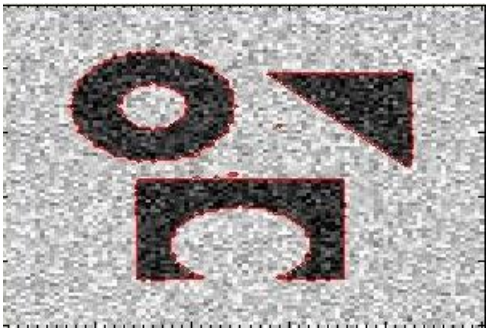

(c)

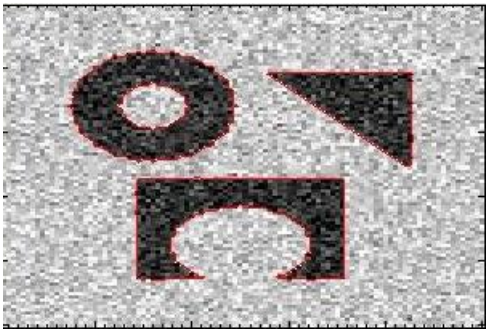

(d)

Figure 3.3: One-phase CV result ($\alpha = 1$, $\mu = 3000$, no re-initialization). (a) Initial contour. (b)- (c)- (d) 47, 94, 140 iterations (4.36 s).

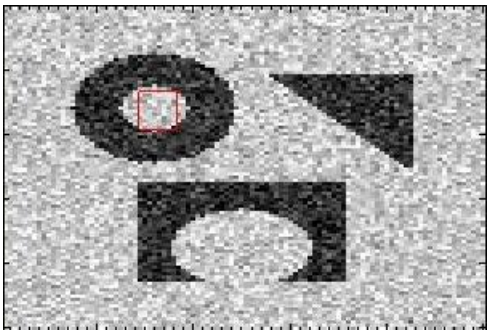

(a)

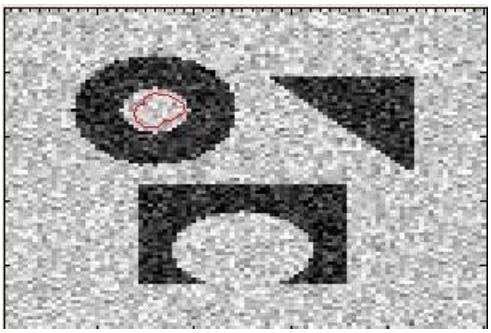

(b)

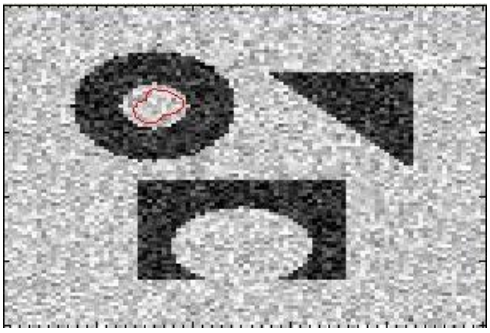

(c)

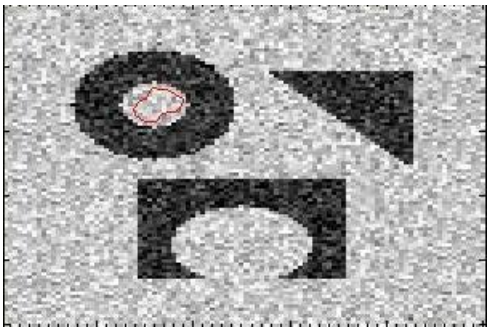

(d)

Figure 3.4: One-phase CV result ($\alpha = 1$, $\mu = 3000$, 1000 iterations, no re-initialization). (a) Initial contour (b)- (c)- (d) 333, 666, 1000 iterations (18.9 s).

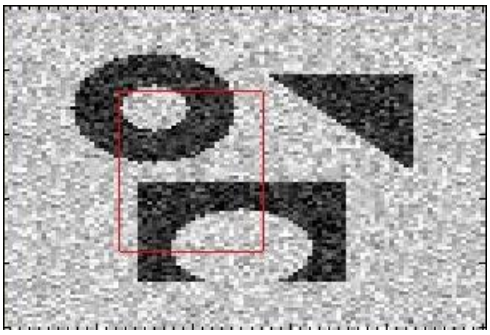

(a)

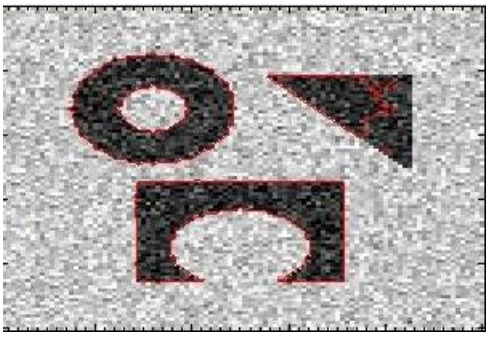

(b)

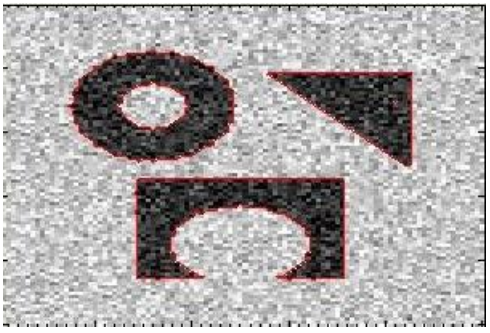

(c)

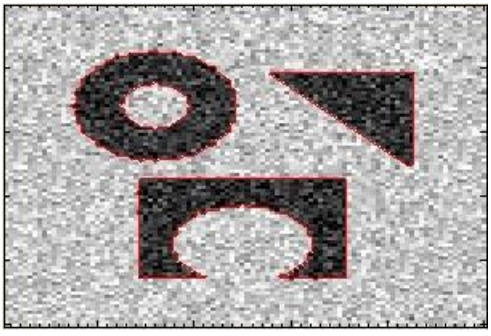

(d)

Figure 3.5: One-phase CV result ($\alpha = 1$, $\mu = 3000$, 60 iterations, no re-initialization). (a) Initial contour (b)- (c)- (d) 20, 40, 60 iterations (1.15 s).

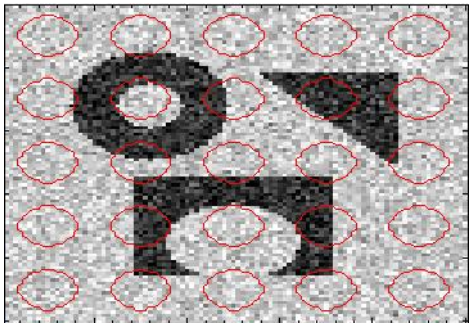

(a)

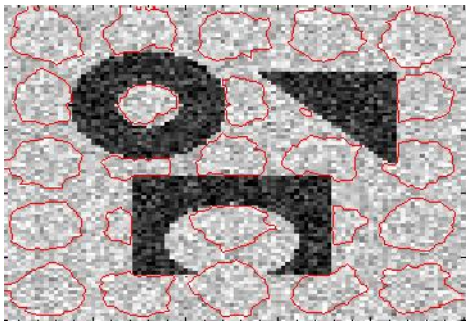

(b)

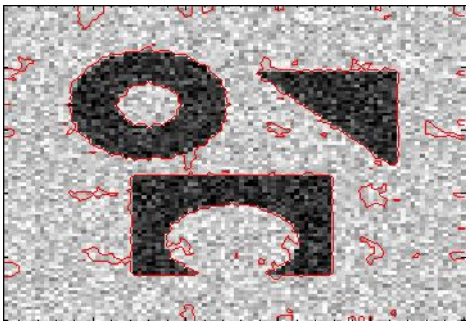

(c)

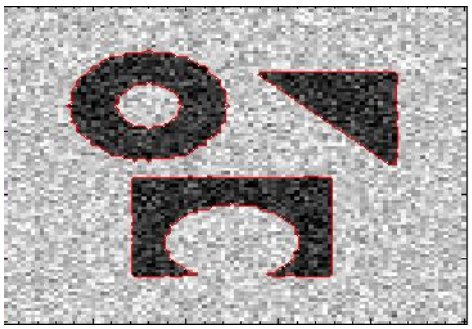

(d)

Figure 3.6: One-phase CV result ($\alpha = 1$, $\mu = 3000$, no re-initialization). (a) Initial contour (b)- (c)- (d) 20, 40, 60 iterations (0.88 s).

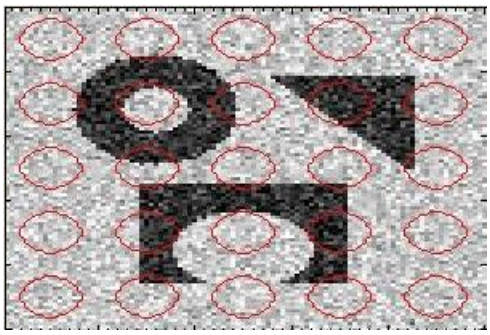

(a)

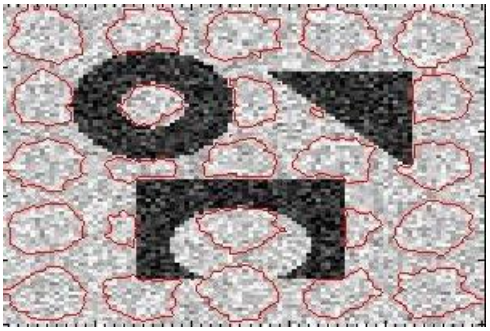

(b)

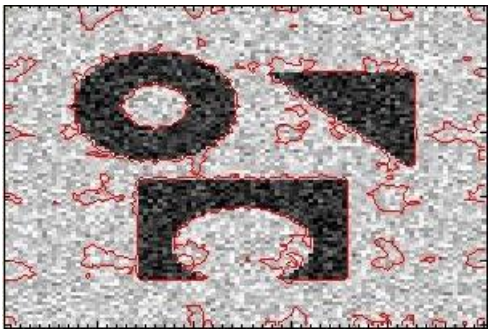

(c)

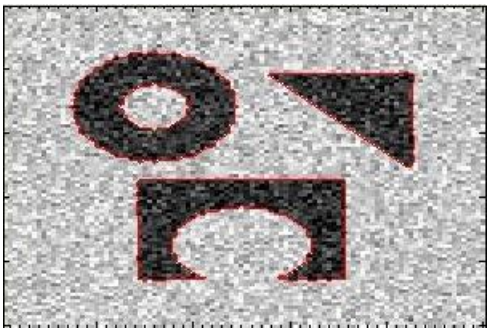

(d)

Figure 3.7: One-phase CV result ($\alpha = 1$, $\mu = 3000$, re-initialization at every 10 iterations). (a) Initial contour. (b)- (c)- (d) 17, 33, 50 iterations (4.36 s).

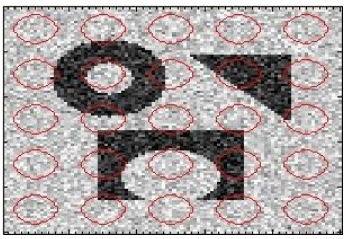

(a)

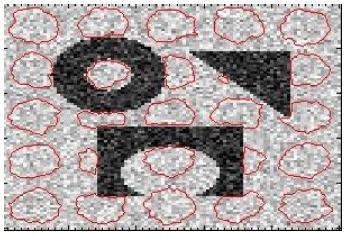

(b)

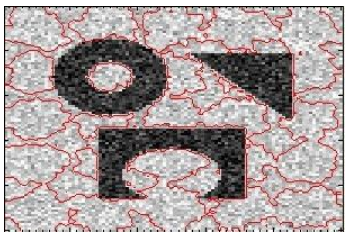

(c)

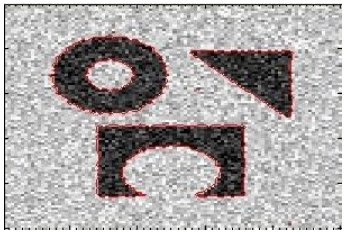

(d)

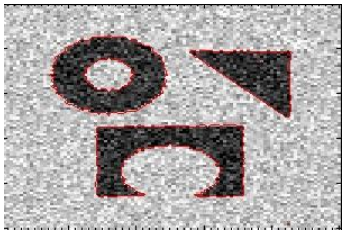

(e)

Figure 3.8: One-phase GF result ($\alpha = 1$, $\mu = 3000$, 40 iterations, no re-initialization). (a) Initial contour (b)- (c)- (d) 13, 27, 40 iterations (3.672 s). (e) 300 iterations (7.922 s).

3.5.2 Experiments on Complicated Geometric Piecewise Constant Images

A four-phase CV active contour method is used for a more complicated 354*287 image which does not consist of only 2 regions with distinct mean intensities. Results are given in Figure 3.9 and Figure 3.10 after different initializations for 500 and 600 iterations, respectively. In the first case, segmentation is perfect; but in the second case, algorithm does not find the white object properly.

Seed initialization is also used, but with given initial conditions, objects are not found as shown in Figure 3.11. When seed initialization is used with a different initial condition, objects are properly found as shown in Figure 3.12. It can be concluded that even in automatic initialization, objects are not always found depending on the initial contour placement.

Finally, in Figure 3.13, a satisfactory result with piecewise constant gradient flows method is shown.

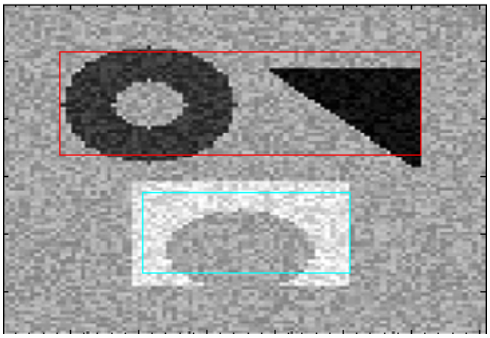

(a)

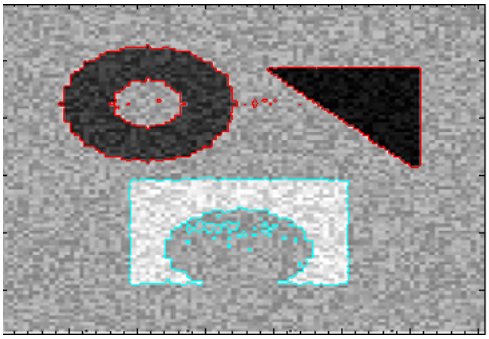

(b)

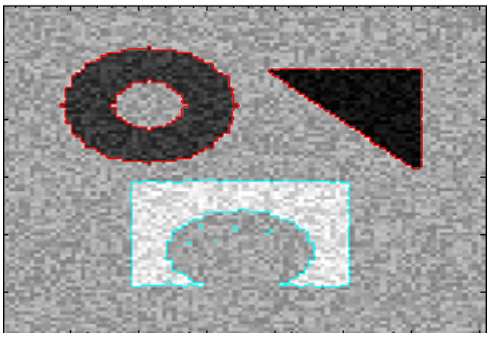

(c)

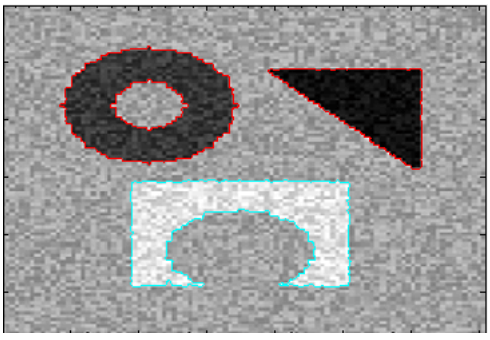

(d)

Figure 3.9: Two-phase CV result ($\alpha = 1$, $\upsilon = 0.0165 * 357 * 265$), 500 iterations. (a) Initial contour. (b)- (c)- (d) 167, 334, 500 iterations (161.50 s).

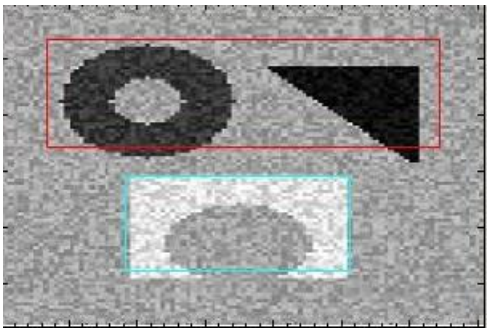

(a)

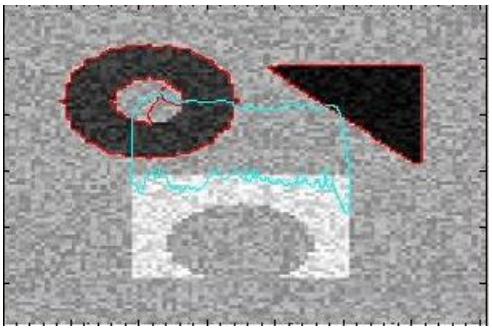

(b)

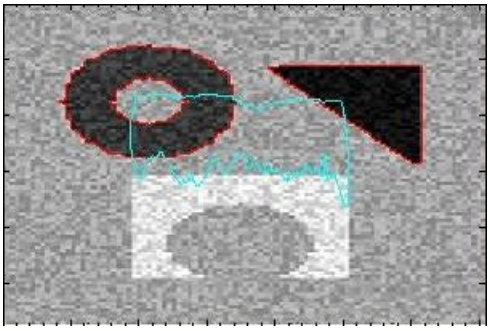

(c)

Figure 3.10: Two-phase CV result ($\alpha = 1$ $\upsilon = 0.0165 * 357 * 265$). (a) Initial contour. (b)- (c) 500 and 600 iterations (407.6 s).

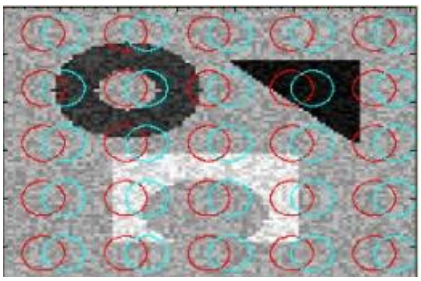

(a)

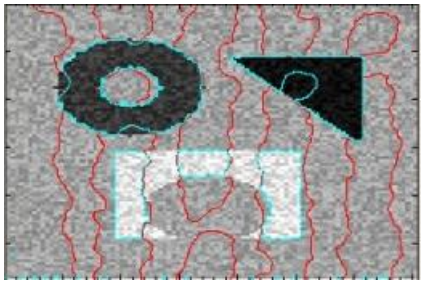

(b)

Figure 3.11: Two-phase CV result ($\alpha = 1$, $v = 0.0165 * 357 * 265$). (a) Initial contour. (b) 1533 iterations.

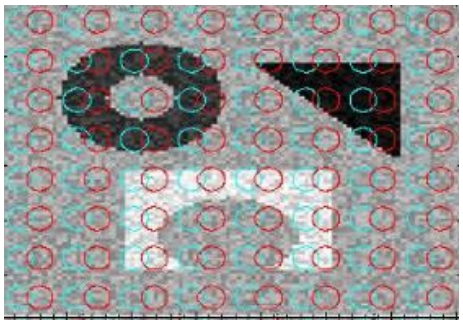

(a)

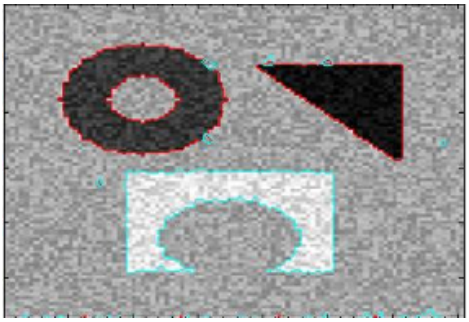

(b)

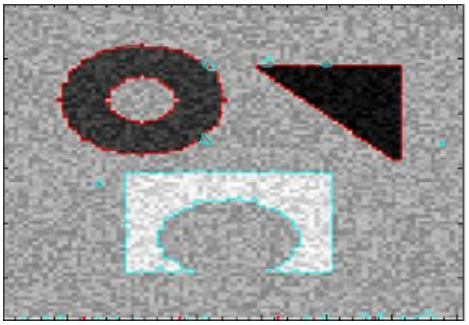

(c)

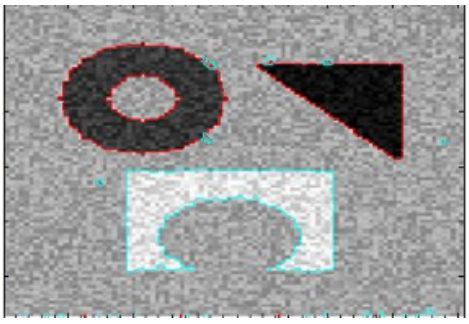

(d)

Figure 3.12: Two-phase CV result ($\alpha = 1$, $\upsilon = 0.033 * 357 * 265$, 329 s). (a) Initial contour. (b)- (c)- (d) 333, 666, 1000 iterations.

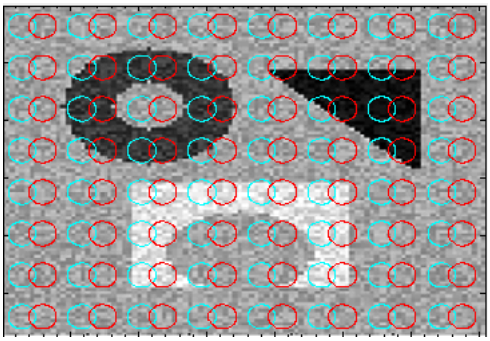

(a)

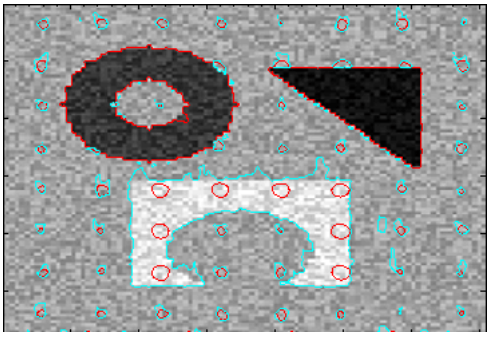

(b)

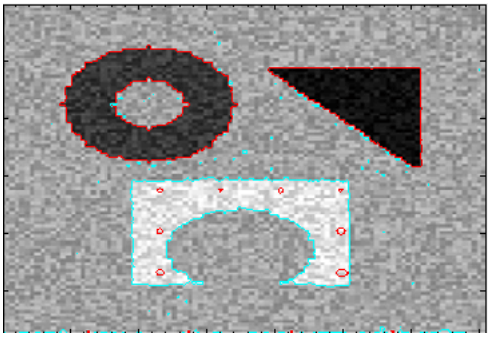

(c)

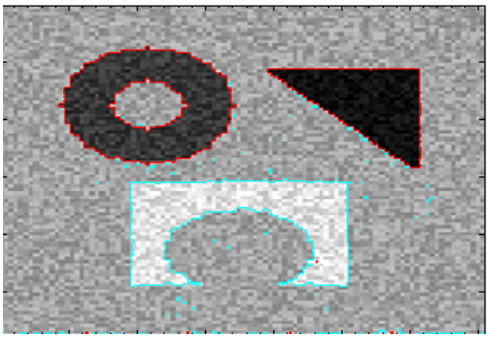

(d)

Figure 3.13: Two-phase GF result ($\alpha = 1$, $\upsilon = 0.033 * 357 * 265$). (a) Initial contour. (b)- (c)- (d) 67, 134, 200 iterations (87.4 s).

3.5.3 Experiments on Natural Images

A natural image which consists of uniform intensity regions is input to the CV active contour method. Segmentation result shown in Figure 3.14 is satisfactory except some small mistakes of the final contour. Parameters are $\mu = 3000$ and $\alpha = 1$ and 1800 iterations are done.

(a) (b)

(c) (d)

Figure 3.14: Segmentation by the CV method, plane image. (a) Initial contour. (b)- (c)- (d) 800, 1400, 1800 iterations (1211 s).

A natural bird image is input to the CV method. The segmentation result shown in Figure 3.15 is satisfactory. Parameters are $\mu = 3000$ and $\alpha = 1$ and 1500 iterations are performed.

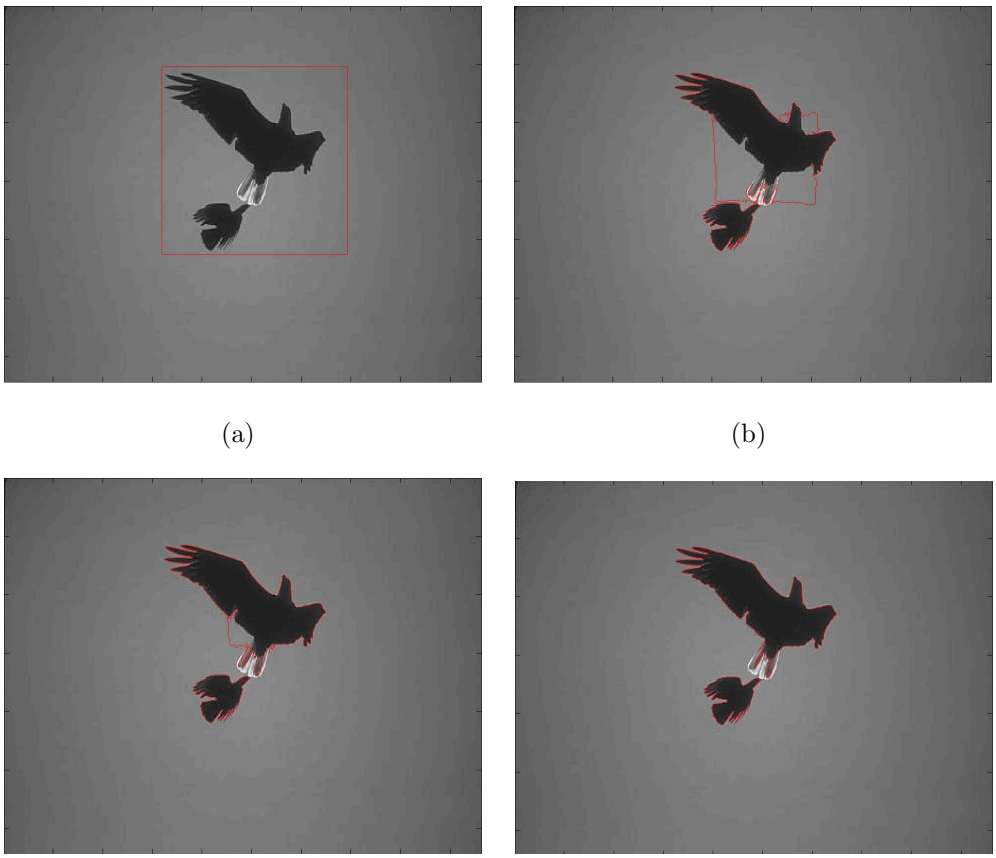

(a) (b)

(c) (d)

Figure 3.15: Segmentation by the CV method, bird image. (a) Initial contour. (b) 666, 1167, 1500 iterations (424 s).

CHAPTER 4

DIFFUSION FILTERS

4.1 HEAT EQUATION

Diffusion filters are PDE based techniques for image smoothing. The most basic type of diffusion filters is based on the heat equation. Images are smoothed homogeneously by solving the heat equation. This approach is also called the linear diffusion filtering. Linear diffusion equation is shown in equation 4.1, with initial and boundary conditions. Input image is denoted by u_0, filtered image is denoted by $u\,(x,t)$ and image domain is denoted by $\Omega \subseteq \mathbb{R}^2$, spatial coordinate is denoted by $x \in \Omega$ and the boundary of image is denoted by $\Gamma = \partial\Omega$. Outer normal to boundaries of image domain is denoted by n. Time, t can be seen as scale parameter and linear diffusion filtering can be seen as a scale-space representation of the denoised image. The solution of heat equation is equivalent to convolving the image with two dimensional Gaussian kernel of blurring radius $\sigma = \sqrt{2t}$ [12]. Since solving the heat equation denoises the image in the same way as Gaussian smoothing, the edges are blurred.

$$\frac{\partial u}{\partial t} = div(\nabla u) \quad on\ \Omega \times (0,\infty) \tag{4.1}$$

$$u\,(x,0) = u_0\,(x)$$

$$\frac{\partial u}{\partial n} = 0 \quad on\ \Gamma \times (0,\infty)$$

4.2 ISOTROPIC NONLINEAR DIFFUSION FILTERS

The smoothing is done homogeneously on the entire image domain in heat equation approach. In order to make smoothing spatially adaptive, PDEs are controlled by an edge detector function such that the image is smoothed only inside of each region. Therefore, an edge detector function which is small at the boundaries but large inside of the regions enclosed by the boundaries is used. Ideally, at edges (where $|\nabla u|^2 \to \infty$) $g = 0$ and at pixels which are not on boundary (where$|\nabla u|^2 = 0$) $g = 1$. The edge detector function used in our experiments is $g(s) = 1/\left(1 + \frac{s}{\lambda}\right)$. Nonlinear diffusion as proposed by Perona and Malik in [18] is given in equation 4.2 with initial and boundary conditions.

$$\frac{\partial u}{\partial t} = div(g\left(|\nabla u|^2\right)\nabla u) \quad on\ \Omega \times (0,\infty) \tag{4.2}$$

$$u(x,0) = u_0(x)$$

$$\frac{\partial u}{\partial n} = 0 \quad on\ \Gamma \times (0,\infty)$$

Contrary to the claim of the authors [18], this approach is not anisotropic since it does take the orientation of the edge into account. Nonlinear diffusion filtering approach of Perona and Malik removes noise inside regions, however it does not remove noise along the edges since diffusion is inhibited at edges regardless of the orientation of the edge. [1]

One disadvantage of Perona-Malik equation is that it is ill-posed. In [19], a regularization of Perona-Malik model is proposed by using Gaussian smoothed image u_σ in the edge detector function. This model has a unique solution due to the fact that ∇u_σ remains bounded. This regularization brings well-posedness and robustness against noise. Regularized Perona-Malik equations are shown in equation 4.3.

[1] The anisotropic nonlinear diffusion [20, 21] is invented by Weickert. Anisotropic nonlinear diffusion equation inhibits diffusion across edges while allowing diffusion along the edges by using the edge direction information.

$$\frac{\partial u}{\partial t} = div(g\left(|\nabla u_\sigma|^2\right)\nabla u) \quad on\ \Omega \times (0,\infty) \tag{4.3}$$

$$u\left(x,0\right) = u_0\left(x\right)$$

$$\frac{\partial u}{\partial n} = 0 \quad on\ \Gamma \times (0,\infty)$$

Indeed, idea and performance of nonlinear diffusion filters are similar to optimal estimation PDE's in the level set implementations of the MS functional based image segmentation. The scheme which solves the Perona-Malik equation is the same as the scheme used in the discretization of the divergence term in the AT PDE equation of u.

4.3 RESULTS

Original Lena image and its noisy version are shown in Figure 4.1.

(a) (b)

Figure 4.1: (a) Original Lena image. (b) Noisy Lena image.

The results of diffusion filters are shown in Figure 4.2. It is clear that noise is filtered out but edges are blurred by linear diffusion filtering. Result of nonlinear diffusion is better than linear diffusion filtering since it smoothes the image with edge preservation as it can be shown form Figure 4.2. λ is the contrast parameter, at pixels $\nabla u > \lambda$ edges are enhanced and $\nabla u < \lambda$ small scale details are eliminated. Increasing λ, lesser pixels are regarded as edges and blurring problem starts to occur. The results of regularized nonlinear diffusion are similar to nonlinear diffusion.

(a)

(b)

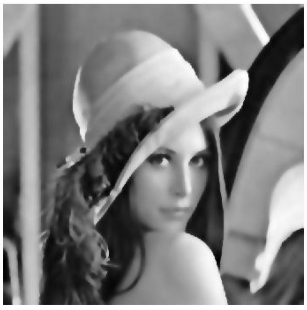

(c)

(d)

(e)

Figure 4.2: Diffusion filtering on noisy Lena image. (a) Linear diffusion filtered version (42 s). (b) Nonlinear diffusion filtered version ($\lambda = 2$). (c) Nonlinear diffusion filtered version ($\lambda = 3$) (45s). (d) Regularized nonlinear diffusion filtered version ($\lambda = 2$). (e)Regularized nonlinear diffusion filtered version ($\lambda = 3$) (45s).

CHAPTER 5

TEXTURE IMAGE SEGMENTATION BY ACTIVE CONTOURS

Textured image segmentation is a challenging problem. Object boundaries at textured images cannot be detected by gradient modulus since gradient value is high even inside of the objects. Objects in highly textured images does not consist of one region with distinct mean but it consists of many small regions with different mean intensities. Hence, neither boundary-based active contour models (for example, the geodesic active contours method) nor region-based active contour models (for example, the CV method) are directly applicable to textured image segmentation. However, there are some extensions of the CV method and the geodesic active contours method for texture segmentation by creating a Gabor-based image feature space in the literature. In this chapter of the thesis, these techniques are analyzed. Experimentally, it is observed that the extension of the CV method for textured image segmentation provides quite satisfactory results. However, the extension of geodesic active contours method for textured image segmentation does not provide satisfactory results.

5.1 CHAN-VESE ACTIVE CONTOUR METHOD

As being a model based on the MS model, the CV method draws a cartoon approximation of the original images with objects drawn without textures. Quality of segmentation of non-textured images or lowly textured images by this method is satisfactory. However, the CV method is not applicable to segmentation of textured images if a textured region consists of different homogeneous regions in

terms of intensity. The CV functional is given in equation 3.3. The results of the model for some textured images given in this section show that the CV method fails for texture segmentation.

5.1.1 Experiment I

The performance of the model is not perfect for segmentation of the textured zebra image in Figure 5.1. Not the zebra but the black stripes inside of the zebra is found as the object by the CV method. Parameters are $\mu = 8000$ and $\alpha = 1$.

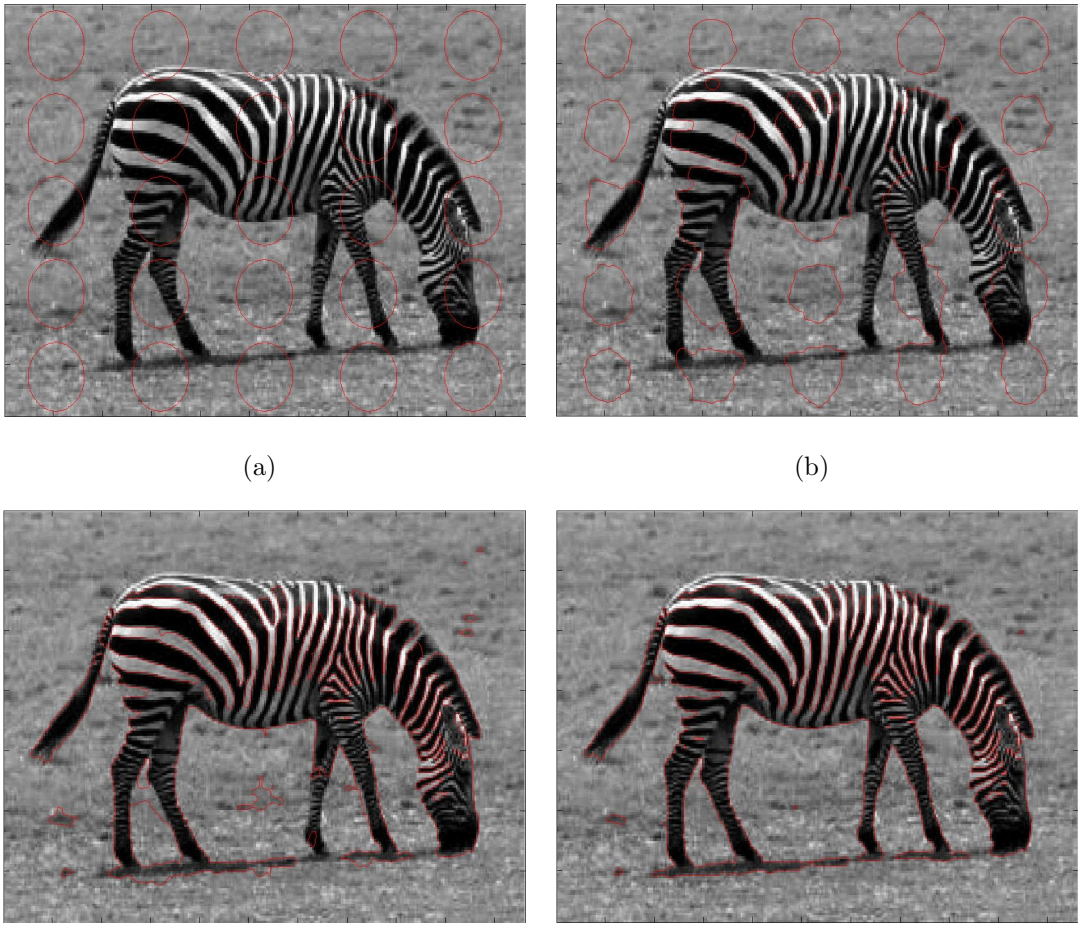

(a) (b)

(c) (d)

Figure 5.1: Zebra-1 image, CV method. (a) Initial contour. (b)- (c)- (d) 83, 167, 250 iterations (190 s).

5.1.2 Experiment II

In Figure 5.2, another textured zebra image is segmented. The CV method finds the zebra as the object in the scene but it also finds some of the white stripes inside of zebra as background. Parameters are $\mu = 12000$ and $\alpha = 1$.

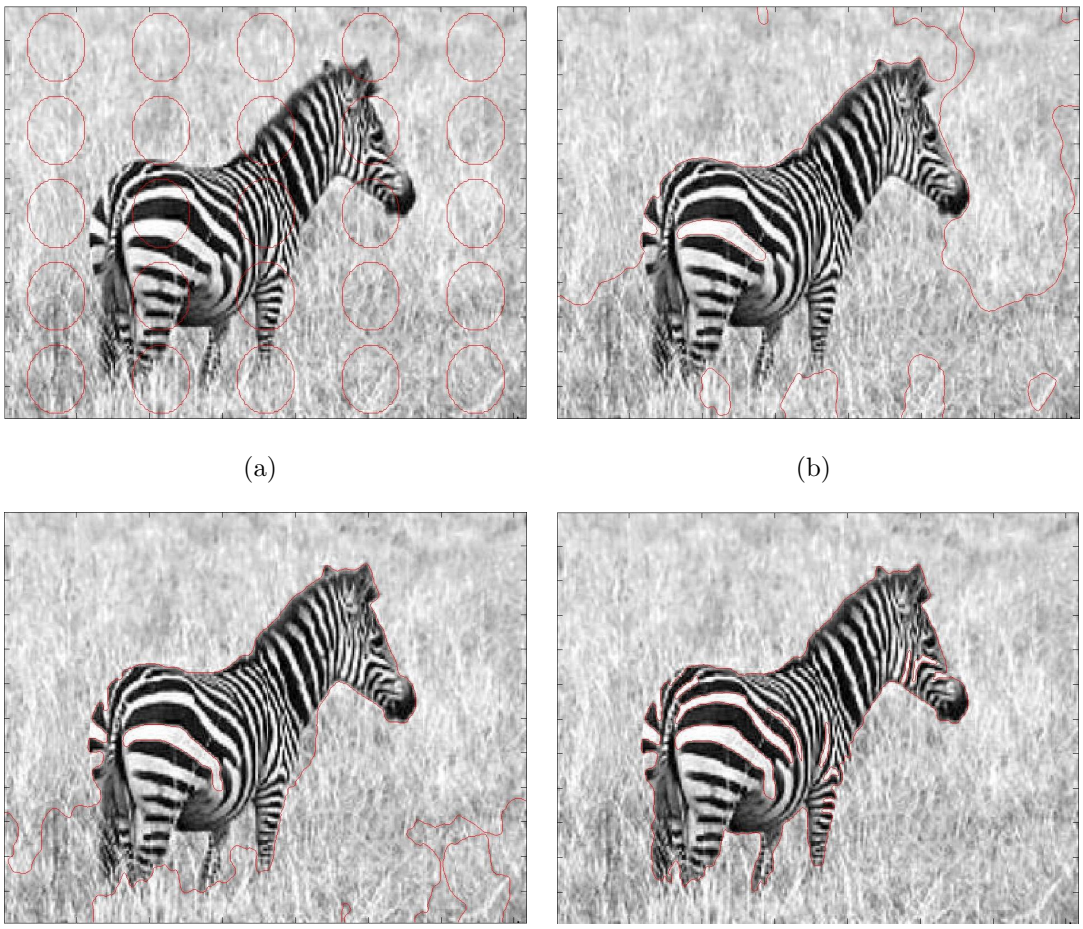

(a) (b)

(c) (d)

Figure 5.2: Zebra-2 image, CV method. (a) Initial contour. (b)- (c)- (d) 2000, 4000, 6200 iterations (1490 s).

5.1.3 Experiment III

In Figure 5.3, a highly textured house image is segmented. Parameters of the CV model are adjusted to $\mu = 4000$ and $\alpha = 1$. The method segments the image into two regions by mean intensity difference but it does not detect the object in the scene.

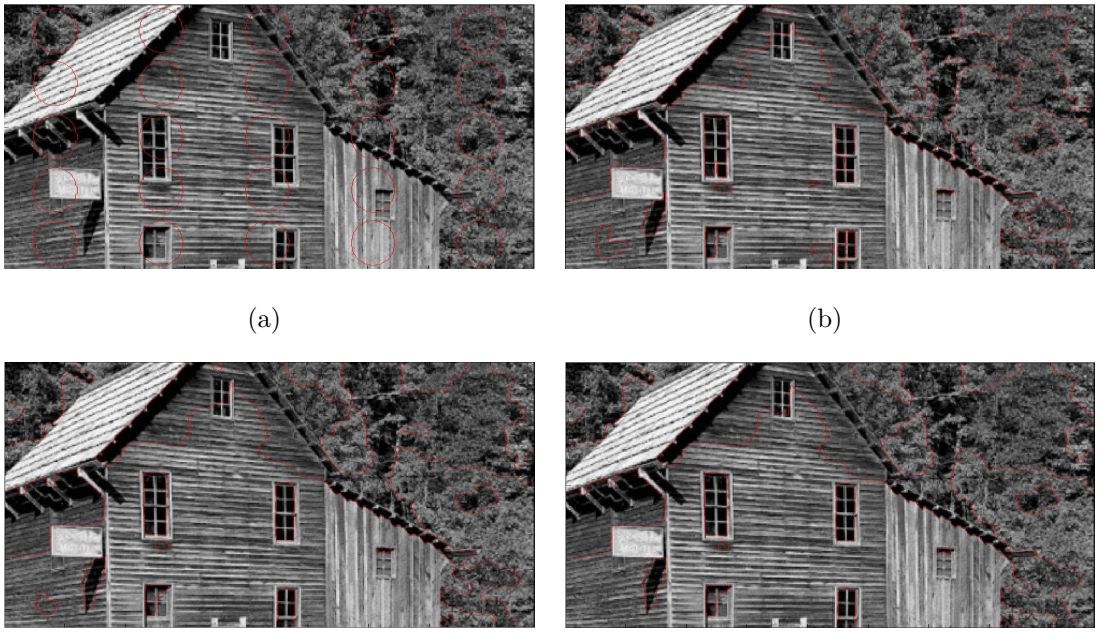

(a) (b)

(c) (d)

Figure 5.3: House image, CV method. (a) Initial contour. (b)- (c)- (d) 667, 1333, 2000 iterations. (255 s).

5.1.4 Experiment IV

In Figure 5.4, a textured cheetah image is segmented. Since the mean values of object and background are near to each other, the image is not successfully segmented by the CV method. Parameter of the model are $\mu = 50$ and $\alpha = 1$.

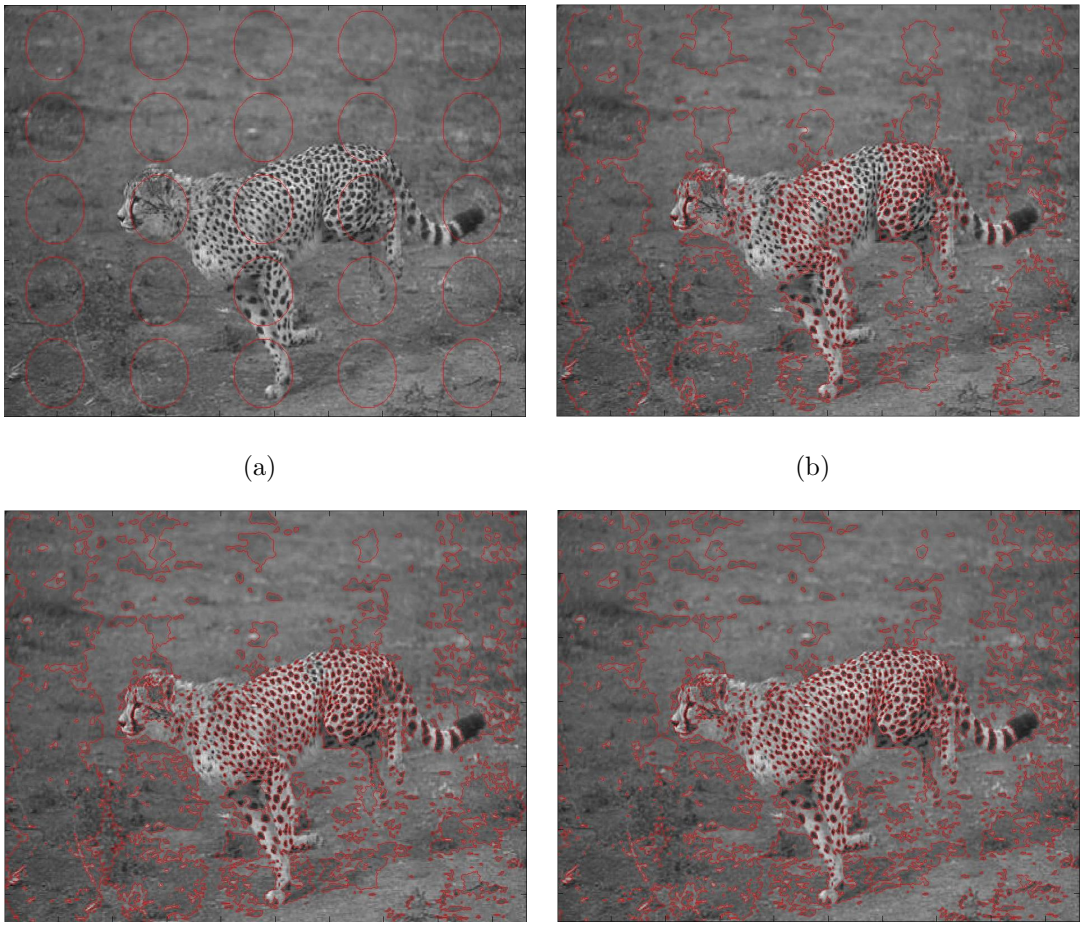

(a) (b)

(c) (d)

Figure 5.4: Cheetah image, CV method. (a) Initial contour. (b)- (c)- (d) 67, 133, 200 iterations (176 s).

5.2 EFFECT OF PRE-FILTERING IN ACTIVE CONTOURS

Nonlinear diffusion filtering is an effective method to smooth images while preserving edges. Using nonlinear diffusion filtering as a pre-filtering scheme, small scale details in textured regions are smoothed out so that the performance of the CV active contour method increases for textured images which can be decomposed into regions with distinct mean intensities.

5.2.1 Experiment I

The performance of the CV method with nonlinear diffusion filtering as a pre-filtering scheme is tested with a zebra image. Performance is better than the case where we only used the CV method, i.e., method does not fail at striped of zebra. Parameters are $\lambda = 200$, $\mu = 1000$ and 100 iterations of nonlinear diffusion and 600 iterations of the CV method are performed. The only inaccuracy of the segmentation is at the upper part of the zebra. The result is shown in Figure 5.5.

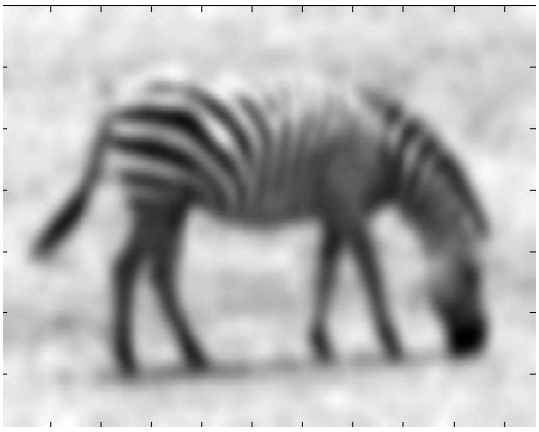

(a)

(b)

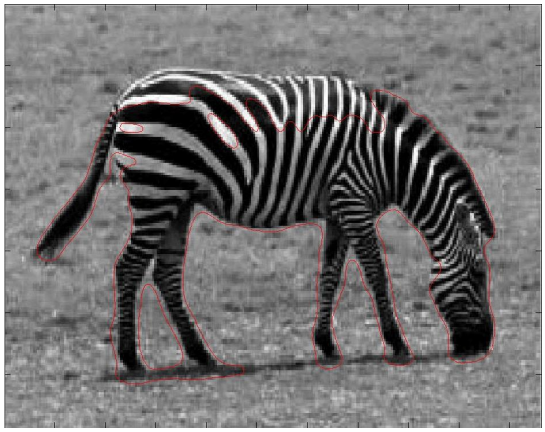

(c)

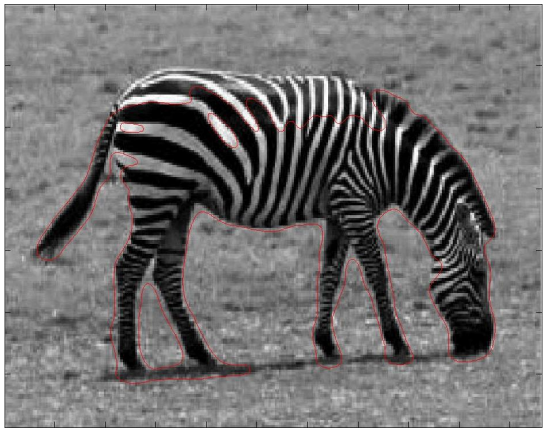

(d)

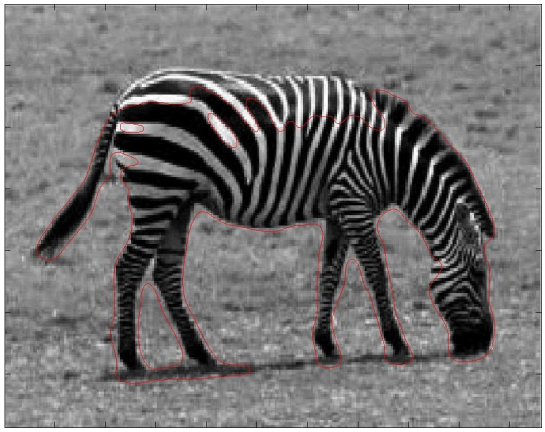

(e)

Figure 5.5: Effect of pre-filtering, zebra-1 image. (a) Nonlinear diffusion filtered image. (b) Initial contour. (c)- (d)- (e) 200, 400, 600 iterations (126.96 s).

5.2.2 Experiment II

The performance of the CV method with nonlinear diffusion filtering as a pre-filtering scheme is tested on another zebra image. Performance is better than the case where the image is segmented directly with the CV method. Parameters are chosen as $\mu = 6000$ and $\lambda = 250$. 100 iterations of nonlinear diffusion and 1200 iterations of the CV model are performed. The result is shown in Figure 5.6.

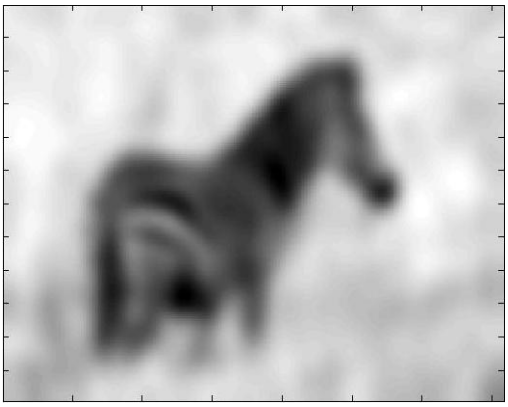

(a)

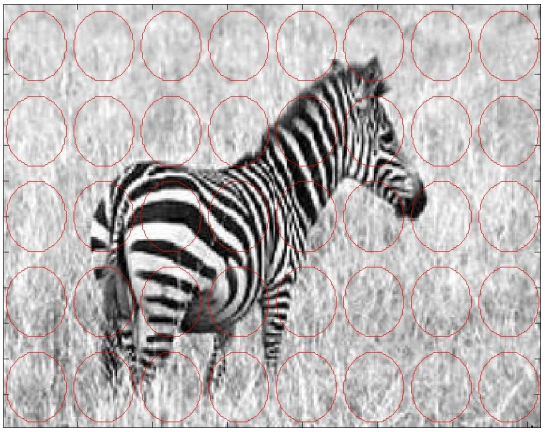

(b)

(c)

(d)

(e)

Figure 5.6: Effect of pre-filtering, zebra-2 image. (a) Nonlinear diffusion filtered image. (b) Initial contour. (c)- (d)- (e) 400, 800, 1200 iterations (527.3 s).

5.2.3 Experiment III

The performance of the CV method with nonlinear diffusion filtering used as a pre-filtering scheme is tested on a very highly textured house image. Neither this method nor the CV method could segment this image successfully. Parameters are $\mu = 3000$ and $\lambda = 50$. 100 iterations of nonlinear diffusion and 1000 iterations of the CV method are performed. The result is shown in Figure 5.7.

(a)

(b)

(c)

(d)

(e)

Figure 5.7: Effect of the pre-filtering scheme, house image. (a) Filtered image. (b) Initial contour. (c)- (d)- (e) 333, 666, 1000 iterations (123.1 s).

5.2.4 Experiment IV

The performance of the CV method with nonlinear diffusion filtering used as a pre-filtering scheme is tested on a very textured cheetah image. In this image, the object is not different from the background in terms of intensity but it has a different texture. Since there is not a great difference between mean values of object and background, neither this algorithm nor the CV method could segment this image successfully. Parameters are $\mu = 200$ and $\lambda = 50$. 100 iterations of nonlinear diffusion and 1000 iterations of the CV model are performed. The result is shown in Figure 5.8.

(a)

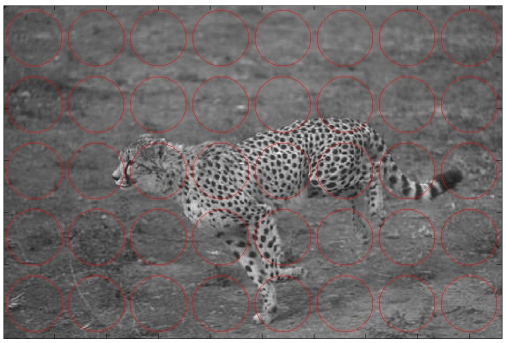

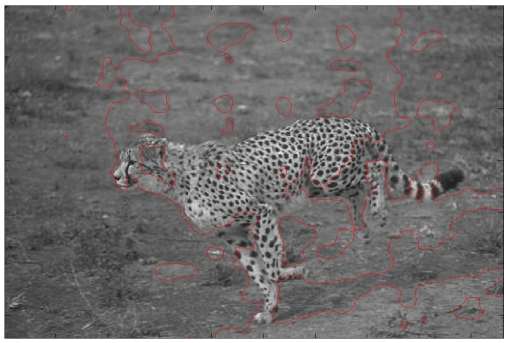

(b) (c)

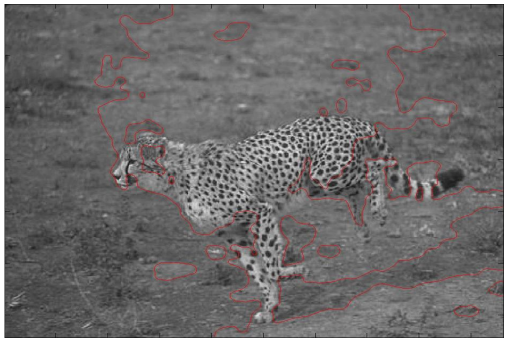

(d) (e)

Figure 5.8: Effect of the pre-filtering scheme, cheetah image. (a) Filtered image. (b) Initial contour. (c)- (d)- (e) 250, 500, 750 iterations (157 s).

5.3 GABOR SPACE CHAN-VESE ACTIVE CONTOURS

5.3.1 Method

An extension of the CV method is proposed in [22] in order to segment textured images. Textures are discriminated by constructing a Gabor feature space of the image. Firstly, the image function is convolved with different Gabor functions. Gabor functions of different frequencies, scales and orientation f, σ, θ are used to obtain different channels. Then some of the channels are selected by the user. The automatic selection technique of [22] is used in our implementation. In this technique, channels with maximum difference between object and background mean intensities are selected. Then, vector valued Chan-Vese method [27] segments the image. Even if some edges are missing at some channels, CV method extracts the object by using multi-channel information. Input to N-channel CV method are Gabor responses denoted by $u = u(1)$, $u(2)$, ..., $u(N)$. Multi channel CV method is given in equation 5.1. Parameters of the method are ν, $w_1(1)$, $w_1(2)$, ..., $w_1(N)$ and $w_2(1)$, $w_2(2)$, ..., $w_2(N)$.

$$E_{CV}(c_1, c_2, \Gamma) = \int_{\omega} \frac{1}{N} w_1(i) \sum_{i=1}^{N} |u(i) - c_1(i)|^2 dxdy + \int_{\Omega \setminus \omega} \frac{1}{N} w_2(i) \sum_{i=1}^{N} |u(i) - c_2(i)|^2 dxdy + \nu |\Gamma| \tag{5.1}$$

A Gabor filter with frequency f, scale σ and orientation θ is given below:

$$h(x, y) = g(x', y') \, exp(2\pi i F x') \tag{5.2}$$

where

$$(x', y') = (x \cos(\phi) + y \sin(\phi), -x \sin(\phi) + y \cos(\phi)) \tag{5.3}$$

and

$$g(x, y) = \frac{1}{2\pi\sigma^2} \exp\left(-\frac{x^2}{2\lambda_G^2 \sigma^2} - \frac{y^2}{2\sigma^2}\right). \tag{5.4}$$

A feature space of the image is obtained by convolving the image u_0 with Gabor function as

$$W = h \star u_0. \tag{5.5}$$

Magnitude of the Gabor transforms will be used as the Gaborian feature space. The parameter λ_G shows the aspect ratio of the elliptic Gaussian window and it is chosen as 2 in the experiments.

5.3.2 Experiments

5.3.2.1 Experiment I

Parameters of Gabor filters are chosen as follows: for 1^{st} channel, $f = 0.0012$, $\sigma = 3.0096$, $\theta = 1.83\,rad$, for 2^{nd} channel, $f = 0.3800$, $\sigma = 0.6991$, $\theta = 1.83\,rad$, for 3^{rd} channel, $f = 0.3800$, $\sigma = 0.6991$, $\theta = 2.36\,rad$ and for 4^{th} channel, $f = 0.1$, $\sigma = 4.011$, $\theta = 3.07\,rad$. Gabor responses are shown in Figure 5.9.

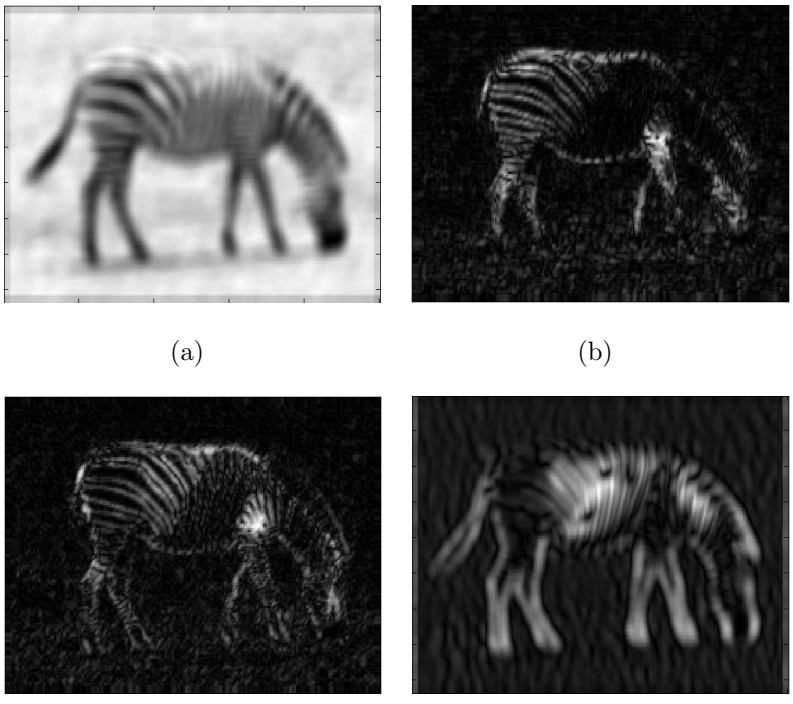

(a) (b)

(c) (d)

Figure 5.9: 4 channels of Gabor transforms.

The result of the image segmentation by the CV active contour method which is initialized with seeds is shown in Figure 5.10 (the parameters of the CV model are $\mu = 4000$, $w_1 = [0.8, 4, 4, 2]$ and $w_2 = [0.7, 3.5, 3.5, 1.75]$). The result is almost satisfactory. Only inaccuracy of the method is that the found object by the final contour widens unnecessarily at legs of the zebra. Convolution of the image with Gabor filters is responsible for this widening effect.

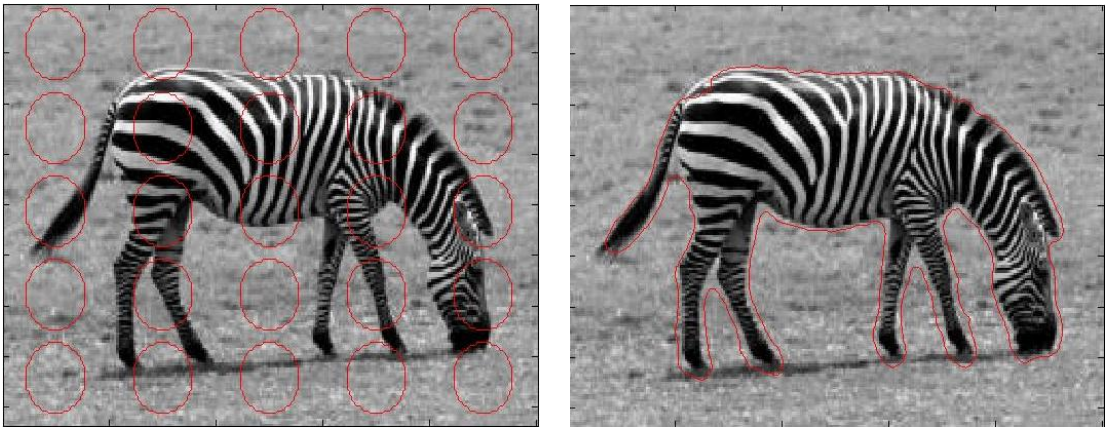

(a) (b)

Figure 5.10: Gabor space CV method, zebra-1 image. (a) Initial curve. (b) 1800 iterations.

5.3.2.2 Experiment II

An experiment is done on another textured zebra image. Selected angle, frequency, and scale of Gabor functions in the experiment are as follows: for 1^{st} channel, $f = 0.7952$, $\sigma = 1.3784$, $\theta = 1.3784\,rad$, for 2^{nd} channel, $f = 0.6463$, $\sigma = 2.9852$, $\theta = 2.9852\,rad$, for 3^{rd} channel, $f = 0.6463$, $\sigma = 1.3784$, $\theta = 1.3784\,rad$, for 4^{th} channel, $f = 0.2238$, $\sigma = 7.5127$, $\theta = 2.0581\,rad$ and for 5^{th} channel $f = 0.4733$, $\sigma = 3.5166$, $\theta = 1.3784\,rad$. The parameters of the CV active contour method are adjusted to $w_1 = [1,\ 1,\ 2,\ 3,\ 0.8,\ 0.8]$, $w_2 = [0.8,\ 0.8,\ 1.6,\ 1.6,\ 0.6,\ 0.6]$ and $\mu = 2400$. First 5 channels are Gabor responses and last channel is the original image. Segmentation result is satisfactory and the active contour is not misguided at the stripes of the zebra. First 5 channels of Gabor responses are shown in Figure 5.11. Initial and final contours are shown in Figure 5.12.

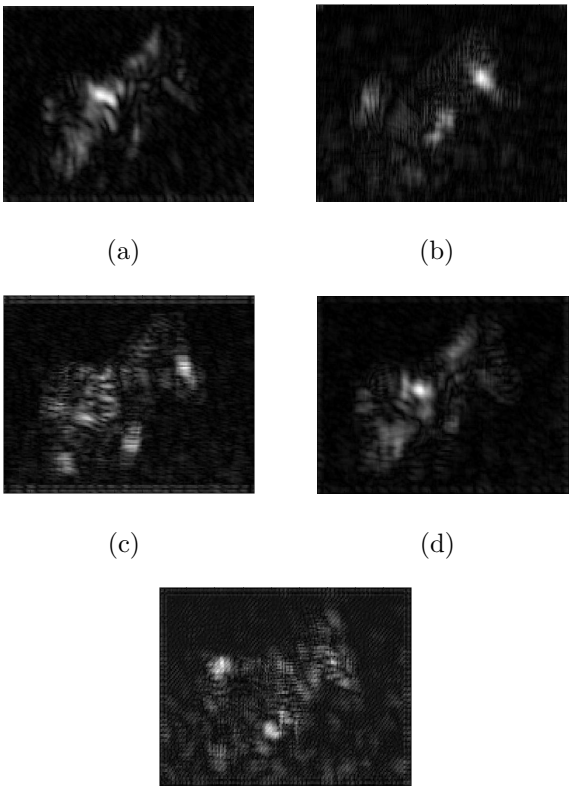

(a) (b) (c) (d) (e)

Figure 5.11: 5 channel Gabor Responses.

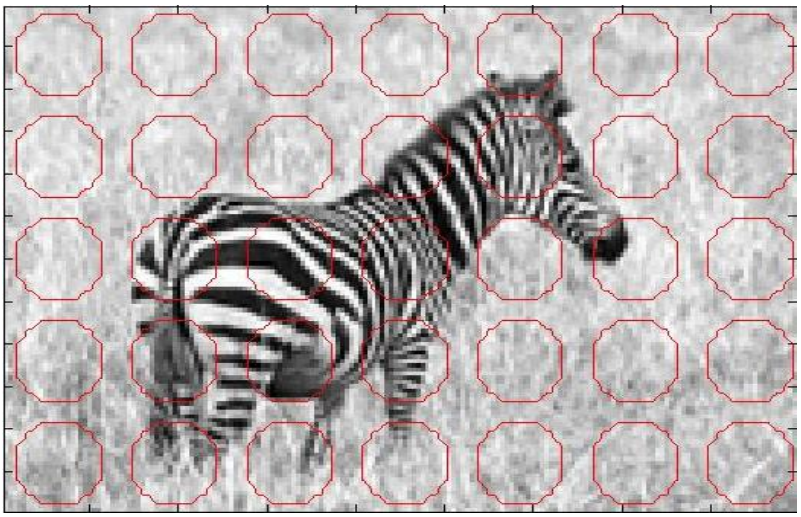

(a)

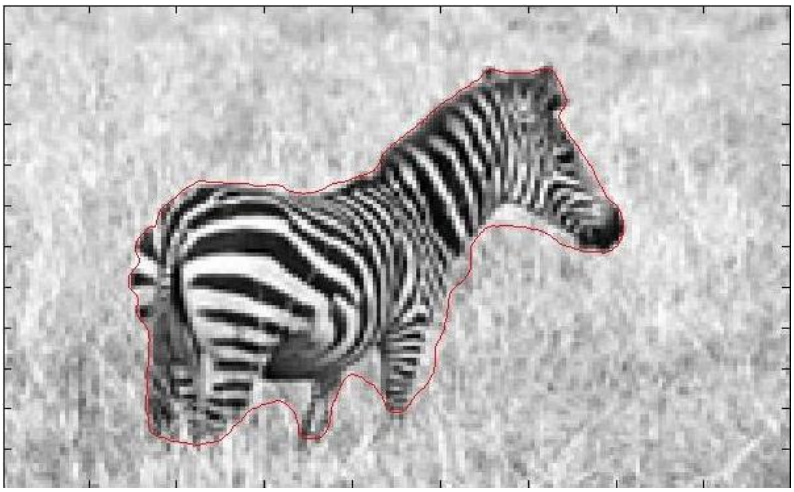

(b)

Figure 5.12: Gabor space CV method, zebra-2 image. (a)Initial contour. (b) 1400 iterations.

5.3.2.3 Experiment III

Some experiments are done on a textured house image. Selected angle, frequency, and scale of Gabor functions in the experiment are as follows: for 1^{st} channel, $f = 0.8693$, $\sigma = 2.8985$, $\theta = 0.8288\,rad$, for 2^{nd} channel, $f = 0.5499$, $\sigma = 0.7248$, $\theta = 0.5713\,rad$, for 3^{rd} channel, $f = 0.0351$, $\sigma = 2.5662$, $\theta = 0.4275\,rad$, for 4^{th} channel, $f = 0.7922$, $\sigma = 4.7975$, $\theta = 1.5249\,rad$. It is seen that a large part of house object in the image is found by the active contour. The result is better than results of all other methods for this house image. Parameters are adjusted to $w_1 = [4,\ 4,\ 0.8,\ 2.4,\ 2.4]$, $w_2 = [3,\ 3,\ 0.6,\ 1.8,\ 1.8]$ and $\mu = 8000$. Gabor responses are shown in Figure 5.13. The initial and final contours are shown in Figure 5.14.

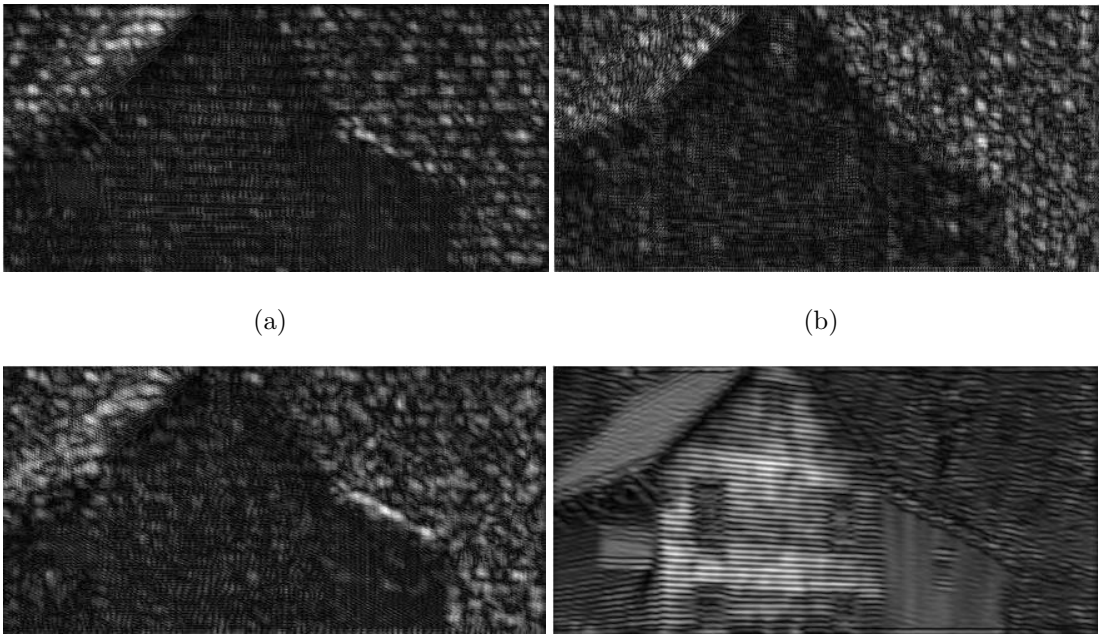

(a) (b)

(c) (d)

Figure 5.13: 4 channel Gabor Responses.

(a)

(b)

Figure 5.14: Gabor space CV method, house image. (a)Initial contour. (b) 2920 iterations.

5.3.2.4 Experiment IV

Some experiments are done on a textured cheetah image. The result is quite satisfactory such that only the tail of the zebra is missing at the final contour. The parameters of the CV model are adjusted to $w_1 = [1,\ 4\ ,8]$, $w_2 = [0.75,\ 3,\ 6]$ and $\mu = 16000$. Gabor responses are shown in Figure 5.15. The initial and final contours are shown in Figure 5.16.

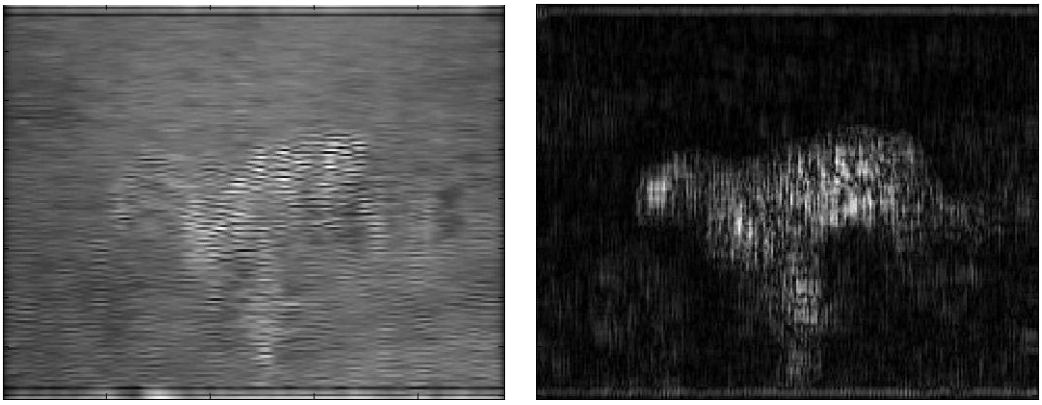

(a) (b)

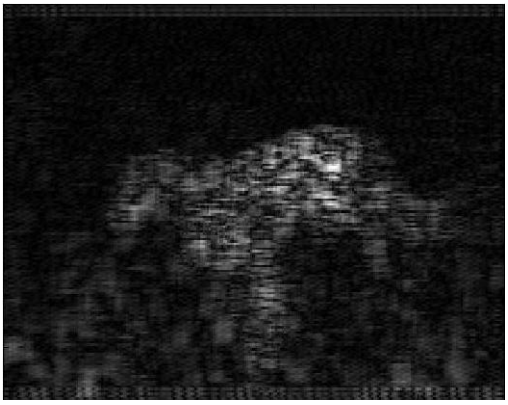

(c)

Figure 5.15: 3 channel Gabor responses.

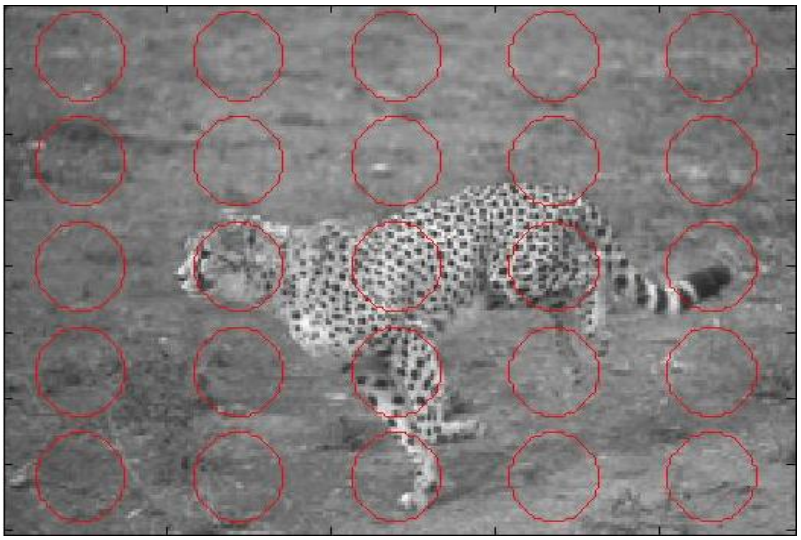

(a)

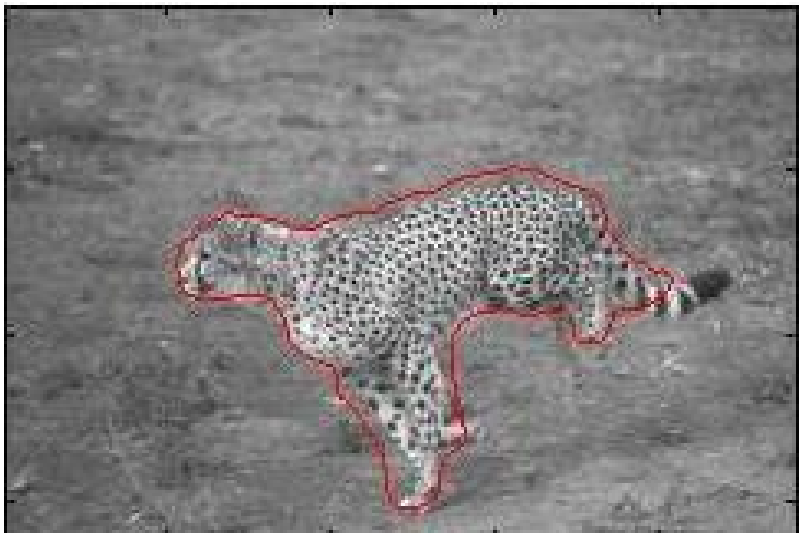

(b)

Figure 5.16: Gabor space CV method, cheetah image. (a)Initial contour. (b) 1200 iterations.

5.4 GABOR-SPACE GEODESICS ACTIVE CONTOURS

In edge-based image segmentation methods, edges are detected by a positive decreasing function which is low at edges, and high at inside of objects. In non textured images, gradient modulus is high at edges and low inside of objects. Therefore, edge detector function is defined as inversely proportional to gradient modulus. In textured image segmentation, gradient of image does not always indicate the presence of an edge. At textured regions, misguided by fine structures, gradient is high even inside of the object. The idea of [23] for textured image segmentation is to define a Gabor-space based edge detector function replacing the edge detector function which depend on image gradient in the geodesics active contour method.

5.4.1 Gabor Based Edge Detector

Local coordinates of image is denoted by (x, y). A Gabor filter with frequency f, scale σ and orientation θ is given in equation 5.2. In the Beltrami framework, a gray value image is viewed as a surface (2-dimensional manifold) embedded in a 3-dimensional space. Similarly, feature spaces of images, i.e., the Gaborian space can be also considered as a surface embedded in a higher dimensional space. The image is convolved with Gabor filters of different scale and orientation. Furthermore, the Gaborian feature space can be seen as a 2-D manifold embedded in 7-dimensional space $(x, y, \theta, \sigma, f, R, J)$ where θ, σ and f are the direction, scale and frequency for which a maximal Gabor response has been obtained and R and J denote the real and imaginary parts of the maximal magnitude Gabor response.

The metric g of embedding space is obtained by multiplying the transpose of the Jacobian of the mapping by itself. That is $g = J^T J$. Inverse of this metric's determinant can be used as an edge detector since the metric shows the rate of change of metric in a specific direction. The higher the metric of a pixel is, the bigger chance of getting an edge there one has.

In 2-dimensional images, an edge detector function is given by inverse of determinant of this metric:

$$g = \begin{bmatrix} 1 + Ix^2 & IxIy \\ IxIy & 1 + Iy^2 \end{bmatrix}.$$

In [28], an energy functional is proposed as $S(x, y, I) = \int det\,(g)\, dxdy$ for the aim of image smoothing. By applying a gradient descent process to this energy functional, a PDE equation, known as the Beltrami flow is obtained. The Beltrami flow serves as an directional edge preserving diffusion filter.

In the Gabor-space geodesic active contours method, the first step is filtering each feature channel of the Gabor feature space by the Beltrami flow so that textured edges can be more easily found by Gabor based edge detectors.

In the Gabor feature space of images, F^i denotes i^{th} channel of $(\theta, \sigma, f, R, J)$ and edge detector function is given by the inverse of the determinant of this metric:

$$g = \begin{bmatrix} 1 + \sum_i Fx^i Fx^i & \sum_i Fx^i Fy^i \\ \sum_i Fx^i Fy^i & 1 + \sum_i Fy^i Fy^i \end{bmatrix}.$$

5.4.2 Geodesics Active Contour Method

A popular active contour implemented by the level set method is the *geodesic active contour* model [3], where a new definition of curve length is introduced: it is weighted by an edge detector function. Replacing the edge detector function in the geodesic active contours method with the Gabor based edge detector denoted by E, a suitable scheme for textured image segmentation is obtained as given in equation 5.6.

$$\frac{\partial \phi}{\partial t} = |\nabla \phi|\, div\left(E \frac{\nabla \phi}{|\nabla \phi|}\right) \tag{5.6}$$

One may add an additional force that comes from an area minimization term known as the balloon force to this active contour method in order to direct the curve towards the objects. The PDE equation of the geodesics active contour method with additional balloon force is given in the equation 5.7. The weight of the balloon force is denoted by α_B.

$$\frac{\partial \phi}{\partial t} = |\nabla \phi| \left(div \left(E \frac{\nabla \phi}{|\nabla \phi|} \right) + \alpha_B E \right) \tag{5.7}$$

5.4.3 Experiments

5.4.3.1 Experiment 0

A simple experiment is done with a simple geometric test image to test the geodesic active contours method. In this experiment, Gabor based edge detector is not used. Parameters are chosen as follows: balloon force constant $\alpha = 0.5000$, the time step $\triangle t = 0.1$. 1800 iterations are done. Geodesic active contours method captures the object accurately as shown in Figure 5.17.

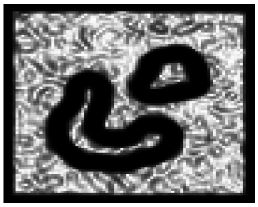

(a)

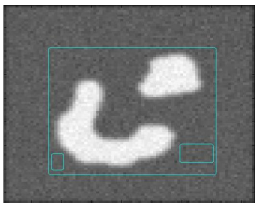

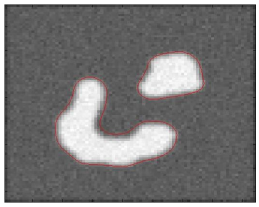

(b) (c)

Figure 5.17: Geodesics active contour method, a simple noisy geometric image. (a) Edge detector function. (b) Initial contour. (c) 1800 iterations.

5.4.3.2 Experiment I

The parameter set of the Gabor filters which are convolved with the zebra image is chosen as follows: $f = 0.4$, $\sigma = [0.9803,\ 0.9901,\ 1,\ 1.01,\ 1.0201,\ 1.0303]$, and $\theta = [0,\ \pi/12,\ 2\pi/12, 3\pi/12, 4\pi/12, 5\pi/12,\ 6\pi/12,\ 7\pi/12,\ 8\pi/12, 9\pi/12, 10\pi/12,\ 11\pi/12]$ respectively. In Figure 5.19, the initial curve is rectangle and the active contour does not converge to the legs of zebra. In Figure 5.20, the curve is initialized close to the object by subtracting some rectangles from it, however the final curve is not as close to the object boundaries as required.

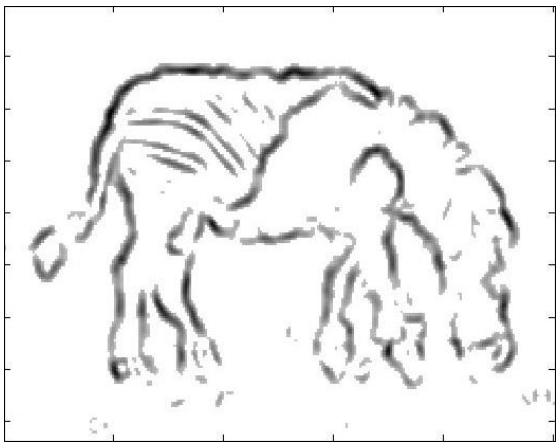

Figure 5.18: Edge detector function, zebra-1 image.

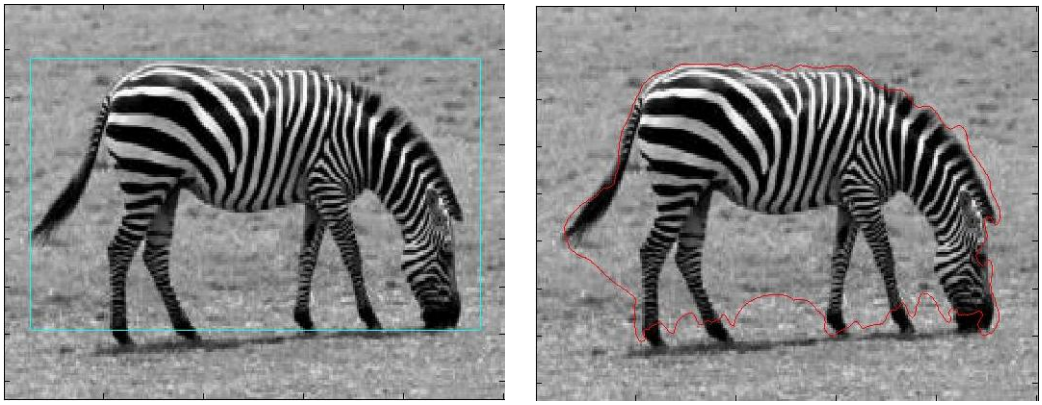

(a) (b)

Figure 5.19: Gabor-space geodesics active contour method, zebra-1 image. (a) Initial contour. (b) 18000 iterations. ($\alpha_B = 0.125$).

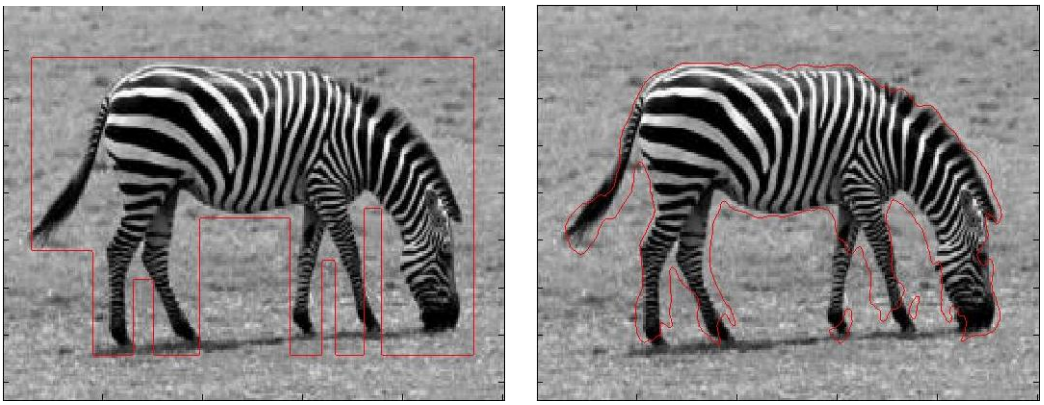

(a) (b)

Figure 5.20: Gabor-space geodesics active contour method, zebra-1 image. (a) Initial contour. (b) 12000 iterations. ($\alpha_B = 0.125$).

5.4.3.3 Experiment II

Another zebra image is segmented. The Gabor filter parameters are $f = 0.0828$, $\theta = [0, \pi/6, 2 * \pi/6, 3 * \pi/6, 4 * \pi/6, 5 * \pi/6]$ and $\sigma = [0.7946, 1.2040]$. Edge detector function is shown in Figure 5.21, the result of the active contour method is shown in Figure 5.22.

Figure 5.21: Edge detector function, zebra-2 image.

(a) (b)

Figure 5.22: Gabor-space geodesics active contour method, zebra-2 image. (a) Initial contour. (b) 4000 iterations.

5.4.3.4 Experiment III

A highly textured house image is segmented. The frequency of Gabor filters are $f = 0.2$, $\theta = [0, \pi/6, 2\pi/6, 3\pi/6, 4\pi/6, 5 * \pi/6]$ and this set of scales (σ) are chosen as [0.7333, 0.8147, 0.8962, 0.9777]. Edge detector function is shown in Figure 5.23, the result of active contour method is shown in Figure 5.24.

Figure 5.23: Edge detector function, house image.

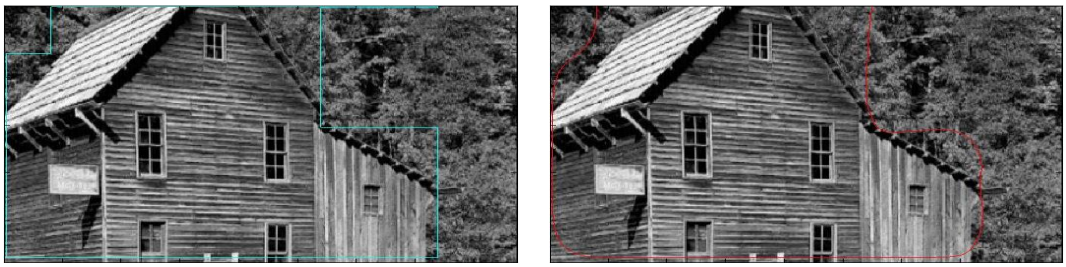

(a) (b)

Figure 5.24: Gabor-space geodesics active contour method, house image.
(a) Initial contour. (b) 2000 iterations.

5.4.3.5 Experiment IV

A highly textured cheetah image is input. The parameters of Gabor filters are $f = 0.2$, $\theta = [0, 0.37, 1.56, 1.93]$ (rad) and $\sigma = [0.8965, 0.9961, 1.0957, 1.1954]$. Edge detector function is shown in Figure 5.25, the unsuccessful segmentation result is shown in Figure 5.26.

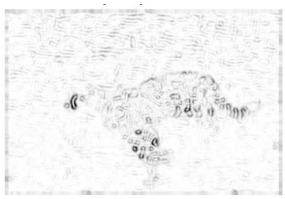

Figure 5.25: Edge detector function, cheetah image.

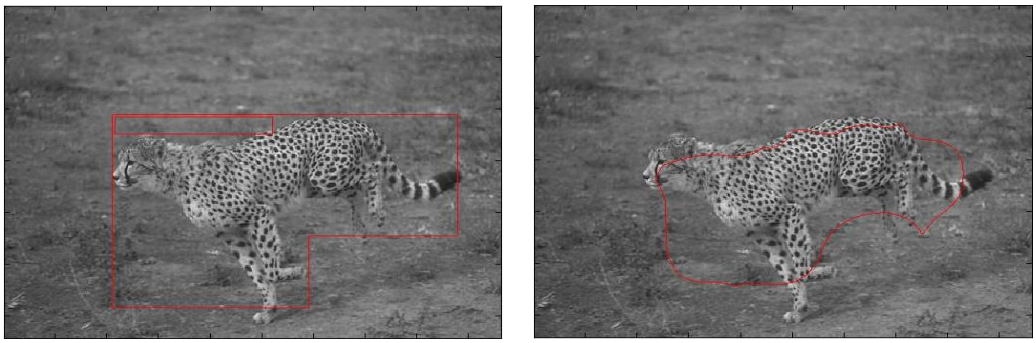

(a) (b)

Figure 5.26: Gabor-space geodesics active contour method, cheetah image. (a) Initial contour. (b) 2020 iterations ($\alpha_B = 0.2$).

5.4.4 Discussion

From the experiments, it can be concluded that segmentation results of the Gabor-space based geodesic active contours method are not satisfactory. In some experiments, the active contour does not detect all of the boundaries of the image, and in others, the active contour passes through the object without enclosing it.

It appears from the experiments that the edge detector function based on the Gabor-space fails to represent the object boundaries, perfectly. The fundamental reason of its failure that selection of maximal orientation and scale for which Gabor response is maximal does not help texture discrimination. In addition, the performance of different Gabor feature channels in the discrimination of textures varies as some of the feature channels does not satisfy the property of homogeneity within regions. An added difficulty of this method is the selection of suitable Gabor filter parameters. With different selections of the Gabor filter parameters, the performance of Gabor filters in discrimination of textures varies greatly.

Furthermore, there are some limitations of geodesic active contours method which create difficulties for enclosing the objects by the active contour. The capture range of geodesic active contours method is short and the curve cannot converge to the narrow concave parts of the boundary. This is due to the fact that the term which is responsible for locating the curve to the boundaries, is localized near the boundary. Therefore, one should add a balloon force to the geodesic active contours method to expand and shrink the curve. But, in this case, the contour is moved towards the objects boundaries by the balloon force and it stops at the low values of the edge detector function. Since the edge detector function obtained by this method is imperfect, the active contour does not converge to the boundaries.

CHAPTER 6

AMBROSIO - TORTORELLI APPOACH

6.1 AMBROSIO - TORTORELLI FUNCTIONAL

Due to the irregularity of the MS functional, it is impossible to minimize it in a straight forward way. To overcome the difficulties in the minimization process of the MS functional, it should be approximated by a regular functional in Γ-convergence framework. One such functional is given in equation 6.1: the AT functional. This functional Γ-converges to the MS functional as ρ goes to zero.

$$\lim_{\rho \to 0} E_{AT}(u, v) = E_{MS}(u, \Gamma)$$

$$E_{AT}(u,v) = \int_{\Omega} \left(\beta \left(u - u_0 \right)^2 + \alpha \left(\nu^2 |\nabla u|^2 \right) + \frac{1}{2} \left(\rho |\nabla v|^2 + \frac{(1-v)^2}{\rho} \right) \right) dxdy \tag{6.1}$$

In the AT approach, the discontinuity set Γ is removed from the functional and the edges are represented by a boundary function, v taking values between zero and one. If $(x, y) \in \Gamma$ then $v(x, y) = 0$ and if $(x, y) \notin \Gamma$ then $v(x, y) = 1$. As usual, the piecewise smooth function is represented by u. The AT functional is a regular functional, therefore standard techniques of calculus of variations are applicable for minimization of it.

The interpretation of AT functional is as follows: v is close to 0 if $|\nabla u|^2$ is large, and 1 otherwise. The edge detector variable v is smoothed by the third term $(\int_{\Omega} \rho |\nabla v|^2 dxdy)$ in the functional. Edge detector variable v controls the selective smoothing of image such that u is smoothed when $v = 1$ or $|\nabla u|^2$ is

small, smoothing is prevented when $v = 0$ or $|\nabla u|^2$ is large. Thus, the AT functional smoothes the image with edge preservation.

The calculus of variations provides the Euler–Lagrange equation of the AT functional and the gradient descent method gives the PDE equation that minimizes the functional as fast as possible, where t is an artificial time parameter (more details are given in Appendix F). The PDE equation for minimizing AT functional with respect to u is given in equation 6.2 and where equation 6.3 is the Neumann boundary condition and equation 6.4 is the initial condition. The PDE equation for minimizing AT functional with respect to v is given in equations 6.5 and where equation 6.6 is the Neumann boundary condition and equation 6.7 is the initial condition. The image segmentation problem is solved by alternating between the PDE equations associated with u and v.

$$\frac{\partial u}{\partial t} = \nabla \bullet (v^2 \nabla u) - \frac{\beta}{\alpha}(u - u_0) \tag{6.2}$$

$$\left.\frac{\partial u}{\partial n}\right|_{\partial\Omega} = 0 \tag{6.3}$$

$$u(x, y, 0) = u_0 \tag{6.4}$$

$$\frac{\partial v}{\partial t} = \nabla^2 v - \frac{2\alpha|\nabla u|^2 v}{\rho} - \frac{v - 1}{\rho^2} \tag{6.5}$$

$$\left.\frac{\partial v}{\partial n}\right|_{\partial\Omega} = 0 \tag{6.6}$$

$$v(x, y, 0) = \frac{1}{1 + 2\alpha\rho|\nabla u_0|^2} \tag{6.7}$$

The weights that control the balance between different entities of the functional are $\alpha,\ \beta$. One of the parameters in the MS model, ν is eliminated by setting it to 1. $\sqrt{\frac{\alpha}{\beta}}$ can be seen as the smoothing radius σ. If α and β is increased at the same time, the weight of the length penalty term in the MS functional is decreased and longer edges are found, hence a more detailed segmentation is obtained. At

steady state, $\nabla^2 v$ (the term which is responsible for smoothing of edge detector variable) does not effect the equation 6.5 much as noted by [29]. Ignoring the smoothing, we can get from 6.5 that $v = \frac{1}{1+2\alpha\rho|\nabla u|^2}$. Therefore, it is a good idea to initialize edge detector function as in 6.7. Comparing the Perona-Malik and the AT equations, it is clear that the contrast parameter λ in the AT model is given by $\sqrt{\frac{1}{2\alpha\rho}}$.

6.2 NUMERICAL SCHEMES

The AT equations are implemented with a suitable numerical scheme which is neither implicit, nor explicit. A 4 point scheme is used discretization of divergence term in [30], similar to numerical scheme in [14, 8]. But, in this study, 8 point scheme from [12] is used in the discretization of the divergence term.

Let $h = \triangle x = \triangle y$ be the space steps, let $\triangle t$ be the time step. Let the image be M by N. The following notations are used:

$$(x_i, y_j) = (ih,\ jh) \quad for\ 1 \leq i \leq M,\ 1 \leq j \leq N \tag{6.8}$$

$$u_0, i, j = u_0\,(x_i, y_j) \tag{6.9}$$

$$u^n_{i,j} = u(n\triangle t, x_i, y_j) \tag{6.10}$$

$$v^n_{i,j\pm 1/2} = \frac{v^n_{i,j\pm 1} + v^n_{i,j}}{2} \tag{6.11}$$

$$v^n_{i\pm 1/2,j} = \frac{v^n_{i\pm 1,j} + v^n_{i,j}}{2} \tag{6.12}$$

$$\left(|grad|^2\right)^n = \frac{1}{4}\left(\left(u^n_{i,j+1} - u^n_{i,j-1}\right)^2 + \left(u^n_{i+1,j} - u^n_{i-1,j}\right)^2\right) \tag{6.13}$$

A discrete form of Euler-Lagrange equations of the AT model is given in equations 6.14 and 6.15.

$$\begin{aligned}\frac{u_{i,j}^{n+1}-u_{i,j}^{n}}{\triangle t} = \alpha \big(& l_p * v_{i+1/2,j}^{n}\left(u_{i+1,j}^{n}-u_{i,j}^{n}\right) + l_p * v_{i-1/2,j}^{n}\left(u_{i-1,j}^{n}-u_{i,j}^{n}\right) \\ & l_p * v_{ppi,j+1/2}^{n}\left(u_{i,j+1}^{n}-u_{i,j}^{n}\right) + l_p * v_{i,j-1/2}^{n}\left(u_{i,j-1}^{n}-u_{i,j}^{n}\right) \\ & l_d * v_{i+1/2,j+1/2}^{n}\left(u_{i-1,j+1}^{n}-u_{i,j}^{n}\right) + l_d * v_{i-1/2,j-1/2}^{n}\left(u_{i-1,j-1}^{n}-u_{i,j}^{n}\right) \\ & l_d * v_{i+1/2,j+1/2}^{n}\left(u_{i+1,j+1}^{n}-u_{i,j}^{n}\right) + l_d * v_{i+1/2,j-1/2}^{n}\left(u_{i+1,j-1}^{n}-u_{i,j}^{n}\right)\big) \\ & -\beta \cdot \big(\left(u_{i,j}^{n+1}-u_{0_{i,j}}\right)\big)\end{aligned} \tag{6.14}$$

$$\begin{aligned}\frac{v_{i,j}^{n+1}-v_{i,j}^{n}}{\triangle t} = & \big(\left(v_{i+1,j}^{n}-v_{i,j}^{n}\right) + \left(v_{i-1,j}^{n}-v_{i,j}^{n}\right) \\ & \left(v_{i,j+1}^{n}-v_{i,j}^{n}\right) + \left(v_{i,j-1}^{n}-v_{i,j}^{n}\right)\big) \\ & - \frac{2\alpha}{\rho}\cdot\left(|grad|^2\right)^n v_{i,j}^{n+1} \\ & - \frac{\left(v_{i,j}^{n+1}-1\right)}{\rho^2}\end{aligned} \tag{6.15}$$

In the experiments, we choose $h = 1$ as usual. The condition on the time step for numerical stability is $\triangle t \leq 0.25$ and in experiments we choose $\triangle t = 0.25$ unless otherwise stated. In addition, in order to obtain a stable numerical scheme, $l_p + 2 * l_d = 1$ condition should be satisfied. In numerical experiments, l_p and l_d are chosen as $l_p = 0.5$ and $l_d = 0.25$.

6.3 SHAH'S UNIFIED FUNCTIONAL

Shah proposed a functional given in equation 6.17 in [31] as a $\Gamma-$convergent approximation to a Total Variation minimization [14] variant given in equation 6.16. In this functional, an edge exists if $(v \cong 1)$ and J_u represents the intensity jump across Γ .

$$E_{SHAH}(u,\Gamma) = \frac{\beta}{\alpha}\int_{\Omega}|u-u_0|\,dxdy + \int_{\Omega\setminus\Gamma}||\nabla u||\,dxdy + \int_{\Gamma}\frac{J_u}{1+\alpha J_u}ds \tag{6.16}$$

$$E_{SHAH,\rho}(u,v) = \int_{\Omega}\left(\beta\,|u-u_0| + \alpha\left((1-v)^2\,||\nabla u||\right) + \frac{1}{2}\left(\rho\,||\nabla v||^2 + \frac{v^2}{\rho}\right)\right)dxdy \tag{6.17}$$

Although this functional is very similar to the MS functional, one significant property Shah's functional has: shocks form in u and the set of discontinuities correspond to the object boundaries without being heavily misguided by the noise or the texture. This is due to usage of robust L_1 norm instead of L_2 norm in the data fidelity term. Optimum point of this functional is found via the half-quadratic minimization technique [32].

6.4 RESULTS

The AT model and the Shah model are tested on a real textured house image from [33] and noisy couple image from [30].

Using Shah's functional, the noisy couple image is smoothed and segmented. If parameters are chosen as $\alpha = 0.7$, $\beta = 0.007$, $\rho = 0.02$; the constructed edge set is detailed, noise is eliminated from the image and lady's head is separated from the background. In order to reduce the details, the parameters are chosen as $\alpha = 0.5$, $\beta = 0.005$, $\rho = 0.02$ and the lady's leg is lost in the background. The experiment is shown in Figure 6.1. Both of the segmentations have some unnecassary details like segmentation of the ground of the house into 3 parts.

(a)

(b) (c)

(d) (e)

Figure 6.1: Segmentation by the Shah functional, couple image. (a) Input image. (b)- (c) Smoothed image and edge set ($\alpha = 0.7$, $\beta = 0.007$, $\rho = 0.02$). (d)- (e) Smoothed image and edge set ($\alpha = 0.5$, $\beta = 0.005$, $\rho = 0.02$).

The noise is not completely eliminated by the AT model if parameters are chosen as $\alpha = 1$, $\beta = 0.001$, $\rho = 0.02$ and 10000 iterations are performed. The only solution is to increase the blurring radius by selecting $\alpha = 1$, $\beta = 0.00075$, $\rho = 0.02$; however in this case the lady's upper body part is lost after 1200 iterations of the AT method. The experiment is shown in Figure 6.2. Comparing the results, it seems that Shah's functional better segments noisy images without being effected by noise much.

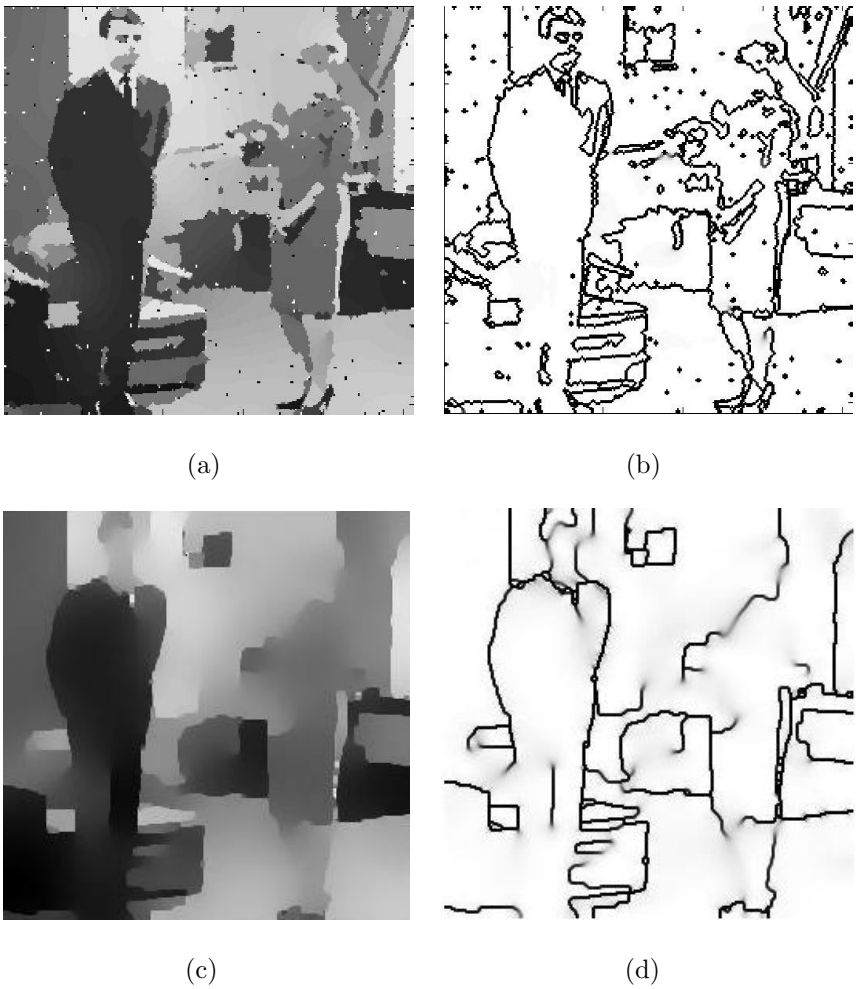

(a) (b)

(c) (d)

Figure 6.2: Segmentation by the AT model, couple image.

(a)- (b) Smooth image, edges ($\alpha = 1$, $\beta = 0.001$, $\rho = 0.02$, 1000 iterations).

(c)- (d) Smooth image, edges ($\alpha = 0.7$, $\beta = 0.00075$, $\rho = 0.02$, 1200 iterations).

A highly textured house image is input to the AT and Shah's unified segmentation models. In each case, the edge at the right side of the house is not found since the intensity discontinuity passes from inside of the house. With Shah's unified model, the cartoon limit is reached as shown in Figure 6.3.

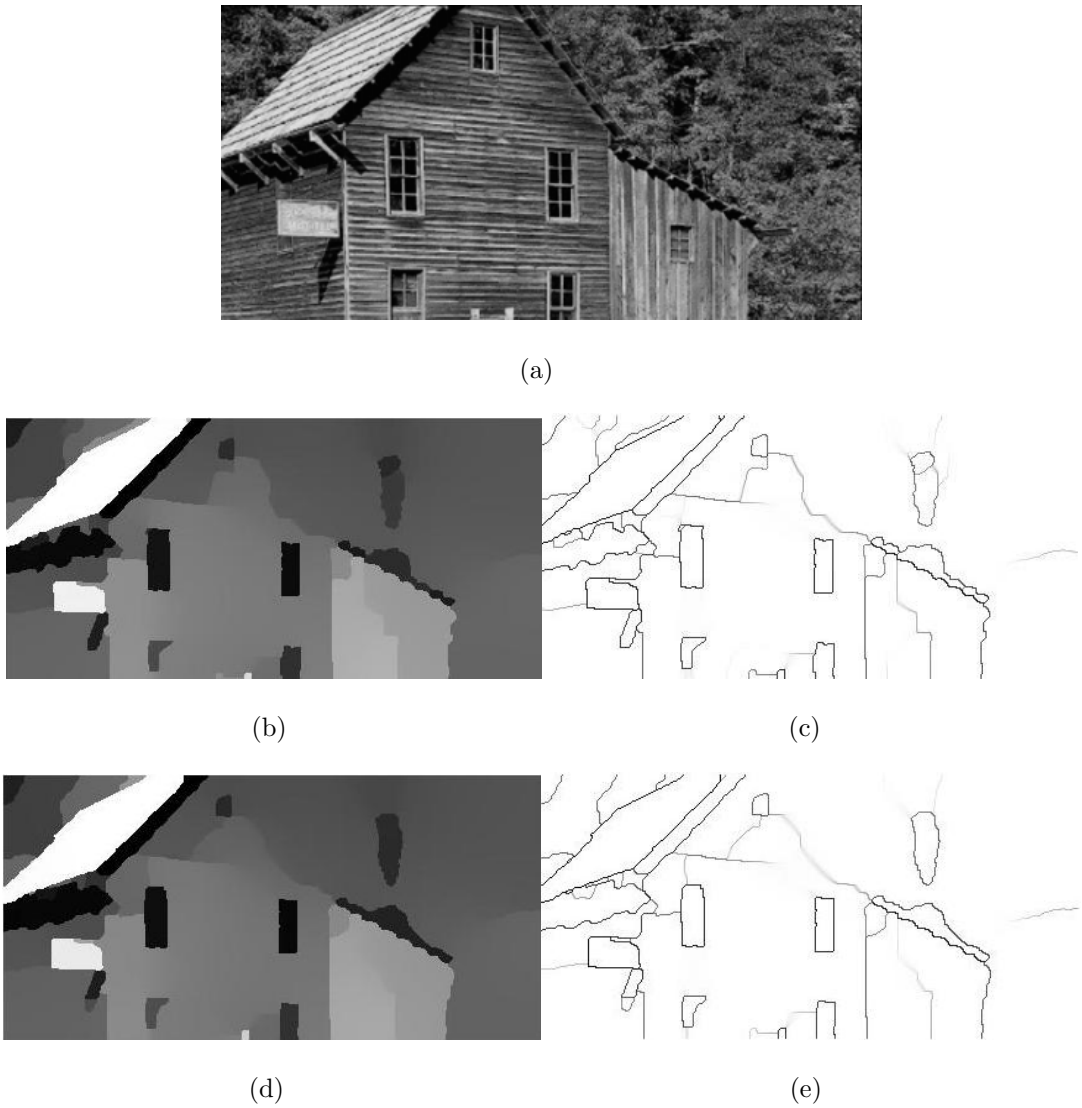

(a) (b) (c) (d) (e)

Figure 6.3: Segmentation by the Shah model, house image. (a) Original image. (b)- (c) Smooth image and edges ($\alpha = 0.5$, $\beta = 0.0005$, $\rho = 0.02$). (d)- (e) Smooth image and edges ($\alpha = 0.5$, $\beta = 0.0001$, $\rho = 0.02$).

The results of segmentation of the house image with the AT model are shown in Figure 6.4. At (a-b), smoothing radius is too large so that most of the edges are lost. The segmentation at (c-d) is detailed and some scale details of the image are not smoothed out. The least detailed segmentation is shown in (e-f).

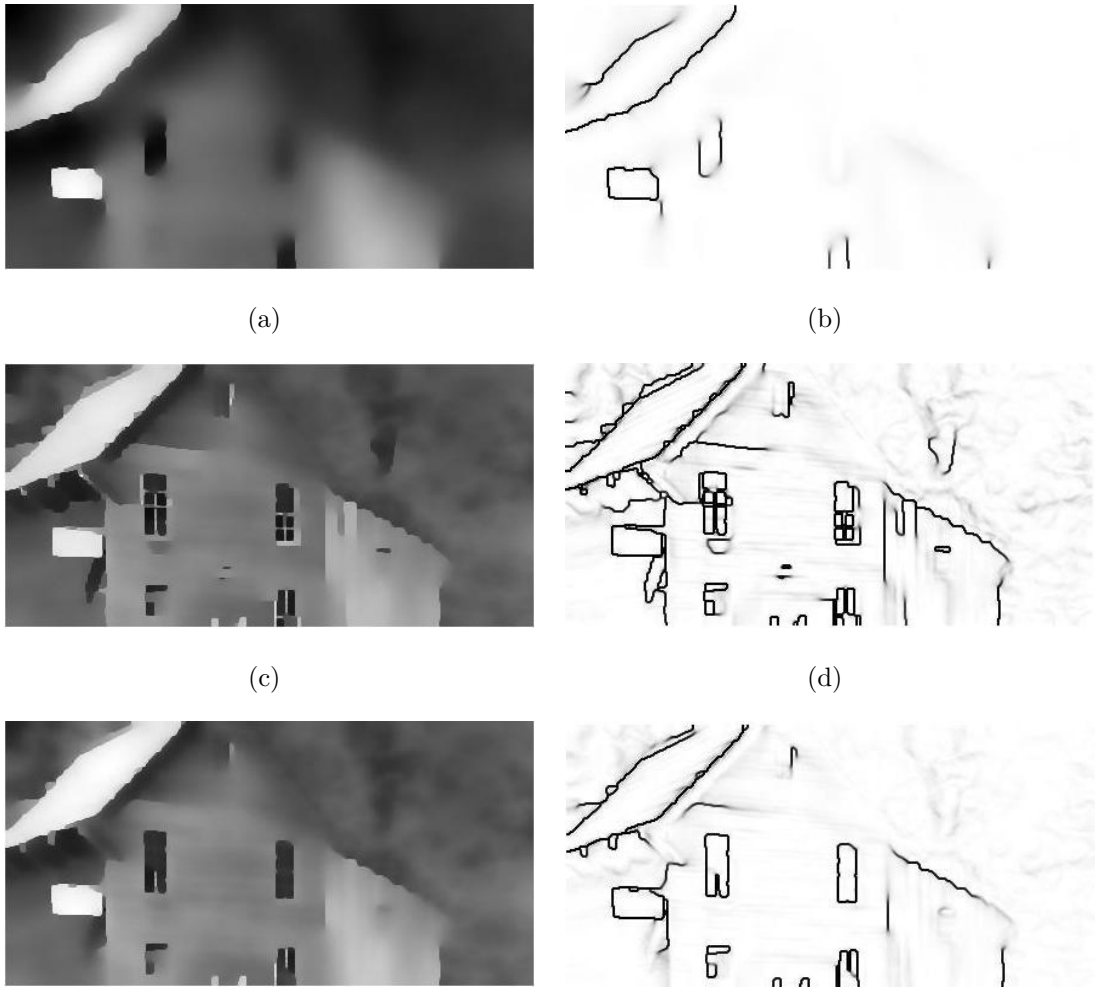

(a) (b)

(c) (d)

(e) (f)

Figure 6.4: Segmentation by the AT model, house image ($\rho = 0.02$ for all).
(a)- (b) $\alpha = 0.5$, $\beta = 0.0005$, 284 s. (c)- (d) $\alpha = 1$, $\beta = 0.01$, 405 s.
(e)- (f) $\alpha = 0.5$, $\beta = 0.005$, 220 s.

It can be concluded from the experimental results that the Shah model that uses L_1 norm is better than the AT model that uses L_2 norm at segmentation without being misguided by textures at the image.

6.5 LOCAL FEEDBACK INTO AT EQUATIONS

We propose to insert local neighbourhood information to right hand side of u and v PDE equations for segmentation of images which cannot be accurately segmented by the MS model. This operation is named as the local state feedback.

6.5.1 Local Feedback into u PDE equation

Euler-Lagrange equations which minimize the AT energy with respect to u with feedback added to right hand side of the equation are given below:

$$\frac{\partial u}{\partial t} = \nabla \bullet (v^2 \nabla u) - \frac{\beta}{\alpha}(u - u_0) + K_u\,(u_{Ref} - u) \tag{6.18}$$

$$\frac{\partial u}{\partial n}\,|_{\partial\Omega} = 0 \tag{6.19}$$

Local state feedback into u PDE equation is inserted to increase the smoothing of u function. Based on the control theory, a local operation by sliding neighbourhood operations which is similar to proportional feedback is used as local feedback. A 3-by-3 neighborhood block slides over the image and the reference value ($uRef$) for the center in each 3-by-3 block is taken as the average of pixel values in this block. The proportional feedback term for the PDE equation associated with u is given by: $Kp * (uRef(i,j) - u(i,j))$ where Kp is a suitable constant, $u(i,j)$ is the value of the pixel (i,j) and $uRef(i,j)$ is the mean intensity of this pixel's 3-by-3 neighborhood.

Some experiments are done to test the method. Obtained images with AT and local feedback are shown in Figure 6.5 for $\Delta t = 0.10$ and $\Delta t = 0.20$. The parameters in the AT functional are adjusted to $\alpha = 0.5$, $\rho = 0.01$, $\beta = 0.005$, $K_u = 8$ and 40 iterations are done. If $\Delta t = 0.10$, numerical scheme is stable.

Increasing Δt, numerical scheme becomes unstable. As seen in Figure 6.5, after inserting local feedback term, smoothing in the textured regions are increased and algorithm does not find some of the false edges in the textured regions. Filtered images contain inter-regional blurring since feedback term which does not depend on v, smooth the image without preventing smoothing across edges.

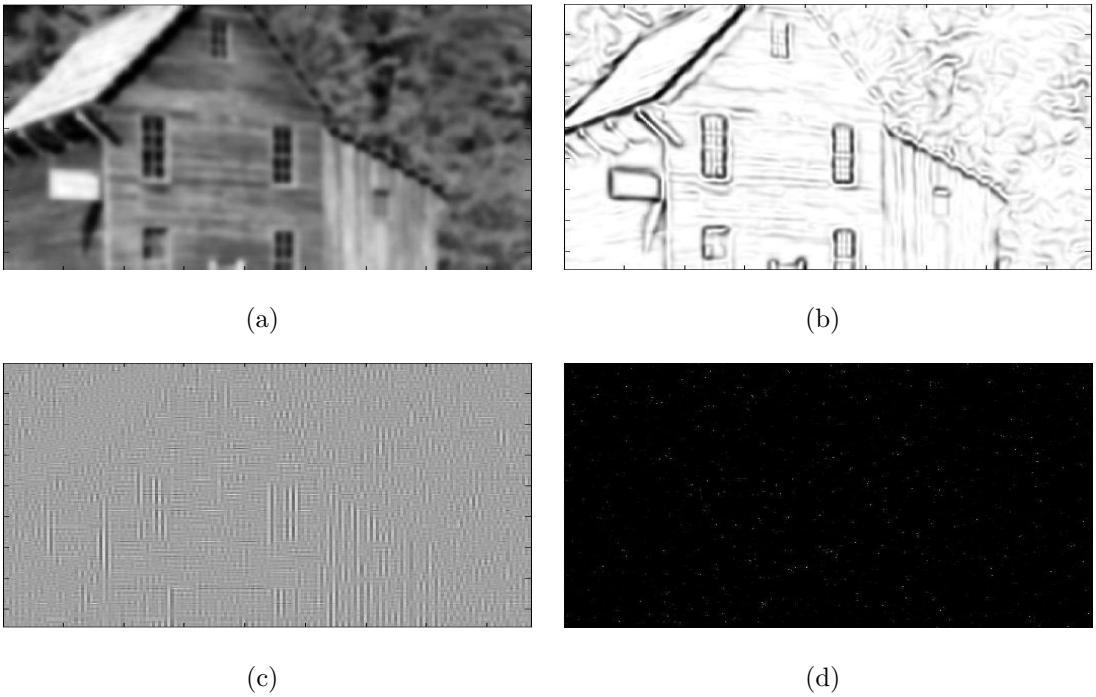

(a) (b)

(c) (d)

Figure 6.5: AT model with local feedback into u. (a)- (b) u, v ($\Delta t = 0.10$, 32 s). (c)- (d) u, v ($\Delta t = 0.20$, 34 s).

In fact, a similar operation to this feedback operation is also included in AT approach: $\int_\Omega \alpha\,(v^2|\nabla u|^2)\,dx$ term averages the values of 8 neighbours of the center pixel in 3-by-3 windows if v is taken 1 in the entire image. The result of multiplication of a 3-by-3 discrete normalized identity matrix (I) by K_u is denoted by IK. Note that the center of the matrix is taken away. A discrete form of AT PDE equations of u with feedback is given in equation 6.20.

$$
\begin{aligned}
\frac{u_{i,j}^{n+1}-u_{i,j}^{n}}{\triangle t} = \beta\cdot\left(u_{0_{i,j}}-u_{i,j}^{n+1}\right)+\alpha\Big(&\left(v_{i+1/2,j}^{n}+IK_{i+1,j}\right)\left(u_{i+1,j}^{n}-u_{i,j}^{n}\right)\\
&+\left(v_{i-1/2,j}^{n}+IK_{i-1,j}\right)\left(u_{i-1,j}^{n}-u_{i,j}^{n}\right)\\
&+\left(v_{i,j+1/2}^{n}+IK_{i,j+1}\right)\left(u_{i,j+1}^{n}-u_{i,j}^{n}\right)\\
&+\left(v_{i,j-1/2}^{n}+IK_{i,j-1}\right)\left(u_{i,j-1}^{n}-u_{i,j}^{n}\right)\\
&+\left(v_{i-1/2,j+1/2}^{n}+IK_{i-1,j+1}\right)\left(u_{i-1,j+1}^{n}-u_{i,j}^{n}\right)\\
&+\left(v_{i-1/2,j-1/2}^{n}+IK_{i-1,j-1}\right)\left(u_{i-1,j-1}^{n}-u_{i,j}^{n}\right)\\
&+\left(v_{i+1/2,j+1/2}^{n}+IK_{i+1,j+1}\right)\left(u_{i+1,j+1}^{n}-u_{i,j}^{n}\right)\\
&+\left(v_{i+1/2,j-1/2}^{n}+IK_{i+1,j-1}\right)\left(u_{i+1,j-1}^{n}-u_{i,j}^{n}\right)\Big)
\end{aligned}
\tag{6.20}
$$

The only difference between the scheme with feedback and without feedback is that in feedback operation 8 neighbours of center pixel in each 3-by-3 window is averaged equally without depending on v. Therefore, we expect to obtain similar results to AT with feedback operation if we take $v = 1$ in whole image domain and choose $\Delta t = 0.20$ in PDE equation associated with u without using the feedback term. The results of this case can be seen in Figure 6.6.

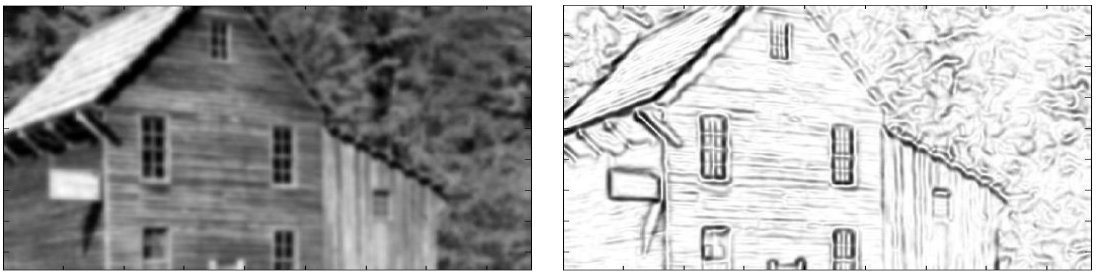

(a) (b)

Figure 6.6: Segmentation by the AT model without control of u by v. (a) u. (b) v at $\Delta t = 0.20$ (40 iterations) (18.5s).

In the local feedback operation, averaging results in regularization without edge preservation and this causes inter-regional blurring. In the experiments,

average pixel values of 3 by 3 neighbourhood of each pixel is used as a feedback term, that is equivalent to taking $Ku = 8$ and $I = \begin{bmatrix} 1/9 & 1/9 & 1/9 \\ 1/9 & & 1/9 \\ 1/9 & 1/9 & 1/9 \end{bmatrix}$ in equation 6.20. But, if we take $Ku = 8$ and $I = \begin{bmatrix} 1/32 & 1/16 & 1/32 \\ 1/16 & & 1/16 \\ 1/32 & 1/16 & 1/32 \end{bmatrix}$ we can see that numerical scheme of the modified form of the AT PDE equation associated with u is nothing but numerical minimization of this functional:

$$E(u,v) = \int_\Omega \left(\beta \left(u - u_0\right)^2 + \alpha \left(\left[v^2 + 1\right] |\nabla u|^2 \right) + \frac{1}{2} \left(\rho |\nabla v|^2 + \frac{(1-v)^2}{\rho} \right) \right) dxdy.$$

If $|\nabla u|^2$ is large at any pixel, $v = 0$ and the AT model inhibits diffusion around that pixel, but $(v^2 + 1) = 1$ and the AT model with the feedback scheme allows diffusion around that pixel. Regularization without edge preservation is not an appropriate idea generally, because of the dislocation of the edge set by blurring.

Another experiment is done on the noisy couple image. At this image, the edge set is not located properly because of the blurring at edges as shown in Figure 6.7. The result of segmentation with the AT model is shown in Figure 6.2.

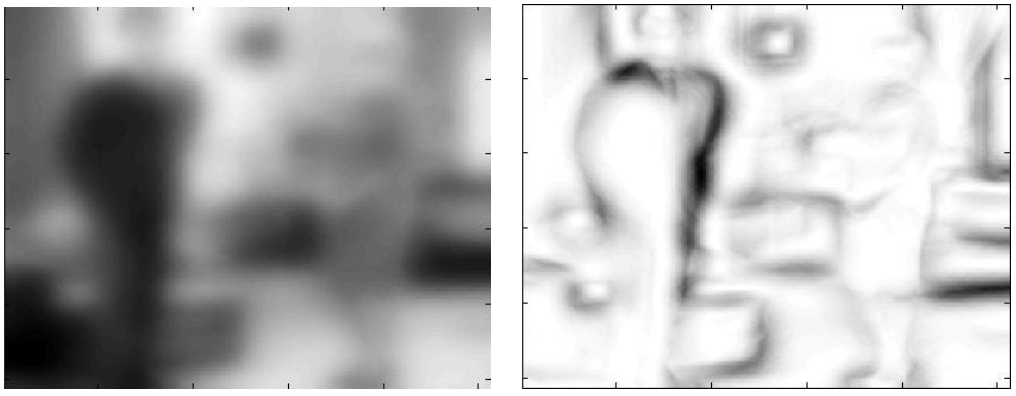

(a) (b)

Figure 6.7: Segmentation by the AT model with feedback operation, noisy couple image. (a) u (b) v ($\alpha = 0.3$, $\rho = 0.005$, $\beta = 0.005$) (150 iterations, 21.25 s).

6.5.2 Local Feedback into v PDE Equation

In the local feedback operation for the PDE equation associated with v, finding edges in local neighbourhood as lines and adding this information as a local state feedback to right hand side of v PDE equation is considered. An artificial reference ($vRef$ function) is obtained from each 5-by-5 neighborhood block of v function. Our method consists of dividing each 5-by-5 block into 2 regions using gradient direction at the center pixel. In every 5-by-5 block, feedback term at the pixels considered as edges are set to 0 and feedback term at remaining pixels is set to 1. We calculate 5-by-5 $vRef$ function as follows: The pixel values in the line perpendicular to gradient are set to 0 and values of other pixels in the window are set to 1. Similar to proportional feedback, we obtain 5-by-5 feedback term for v as: $vRef - v$. We should obtain feedback term for only the center pixel in the 5-by-5 block, therefore we multiply 5-by-5 $vRef - v$ by a 5-by-5 Gaussian kernel, element by element to emphasize the center pixel. Then, this value is multiplied by a suitable constant Kv and the elements of the resultant matrix is summed. At the summing operation, directional edge information is lost. We generally adjust $1/\rho^2$ and Kv equal or near to each other.

$$\frac{\partial v}{\partial t} = \nabla^2 v - \frac{2\alpha|\nabla u|^2 v}{\rho} - \frac{v-1}{\rho^2} + K_v\,(v_{Ref} - v) \tag{6.21}$$

$$\frac{\partial v}{\partial n}\,|_{\partial\Omega} = 0 \tag{6.22}$$

Some experiments are done on the house image by using the 5-by-5 feedback term for v: $vRef - v$. In Figure 6.8, u function, v function at previous step, $vRef$ function, feedback term and v function at next step at the 1^{st} iteration are shown respectively. In Figure 6.9 results at the 11^{th} iteration, in Figure 6.10 results at the 21^{st} iteration are shown. In Figure 6.11, obtained u and v functions after 40 iterations are shown.

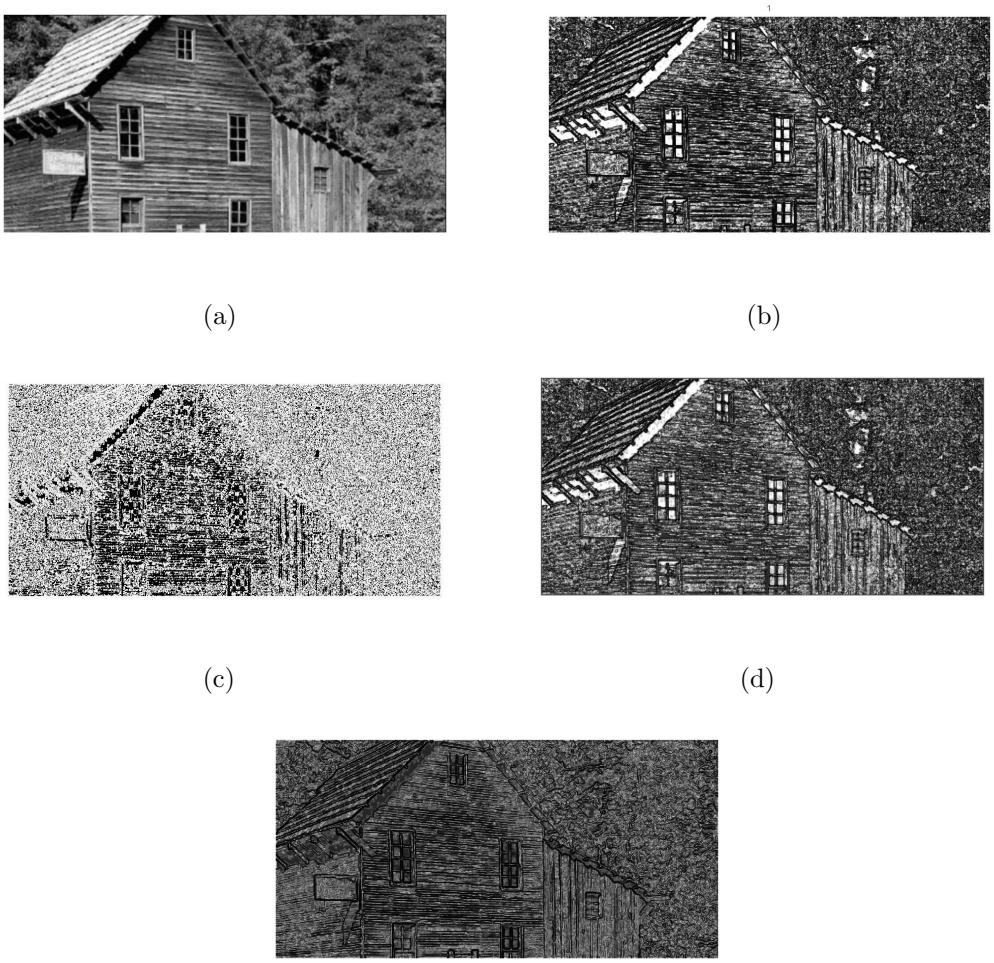

(a) (b)

(c) (d)

(e)

Figure 6.8: 1^{st} iteration of the AT equation with u and v feedback. (a) u^{n+1}. (b) v^n. (c) $vRef$. (d) Feedback term. (e) v^{n+1}.

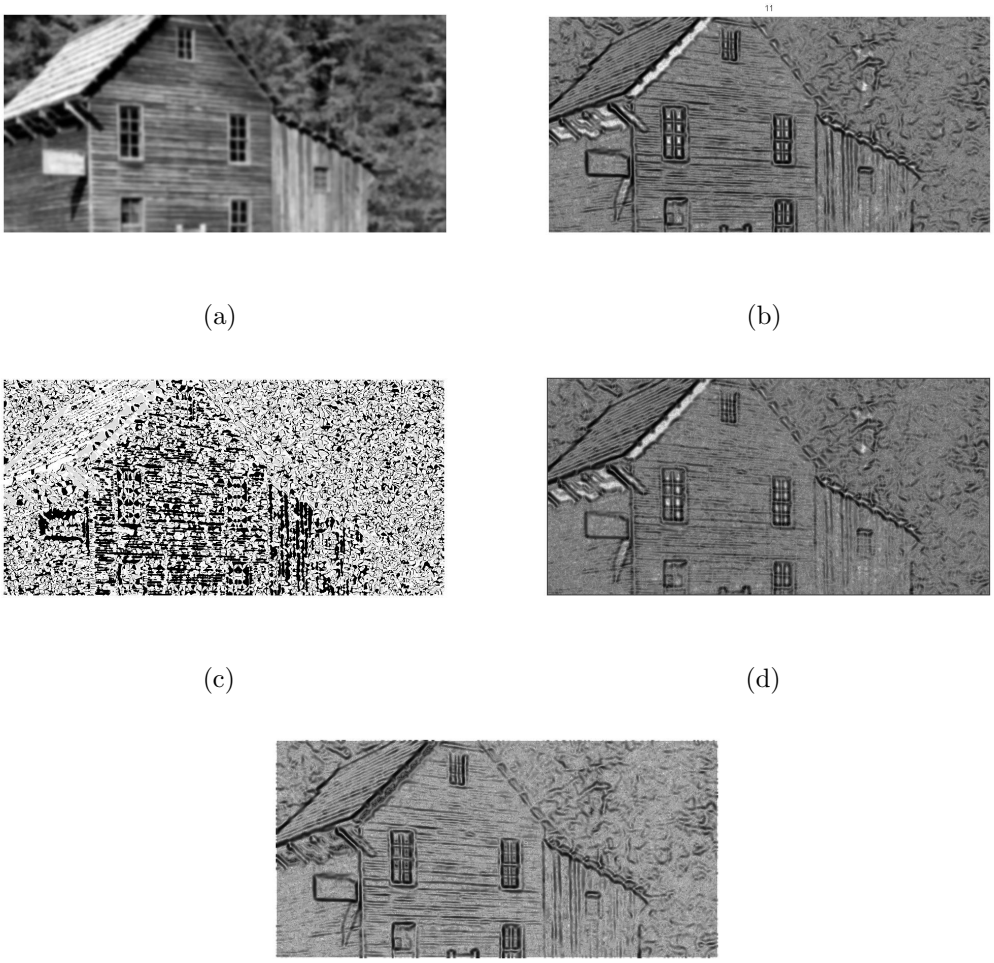

(a) (b)

(c) (d)

(e)

Figure 6.9: 11^{th} iteration of the AT equation with u and v feedback. (a) u^{n+1}. (b) v^n. (c) $vRef$. (d) Feedback term. (e) v^{n+1}.

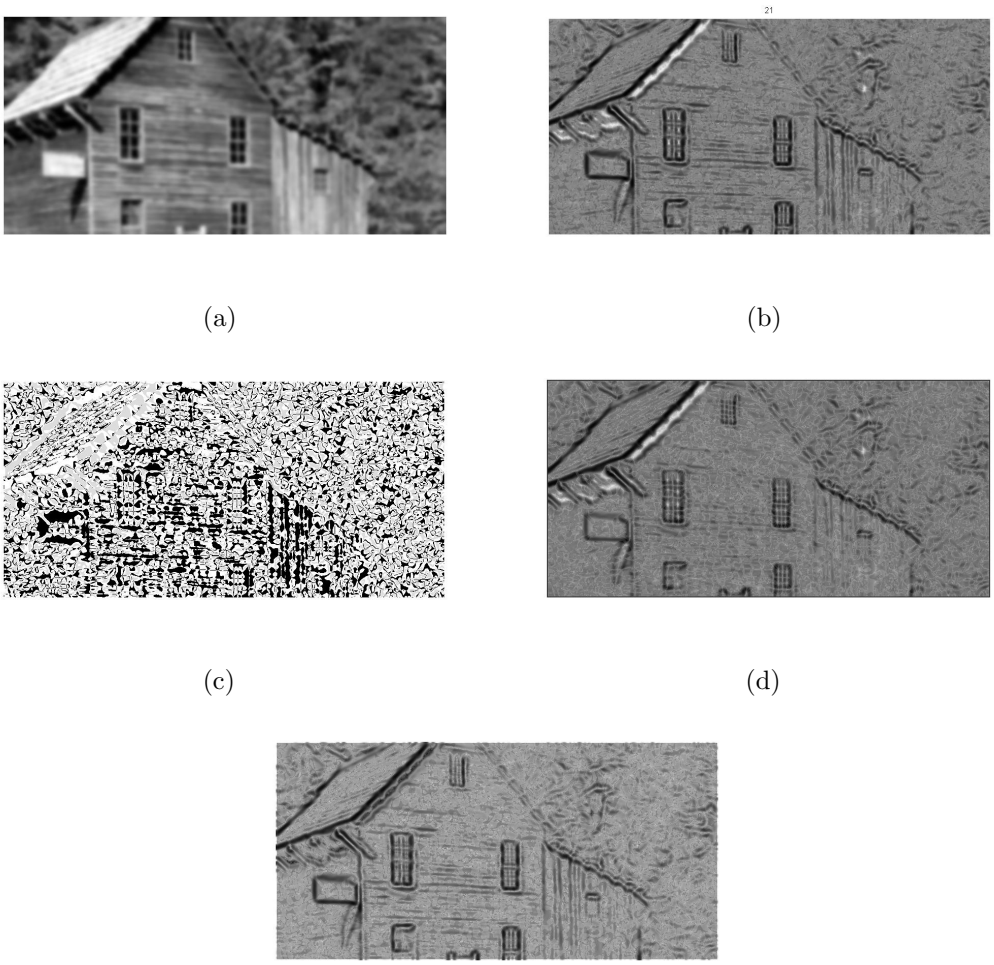

(a) (b)

(c) (d)

(e)

Figure 6.10: 21^{st} iteration of the AT equation with u and v feedback. (a) u^{n+1}. (b) v^n. (c) $vRef$. (d) Feedback term. (e) v^{n+1}.

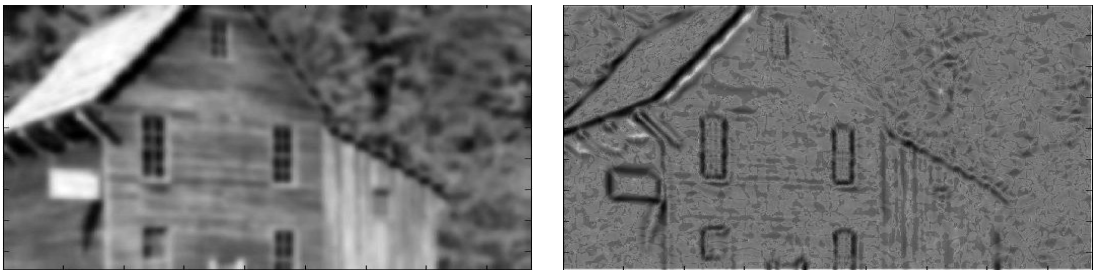

(a) (b)

Figure 6.11: AT segmentation with both u and v feedback (40 iterations). (a) u^{n+1}. (b) v^{n+1} ($\alpha = 1$, $\beta = 0.01$, $K_u = 10$, $K_v = 10000$) (431 s).

Since the directional information is lost in the feedback term associated with v variable, changing the orientation of the feedback kernel around a pixel does not change the feedback term at that pixel. Consequently, the feedback term does not serve as a local edge detector and meaningless segmentation results are obtained.

CHAPTER 7

CONCLUSION

In this thesis study, variational image segmentation methods have been studied. In a variational method, the image segmentation problem is posed in the form of minimizing an energy functional. The main variational model used for image segmentation in this study is the MS model. In this model, an image is decomposed into a set of regions by the requirement of homogeneity within regions. By minimizing the MS energy, a curve representing the edge set and an approximation of the original image, which is region-wise smooth, is computed. It is not straightforward to minimize the MS functional due to the existence of unknowns of different natures. On the other hand, there are two different kind of approximations to the MS functional which can be used in image segmentation: active contour implementations of the MS model and the AT functional.

The first approximation (the MS active contour method) minimizes the MS functional in two steps. In the first step, one eliminates the unknown approximating function from the functional by minimizing the functional with respect to the unknown approximating function while holding the edge set fixed. Then, the only unknown remaining in the functional is the edge set and minimization of the functional with respect to the edge set is a shape optimization problem which can be solved by level set methods. The CV method and the Tsai et. al.'s method are two good examples of this kind of MS approximations. Two-phase CV method simply decomposes the image into two regions with distinct mean intensities. For segmentation of complex images that consist of more than two regions in terms of mean intensity or that contain T-junctions, a four-phase CV scheme is used.

The CV active contour method is tested on synthetic and natural images. From the experiments, it can be concluded that the CV method is robust with respect to noise. Although, the CV active contour method is known to be better than edge-based active contour methods with respect to dependency on initialization; it is still affected by initial contour placement and may converge to an undesired local minima. The possibility of getting an undesired local minima is decreased by the initialization of the active contour with regularly spaced seeds. However, the CV model may stuck to an undesired local minima even in this case. Another result that can be obtained from the experiments is as follows: The assumption that image consists of two scales of intensity are not always satisfied in practice. Therefore in natural images, the performance of the algorithm is not as good as the performance in synthetic images.

Since the MS model segments the image by making use of the requirement of homogeneity within regions, active contour methods based on the MS model is not suitable for segmentation of textured images in which the piecewise smoothness assumption fails. Some extensions of active contour methods for textured image segmentation are also analyzed in this thesis study. Using nonlinear diffusion as a pre-filtering scheme for the CV active contour method, textures are smoothed out. For textured images which can be separated by image homogeneity requirement, results obtained using the pre-filtering scheme are better than the results obtained without using the pre-filtering scheme. However, if the objects belong to different texture classes but they have similar mean intensities, then the CV active contour method is unsuccessful for image segmentation even if the pre-filtering scheme is used.

In literature, there is an active contour method for texture segmentation based on the CV model and Gabor filters. In this method, a Gabor feature space of the image is constructed and a vector-valued CV active contour method segments the textured image. Even though, the selection Gabor filter parameters is not easy, automatic selection is possible by choosing the Gabor channels with maximum difference in terms of mean intensities of regions separated by the initial curve.

Textured image segmentation is not possible by the geodesic active contour method in which the edge detector function is defined as the inverse of the image gradient. However, there is an improved method in which the image is considered as a surface embedded in a 7-dimensional space constructed by Gabor filtering. Inverse of the determinant of the embedding space's metric can be used as an edge detector since this metric shows the rate of change of image intensity in a specific direction. But we did not get satisfactory results at this case. This is due to the low performance of this edge detector function on catching object boundaries.

The second technique is to use the Γ- convergence framework to approximate the MS functional with a functional which can be minimized in a standard way. One such functional is the AT functional. The lower dimensional variable representing the boundaries does not explicitly appear in this functional, instead the boundaries are represented by an edge detector function v which is near zero at edges and near one elsewhere.

Image segmentation experiments are done on noisy and textured images by using the AT model. As an approximation to the MS model, the difficulty of texture segmentation with the AT model is encountered when experiments on textured images are done. The reason behind that is the failure of piecewise smoothness assumption for these images. For an image containing salt and pepper noise, noise is eliminated by increasing smoothing radius of the AT model while losing some of the edges. The Shah's unified functional is used for image segmentation and smoothing and the effectiveness of the Shah's functional for obtaining objects boundaries without being misguided by noise in the image is observed. However, the edge set obtained by the Shah model has some unintuitive details.

In this thesis, some new ideas are proposed in order to increase the performance of the AT model especially on textured images. These ideas are based on the control theory. The variables in PDE equations of the AT model can be treated as states and with an artificial feedback term, this equations can be controlled. An artificial input is fed back to the PDE equations in each pixel

and input minus the pixel value of u or v at that iteration is added to the right hand side of equation of u or v. The PDE equation associated with u function is controlled with a term that increases smoothing. The artificial input is the mean intensity of the 3-by-3 neighborhood of that pixel in this equation. If proportionality constant is chosen suitably, this approach is very similar to increasing v value in the PDE equation associated with u by 1. This approach eliminates some false edges at textured regions. However, it causes inter-regional blurring because real edges are also blurred by the increased smoothing. In addition, a simple scheme for controlling the PDE equation associated with v function is proposed. In this scheme, the reference function is a local edge detector. However, some difficulties are encountered. We should insert a feedback term only for the center pixel of the local neighborhood but by a local edge detector which simply depends on gradient, a 3-by-3 matrix is obtained. This matrix is multiplied element-by-element with a 3-by-3 Gaussian function. Then the sum of the resultant matrix's elements is used as the feedback term of the center pixel. This operation emphasizes feedback term's value at the center pixel; but, it does not keep the orientation of the matrix. As a result, the feedback value is obtained regardless of the orientation of the edge in local neighbourhood. The second problem is that by obtaining a local edge detector, it is very hard to discriminate texture. Experiments show the difficulty in controlling the AT equations to discriminate texture by simple local derivative operators. Therefore, it can be concluded that the usage of high-level information from the image is necessary for the usage of feedback operation effectively.

As a future work, some applications of image segmentation schemes can be investigated. For example, buildings on aerial images can be identified by the variational image segmentation methods studied in the thesis. In addition, the performance of the textured image segmentation method can be improved by the combination of the state-of-art methods for texture segmentation with the framework of active contour methods.

REFERENCES

[1] S. Geman and D. Geman, "Stochastic relaxation, gibbs distributions, and the bayesian restoration of images.," *IEEE Trans. Pattern Anal. Mach. Intell.*, vol. 6, pp. 721–741, 1984.

[2] D. Mumford and J. Shah, "Optimal approximation by piecewise smooth functions and associated variational problems," *Comm. Pure Appl. Math.*, vol. 42, pp. 577–685, 1989.

[3] J. Shi, J. Malik, "Normalized cuts and image segmentation.," *IEEE Trans. Pattern Anal. Mach. Intell.*, vol. 22, pp. 888–905, August 2000.

[4] M. Kass, A. Witkin, and D. Terzopoulos, "Snakes: Active contour models," *Inter. Journal Comp. Vision*, vol. 1, pp. 321–331, 1988.

[5] C. Xu and J. Jerry, "Snake, shape, and gradient vector flow," *IEEE Trans on Image Processing*, vol. 7, no. 3, pp. 359–369, 1998.

[6] S. Osher and J. Sethian, "Fronts propagation with curvature dependent speed: Algorithms based on Hamilton-Jacobi formulations," *Journal Comp. Physics*, vol. 79, pp. 12 – 49, 1988.

[7] V. Caselles, R. Kimmel, and G. Sapiro, "Geodesic active contour models," *Inter. Journal Comp. Vision*, vol. 22, pp. 61–79, 1997.

[8] T. F. Chan and L. Vese, "Active contours without edges," *IEEE Trans. Image Process.*, vol. 10, no. 2, pp. 266–277, Feb. 2001.

[9] A. Tsai, A. Yezzi, and A. Willsky, "Curve evolution implementation of the Mumford-Shah functional for image segmentation, denoising, interpolation,

and magnification," *IEEE Trans. Image Process.*, vol. 10, no. 8, pp. 1169–1186, 2001.

[10] L. Vese and T. Chan, "A multiphase level set framework for image segmentation using the Mumford and Shah model," *Inter. Journal Comp. Vision.*, vol. 50, no. 3, July 2002.

[11] S. Gao and T. Bui, "Image segmentation and selective smoothing by using Mumford-Shah model," *IEEE Trans. Image Process.*, vol. 14, no. 10, pp. 1537 – 1549, Oct. 2005.

[12] G. Aubert and P. Kornprobst, *Mathematical Problems in Image Processing. Partial Differential Equations and the Calculus of Variations.* Springer, 2001.

[13] V. M. Tortorelli and L. Ambrossio, "Approximation of functionals depending on jumps by elliptic functionals via Γ-convergence," *Comm. Pure Appl. Math*, vol. 43, no. 8, pp. 98–113, 1990.

[14] L. Rudin, S. Osher, and E. Fatemi, "Nonlinear total variation based noise removal algorithms," *Phys. D*, vol. 60, pp. 259–268, 1992.

[15] Y. Meyer, *Oscillating Patterns in Image Processing and Nonlinear Evoulution Equations.*, vol. 22. Amer. Math. Soc., 2001.

[16] L. A. Vese and S. J. Osher, "Image denoising and decomposition with total minimization and oscillatory functions.," *Journal Mathematical Imaging and Vision*, vol. 20, pp. 7–18, 2004.

[17] G. Gilboa, N. Sochen, and Y. Zeevi, "Variational denoising of partly textured images by spatially varying constraints.," *IEEE Trans. Image Process.*, vol. 15, no. 8, pp. 2281–2289, 2006.

[18] P. Perona and J. Malik, "Scale-space and edge detection using anisotropic diffusion," *IEEE Trans. Patern Anal. Machine Intel.*, vol. 12, no. 7, pp. 1169–1186, July 1990.

[19] F. Catte, P. L. Lions, J. M. Morel, and T. Coll, "Image selective smoothing and edge detection by nonlinear diffusion," *SIAM J. Numer. Anal.*, no. 1, pp. 182–193, 1992.

[20] J. Weickert, "Theoretical foundations of anistropic diffusion in image processing," in *Theoretical Foundations of Computer Vision, Computing Suppl.* (W. Kropatsch, R. Klette, and F. Solina, eds.), vol. 11, pp. 221–236, Wien: Springer, 1996.

[21] J. Weickert, "Design of nonlinear diffusion filters," in *Computer Vision and Applications: A Guide for Students and Practitioners* (B. Jähne and H. Haussecker, eds.), ch. 12, pp. 439–458, Academic Press, 2000.

[22] B. Sandberg, T. Chan, and L. Vese, "A level-set and gabor based active contour algorithm for segmenting textured images," Tech. Rep. 02-39, UCLA Comput. Appl. Math., 2002.

[23] C. Sagiv, N. A. Sochen, and Y. Zeevi, "Integrated Active Contours for Texture Segmentation," *IEEE Trans. Image Process.*, vol. 15, no. 6, pp. 1633–1646, 2006.

[24] M. Hintermuller and W. Ring, "An Inexact Newton-CG-Type Active Contour Approach for the Minimization of the Mumford-Shah Functional," *Journal Mathematical Imaging and Vision*, vol. 20, pp. 19–42, 2004.

[25] A. Tsai, *Curve evolution and estimation-theoretic techniques for image processing.* PhD thesis, Harvard-M.I.T. Division of Health Sciences and Technology, Aug 2000.

[26] A. Duramaz, "Image segmentation based on variational techniques." M.Sc. Thesis in Electrical and Electronics Engineering Department of Middle East Technical University, Sep 2006.

[27] T. F. Chan, B. Y. Sandberg, and L. Y. Vese, "Active Contours without

Edges for Vector-valued Images.," *Journal of Visual Communication and Image Representation*, vol. 11, pp. 130–141, 2000.

[28] N. A. Sochen, R. Kimmel, and R. Malladi, "A general framework for low level vision," *IEEE Trans. Image Process.*, vol. 7, pp. 310–318, 1998.

[29] A. S. Yılmaz, "Edge preserving smoothing with directional consistency.." M.Sc. Thesis in Computer Engineering Department of Middle East Technical University, June 2007.

[30] E. Erdem and S. Tarı, "Mumford Shah Regularizer with Contextual Feedback," *Journal Mathematical Imaging and Vision*, vol. 33, pp. 67–84, January 2009.

[31] J. Shah, "A common framework for curve evolution, segmentation and anisotropic diffusion," in *Proceedings of the IEEE Conference on Computer Vision and Pattern Recognition*, 1996.

[32] J. K. Kaufhold, *Energy Formulations of Medical Image Segmentations*. PhD thesis, Boston University, College of Engineering, 2001.

[33] J. Wang, "Stochastic relaxation on partitions with connected components and its application to image segmentation," *IEEE Trans. Patern Anal. Machine Intel.*, vol. 20, pp. 619–636, June 1998.

APPENDIX A

CALCULUS OF VARIATIONS

Calculus of variations is a branch of optimization dealing with the minimization of functionals. A functional is a mapping from set of functions to real numbers. In general, functionals are defined by definite integrals. In contrast, the aim of calculus is to find a point that minimizes a function.

In the calculus of variations, the differential equation (Euler-Lagrange equation) whose solution gives the extremal point of the given functional is derived from the optimality condition that the so called Gâteaux derivative must vanish for all test functions at the extremal point. The Gâteaux Derivative is defined as below in [12].

Definition: Gâteaux Derivative

Let X be a Banach space and $F : X \rightarrow R$. The directional derivative of F at u in the direction v is given by:

$$F'(u,v) = \lim_{\lambda \rightarrow 0^+} \frac{F(u+\lambda v) - F(u)}{\lambda}$$

if the limit exists. If there exists $\tilde{u} \in X'$ such that $F'(u,v) = \tilde{u}(v)$, $\forall v \in X$, then F is Gâteaux differentiable at u and we write $F'(u) = \tilde{u}$. If F is Gâteaux differentiable and if the problem $\inf_{v \in X} F(v)$ has a solution u, then we have $F'(u) = 0$. $F'(u) = 0$ is called the Euler-Lagrange equation. If F is convex, the solution u of $F'(u) = 0$ is a solution of the minimization problem.

APPENDIX B

CURVATURE

Curvature is the rate of turning of the tangential vector. The mathematical definitions are taken from [12].

B.1 Parametrized Curves

Curvature is defined for parametrized curves regardless of parametrization. Let $C(p) = (x_1(p), x_2(p))$ be a regular parametrized curve in $\mathbb{R}^2$, where p parametrizes the set of points on the curve where $0 \leq p \leq 1$.

Tangent vector is given by $T(p) = (x_1'(p),\, x_2'(p))$ and normal vector is given by $N(p) = (-x_2'(p),\, x_1'(p))$. Arc length is given by:

$$s(p) = \int_0^p \sqrt{(x_1'(r))^2 + (x_2'(r))^2}\, dr \tag{B.1}$$

To properly define curvature, for parametrization of the curve by s, we have $|T(s)| = 1$. The curvature tensor is defined by $\frac{dT(s)}{ds} = \frac{d^2x}{ds^2}(s)$. It can be shown that curvature tensor is collinear to $\frac{N(s)}{|N(s)|}$, i.e., $\frac{dT(s)}{ds} = \kappa(s)\frac{N(s)}{|N(s)|}$, where $\kappa(s)$ is the curvature and the radius of curvature is given by $\frac{1}{\kappa(s)}$.

Since $|T(s)| = 1$ we obtain the expression for curvature:

$$\kappa(p) = \frac{x_1'(p)x_2''(p) - x_2'(p)x_1''(p)}{\left(x_1'(p)^2 + x_2'(p)^2\right)^{3/2}} \tag{B.2}$$

Since $Tp = |Cp|Ts$, we obtain:

$$\frac{1}{\left|\frac{\partial C(p)}{\partial p}\right|}\frac{\partial}{\partial p}\left(\frac{\frac{\partial C(p)}{\partial p}}{\left|\frac{\partial C(p)}{\partial p}\right|}\right) = \kappa(p)\frac{N(p)}{|N(p)|} \tag{B.3}$$

B.2 Curves as Isolevel of a Function u

Let $x(s)$ be parametrized by its curvilinear abscissa such that it is k-level of function $u:\ \mathbb{R}^2 \rightarrow \mathbb{R}$, that is: $x(s) = \{x_1(s), x_2(s)\ ;\ u\left(x_1(s), x_2(s)\right) = k\}$.

By differentiating $u\left(x_1(s), x_2(s)\right) = k$ with respect to s we obtain:

$$x_1\prime(s)u_{x_1}, x_2\prime(s)u_{x_2} = 0 \tag{B.4}$$

where u_{x_1}denotes $\frac{\partial u}{\partial x_i}\left(x_1(s), x_2(s)\right)$. Therefore, the vectors $(x_1\prime(s), x_2\prime(s))$ and $(-u_{x_2}, u_{x_1})$ are collinear. For some λ, we have

$$\begin{cases} x_1\prime(s) = -\lambda u_{x_2} \\ \\ x_2\prime(s) = \lambda u_{x_1}. \end{cases} \tag{B.5}$$

Therefore, the vectors (u_{x_1}, u_{x_2}) and $(-u_{x_2}, u_{x_1})$ are respectively normal and tangent to the curve $x(s)$. Differentiating again equation B.4 with respect to s we have:

$$\left(x_1\prime(s)\right)^2 u_{x_1^2} + \left(x_2\prime(s)\right)^2 u_{x_2^2} + 2x_1'\left(s\right)x_2'\left(s\right)u_{x_1x_2} + x_1\prime\prime(s)u_{x_1}, x_2\prime\prime(s)u_{x_2} = 0$$

$$\lambda^2\left(u_{x_1}^2 u_{x_2^2} + u_{x_2}^2 u_{x_1^2} - 2u_{x_1}u_{x_2}u_{x_1x_2}\right) + \tfrac{1}{\lambda}\left(x_1\prime\prime\left(s\right)x_2\prime\left(s\right) - x_2\prime\prime\left(s\right)x_1\prime\left(s\right)\right) = 0$$

Since $|x\prime(s)| = 1$, we obtain form B.5 that $\lambda^2 = \frac{1}{|\nabla u|^2}$. With B.2, the expression of curvature is finally obtained as:

$$\kappa = \frac{\left(u_{x_1}\right)^2 u_{x_2^2} + \left(u_{x_2}\right)^2 u_{x_1^2} - 2u_{x_1}u_{x_2}u_{x_1x_2}}{\left(\left(u_{x_1}\right)^2 + \left(u_{x_2}\right)^2\right)^{3/2}} \tag{B.6}$$

or equivalently:

$$\kappa = div\left(\frac{\nabla u}{|\nabla u|}\right). \tag{B.7}$$

APPENDIX C

MINIMIZATION OF THE CHAN-VESE ENERGY

In this part of the Appendix, the Euler-Lagrange equations of the CV functional are determined. The term $\nu \int H_\epsilon(\phi)dx$ which penalizes the area inside the curve is added to the CV Functional, for the sake of completeness. The energy functional which uses regularized versions of Heaviside and Dirac functions is given below:

$$\begin{aligned} E_{CV}(c_1, c_2, \Phi) = \lambda_1 \int_\Omega |u_0 - c_1|^2 H_\epsilon(\phi)dxdy + \lambda_2 \int_\Omega |u_0 - c_2|^2 (1 - H_\epsilon(\phi))dxdy \\ + \mu(\int_\Omega \delta_\epsilon(\phi)|\nabla\phi|dxdy) + \nu \int_\Omega H_\epsilon(\phi)dxdy \end{aligned} \tag{C.1}$$

First step is trivial. In order to find c_1, c_2 values which minimize the above functional, it is necessary that partial derivatives of E_{CV} with respect to c_1, c_2 be equal to 0. We rewrite the functional in a suitable form for this purpose and find the partial derivatives:

$$\begin{aligned} E_{CV}(c_1, c_2, \Phi) = \mu(\int_\Omega \delta_\epsilon(\phi)|\nabla\phi|dxdy) + \nu \int H_\epsilon(\phi)dxdy \\ + \lambda_1 \left(c_1^2 \int_\Omega H_\epsilon(\phi)dxdy - 2c_1 \int_\Omega u_0 \, H_\epsilon(\phi)dxdy \right. \\ \left. + \lambda_1 \int_\Omega u_0^2 H_\epsilon(\phi)dxdy \right) \\ + \lambda_2 \left(c_2^2 \int_\Omega u_0 \, (1 - H_\epsilon(\phi))dxdy - 2c_2 \int_\Omega u_0 \, (1 - H_\epsilon(\phi))dxdy \right. \\ \left. + \lambda_2 \int_\Omega u_0^2 \, (1 - H_\epsilon(\phi))dxdy \right) \end{aligned}$$

$$\frac{\partial E_{CV}}{\partial c_1} = 0 \tag{C.2}$$

$$2c_1 \int_\Omega H_\epsilon(\phi)dx - 2\int_\Omega u_0\ H_\epsilon(\phi)dxdy = 0 \Rightarrow$$

$$c_1(\phi) = \frac{\int_\Omega u_0 H_\epsilon(\phi)dxdy}{\int_\Omega H_\varepsilon(\phi)dxdy} \tag{C.3}$$

$$\frac{\partial E_{CV}}{\partial c_2} = 0 \tag{C.4}$$

$$2c_2 \int_\Omega (1 - H_\epsilon(\phi))\, dx - 2\int_\Omega u_0\ (1 - H_\epsilon(\phi))\, dxdy = 0 \Rightarrow$$

$$c_2(\phi) = \frac{\int_\Omega u_0\,(1 - H_\epsilon(\phi))\, dxdy}{\int_\Omega (1 - H_\varepsilon(\phi))\, dxdy} \tag{C.5}$$

Above equations show that the optimal values of c_1 and c_2 are given by mean intensities in the corresponding regions.

In second step, E_{CV} is minimized with respect to ϕ, keeping c_1 and c_2 fixed by formal methods of calculus of variations. Let ψ be a test function of the same type as ϕ. Gâteaux derivative of the terms in the functional in direction ψ are easily obtained by using Taylor's theorem as shown below:

$$lim_{t\to 0}\nu \int_\Omega \left(\frac{H_\epsilon(\phi + t\psi) - H_\epsilon(\phi)}{t}\right) dxdy$$

$$= lim_{t\to 0}\nu \int_\Omega \frac{H_\epsilon(\phi) + \frac{\partial H\epsilon(\phi)}{\partial\phi} \bullet t\psi + \mathcal{O}(t^2) - H_\epsilon(\phi)}{t} dxdy$$

$$= \int_\Omega H_\epsilon(\phi)'\psi dxdy$$

$$lim_{t\to 0}\lambda_1 \int_\Omega |u_0 - c_1|^2 \left(\frac{H_\epsilon(\phi + t\psi) - H_\epsilon(\phi)}{t}\right) dxdy$$

$$= lim_{t\to 0}\lambda_1 \int_\Omega |u_0 - c1|^2 \frac{H_\epsilon(\phi) + \frac{\partial H\epsilon(\phi)}{\partial\phi} \bullet t\psi + \mathcal{O}(t^2) - H_\epsilon(\phi)}{t} dxdy$$

$$= \lambda_1 \int_\Omega |u_0 - c_1|^2 H_\epsilon'(\phi)\psi dxdy$$

$$lim_{t\to 0}\lambda_2 \int_\Omega |u_0 - c_2|^2 \left(\frac{(1 - H_\epsilon(\phi + t\psi)) - (1 - H_\epsilon(\phi))}{t}\right) dxdy$$

$$= lim_{t\to 0}\lambda_1 \int_\Omega |u_0 - c_1|^2 \frac{-H_\epsilon(\phi) - \frac{\partial H\epsilon(\phi)}{\partial\phi} \bullet t\psi - \mathcal{O}(t^2) + H_\epsilon(\phi)}{t} dxdy$$

$$= -\lambda_2 \int_\Omega |u_0 - c_2|^2 H_\epsilon'(\phi)\psi dxdy$$

Gâteaux derivative of $\mu(\int_\Omega \delta_\epsilon(\phi)|\nabla\phi|dx)$ in direction ψ is

$$lim_{t\to 0}\mu\left(\frac{\int \delta_\epsilon\left(\phi+t\psi\right)|\nabla\left(\phi+t\psi\right)|dxdy-\int \delta_\epsilon\left(\phi\right)|\nabla\left(\phi\right)|dxdy}{t}\right)$$

which is equivalent to

$$\frac{\int_\Omega\left(\delta_\epsilon\left(\phi+t\psi\right)|\nabla\left(\phi+t\psi\right)|-\delta_\epsilon\left(\phi\right)|\nabla\left(\phi+t\psi\right)|+\delta_\epsilon\left(\phi\right)|\nabla\left(\phi+t\psi\right)|-\delta_\epsilon\left(\phi\right)|\nabla\left(\phi\right)|\right)dxdy}{t}.$$

Gâteaux derivative of $\mu(\int_\Omega \delta_\epsilon(\phi)|\nabla\phi|dx)$ is found by finding Gâteaux derivative of first two terms and last two last terms.

$$\begin{aligned}
&lim_{t\to 0}\int_\Omega\left(\frac{\delta_\epsilon\left(\phi+t\psi\right)-\delta_\epsilon\left(\phi\right)}{t}\right)|\nabla\left(\phi+t\psi\right)|dxdy\\
&\quad=lim_{t\to 0}\int_\Omega\frac{\delta_\epsilon\left(\phi\right)+\frac{\partial\delta\epsilon(\phi)}{\partial\phi}\bullet t\psi+\mathcal{O}\left(t^2\right)-\delta_\epsilon\left(\phi\right)}{t}|\nabla\left(\phi+t\psi\right)|dxdy\\
&\quad=\int\delta\epsilon'(\phi)\psi|\nabla\phi|dxdy
\end{aligned}$$

$$\begin{aligned}
&lim_{t\to 0}\int_\Omega\left(\frac{|\nabla\left(\phi+t\psi\right)|-|\nabla\left(\phi\right)|}{t}\right)\delta_\epsilon\left(\phi\right)dxdy\\
&\quad=lim_{t\to 0}\int_\Omega\frac{|\nabla\left(\phi\right)|+\frac{\partial|\nabla\phi|}{\partial(\nabla\phi)}\bullet t\nabla\psi+\mathcal{O}\left(t^2\right)-|\nabla\phi|}{t}\delta_\epsilon\left(\phi\right)dxdy\\
&\quad=\int_\Omega\delta_\epsilon\left(\phi\right)\frac{\langle\nabla\phi,\nabla\psi\rangle}{|\nabla\phi|}dxdy
\end{aligned}$$

Therefore,

$$\begin{aligned}
&lim_{t\to 0}\mu\left(\frac{\int_\Omega\delta_\epsilon\left(\phi+t\psi\right)|\nabla\left(\phi+t\psi\right)|dxdy-\int_\Omega\delta_\epsilon\left(\phi\right)|\nabla\phi|dxdy}{t}\right)\\
&\quad=\mu\int_\Omega\left(\delta\epsilon'(\phi)\psi|\nabla\phi|+\delta_\epsilon\left(\phi\right)\frac{\langle\nabla\phi,\nabla\psi\rangle}{|\nabla\phi|}\right)dxdy
\end{aligned}$$

Applying Green's formula [1] to convert the term containing $\nabla\psi$ to the form involving ψ, where n represents the exterior unit normal to the boundary, $\partial\Omega$ we get:

$$\mu\int_{\Omega}\delta\left(\phi\right)\frac{\langle\nabla\phi,\nabla\psi\rangle}{|\nabla\phi|}dxdy=\int_{\partial\Omega}\mu\frac{\delta_{\epsilon}(\phi)}{|\nabla\phi|}\frac{\partial\phi}{\partial n}\bullet\psi ds-\int_{\Omega}\mu\nabla\left(\delta_{\epsilon}\left(\phi\right)\frac{\nabla\phi}{|\nabla\phi|}\right)\psi dxdy. \tag{C.6}$$

Then, by expanding brackets in $\nabla\bullet\left(\delta_{\epsilon}\left(\phi\right)\frac{\nabla\phi}{|\nabla\phi|}\right)$, we obtain $\delta_{\epsilon}\prime\left(\phi\right)\frac{\langle\nabla\phi,\nabla\phi\rangle}{|\nabla\phi|}+\delta_{\epsilon}\left(\phi\right)\nabla\bullet\left(\frac{\nabla\phi}{|\nabla\phi|}\right)$, or $\delta_{\epsilon}\prime\left(\phi\right)|\nabla\phi|+\delta_{\epsilon}\left(\phi\right)\nabla\bullet\left(\frac{\nabla\phi}{|\nabla\phi|}\right)$ in the simplified form. Then,

$$\begin{aligned}lim_{t\rightarrow0}\mu\left(\frac{\int_{\Omega}\delta_{\epsilon}\left(\phi+t\psi\right)|\nabla\left(\phi+t\psi\right)|dxdy-\int_{\Omega}\delta_{\epsilon}\left(\phi\right)|\nabla\phi|dxdy}{t}\right)\\=\mu\int_{\Omega}\left(-\delta_{\epsilon}\left(\phi\right)\nabla\bullet\left(\frac{\nabla\phi}{|\nabla\phi|}\right)\right)\psi dxdy\\+\int_{\partial\Omega}\mu\frac{\delta_{\epsilon}(\phi)}{|\nabla\phi|}\frac{\partial\phi}{\partial n}\bullet\psi ds\end{aligned}$$

Hence, Gâteaux derivative of the CV functional is obtained as:

$$\begin{aligned}\int_{\Omega}\delta_{\epsilon}(\phi)\left(\mu\nabla\bullet\left(\frac{\nabla\phi}{|\nabla\phi|}\right)+\nu-\lambda_{1}\left|u_{0}-c_{1}\right|^{2}+\lambda_{2}\left|u_{0}-c_{2}\right|^{2}\right)\psi dxdy+\\\int_{\partial\Omega}\mu\frac{\delta_{\epsilon}(\phi)}{|\nabla\phi|}\frac{\partial\phi}{\partial n}\psi ds=0.\end{aligned} \tag{C.7}$$

Firstly, taking ψ to be nonzero near one point of Ω, zero elsewhere and taking limit over such ψ, secondly taking ψ to be nonzero near one point of $\partial\Omega$, zero elsewhere and taking limit over such ψ, the Euler-Lagrange equations for the CV functional are derived as below with the associated Neumann boundary conditions:

$$\delta_{\epsilon}(\phi)\left(\mu\nabla\bullet\left(\frac{\nabla\phi}{|\nabla\phi|}\right)+\nu-\lambda_{1}\left|u_{0}-c_{1}\right|^{2}+\lambda_{2}\left|u_{0}-c_{2}\right|^{2}\right)=0\quad in\ \Omega \tag{C.8}$$

$$\mu\frac{\delta_{\epsilon}(\phi)}{|\nabla\phi|}\frac{\partial\phi}{\partial n}=0\quad on\ \partial\Omega \tag{C.9}$$

[1] Let $\Omega\subset\mathbb{R}^{2}$, c, u, $v:\Omega\rightarrow\mathbb{R}$, and n denote the outer normal to $\partial\Omega$. A useful formula for integration by parts in two-dimensions is given by this form of Green's formula (based on the Green's theorem) : $\int_{\Omega}c\left\langle\nabla u,\nabla v\right\rangle dx=-\int_{\Omega}v\nabla\bullet\left(c\nabla u\right)dx+\int_{\partial\Omega}\left(c\frac{\partial u}{\partial n}\right)vds$.

APPENDIX D

FIRST VARIATION OF REGION INTEGRALS

In this part of Appendix, the variation of region integrals of the form

$$K = \int_{\omega(\vec{C})} \mathcal{H} dxdy \tag{D.1}$$

is determined, where $\vec{\mathcal{C}}$ represents a closed curve, ω represents region inside of $\vec{\mathcal{C}}$ and $\mathcal{H} : \mathbb{R}^2 \rightarrow \mathbb{R}$ denotes a continuous scalar field. Let $\overrightarrow{C} = \overrightarrow{C}(p,t)$ be a family of closed curves where t parametrizes the family and p parametrizes the set of points on the curve where $0 \leq p \leq 1$. Since the curve is closed, $\overrightarrow{C}(0,t) = \overrightarrow{C}(1,t)$ and $\overrightarrow{C_t}(0,t) = \overrightarrow{C_t}(1,t)$.

In order to derive first derivation of region integrals, we define $\overrightarrow{F}$ as,

$$\overrightarrow{F} = \begin{bmatrix} \int_0^x \mathcal{H}(\lambda, y) dxdy \\ \int_0^y \mathcal{H}(x, \lambda) dxdy \end{bmatrix}$$

so that $\nabla \cdot \overrightarrow{F} = 2\mathcal{H}$.

We rewrite equation (D.1) as

$$K = \frac{1}{2} \int_{\omega(\vec{C})} \nabla \cdot \overrightarrow{F} dxdy \tag{D.2}$$

From the divergence theorem, the equation (D.2) is rewritten as

$$K(t) = \frac{1}{2} \oint_C \left\langle \overrightarrow{F}, \overrightarrow{N} \right\rangle ds. \tag{D.3}$$

By relation $ds = \left\| \overrightarrow{Cp} \right\| dp$ between arc length term, ds and its parametrized version, dp, the equation (D.3) is rewritten as a function of t along the integral around $\overrightarrow{C}(p,t)$:

$$K = \frac{1}{2}\int_0^1 \left\langle \overrightarrow{F}, \overrightarrow{N} \left\| \overrightarrow{Cp} \right\| \right\rangle dp \tag{D.4}$$

Defining 90 degree rotation matrix Q as

$$Q = \begin{bmatrix} 0 & 1 \\ -1 & 0 \end{bmatrix}$$

and observing that $Q\overrightarrow{C_p} = \overrightarrow{N}\left\|\overrightarrow{Cp}\right\|$, a suitable form for further operations is obtained and its derivative with respect to t is obtained as:

$$K_t = \frac{1}{2}\int_0^1 \left(\left\langle \overrightarrow{F_t}, Q\overrightarrow{C_p} \right\rangle + \left\langle \overrightarrow{F}, Q\overrightarrow{C_{pt}} \right\rangle dp \right) \tag{D.5}$$

For second part integral above, we use integration by parts and use the property that $\overrightarrow{C_t}(0,t) = \overrightarrow{C_t}(1,t)$ and we obtain

$$K_t = \frac{1}{2}\int_0^1 \left(\left\langle \overrightarrow{F_t}, Q\overrightarrow{C_p} \right\rangle - \left\langle \overrightarrow{F_p}, Q\overrightarrow{C_t} \right\rangle dp \right) \tag{D.6}$$

If we represent 2 by 2 Jacobian matrix by J, the first term of $\overrightarrow{F}$ by F_1 and the second term of by of $\overrightarrow{F}$ by F_2, using the chain rule F_t and F_p can be expressed as:

$$\overrightarrow{F_t} = \begin{bmatrix} \frac{\partial F_1}{\partial x}\frac{\partial x}{\partial t} + \frac{\partial F_1}{\partial y}\frac{\partial y}{\partial t} \\ \frac{\partial F_2}{\partial x}\frac{\partial x}{\partial t} + \frac{\partial F_2}{\partial y}\frac{\partial y}{\partial t} \end{bmatrix} = (J\overrightarrow{F})\overrightarrow{C_t} \tag{D.7}$$

$$\overrightarrow{F_p} = \begin{bmatrix} \frac{\partial F_1}{\partial x}\frac{\partial x}{\partial p} + \frac{\partial F_1}{\partial y}\frac{\partial y}{\partial p} \\ \frac{\partial F_2}{\partial x}\frac{\partial x}{\partial p} + \frac{\partial F_2}{\partial y}\frac{\partial y}{\partial p} \end{bmatrix} = (J\overrightarrow{F})\overrightarrow{C_p} \tag{D.8}$$

Using (D.7) and (D.8), by rearrangements and simplifications, we obtain:

$$
\begin{aligned}
K_t &= \frac{1}{2}\int_0^1 \left\langle (J\overrightarrow{F})\overrightarrow{C_t}, Q\overrightarrow{C_p}\right\rangle - \left\langle (J\overrightarrow{F})\overrightarrow{C_p}, Q\overrightarrow{C_t}\right\rangle dp \\
&= \frac{1}{2}\int_0^1 \left\langle \overrightarrow{C_t}, \left[\left(Q^T(J\overrightarrow{F})\right)^T - \left(Q^T(J\overrightarrow{F})\right)\right]\overrightarrow{C_p}\right\rangle dp \qquad \text{(D.9)} \\
&= \frac{1}{2}\int_0^1 \left\langle \overrightarrow{C_t}, \left(\begin{bmatrix} -\frac{\partial F_2}{\partial x} & \frac{\partial F_1}{\partial x} \\ -\frac{\partial F_2}{\partial y} & \frac{\partial F_1}{\partial y}\end{bmatrix} - \begin{bmatrix} -\frac{\partial F_2}{\partial x} & -\frac{\partial F_2}{\partial y} \\ \frac{\partial F_1}{\partial x} & \frac{\partial F_1}{\partial y}\end{bmatrix}\right)\overrightarrow{C_p}\right\rangle dp \qquad \text{(D.10)} \\
&= \frac{1}{2}\int_0^1 \left\langle \overrightarrow{C_t}, \left(\left(\frac{\partial F_1}{\partial x} + \frac{\partial F_2}{\partial y}\right)\begin{bmatrix} 0 & 1 \\ -1 & 0\end{bmatrix}\right)\overrightarrow{C_p}\right\rangle dp \qquad \text{(D.11)} \\
&= \frac{1}{2}\int_0^1 \left\langle \overrightarrow{C_t}, \left(\nabla\cdot\overrightarrow{F}\right)Q\overrightarrow{C_p}\right\rangle dp \qquad \text{(D.12)}
\end{aligned}
$$

By the relation $\nabla\cdot\overrightarrow{F} = 2\mathcal{H}$, further simplifications can be done and the derivative of K with respect to t can be found as:

$$
\begin{aligned}
K_t &= \int_0^1 \left\langle \overrightarrow{C_t}, \mathcal{H}\overrightarrow{N}\right\rangle \left\|\overrightarrow{Cp}\right\| dp \\
&= \int_0^1 \left\langle \overrightarrow{C_t}, \mathcal{H}\overrightarrow{N}\right\rangle ds \qquad \text{(D.13)}
\end{aligned}
$$

It can be concluded from D.13 that K decreases most rapidly if $\overrightarrow{C_t} = -\mathcal{H}\overrightarrow{N}$.

APPENDIX E

FIRST VARIATION OF ARC-LENGTH

In this part of the Appendix, the variation of length functionals of the form

$$K(t) = \oint_{\vec{C}} ds \tag{E.1}$$

is determined, where $\vec{\mathcal{C}}$ denotes a closed curve, and $\mathcal{H} : \mathbb{R}^2 \rightarrow \mathbb{R}$ denotes a continuous scalar field. Let $\overrightarrow{C} = \overrightarrow{C}(p,t)$ be a family of closed curves where t parametrizes the family and p parametrizes the set of points on the curve where $0 \leq p \leq 1$. Since the curve is closed, we assume that $\overrightarrow{C}(0,t) = \overrightarrow{C}(1,t)$ and $\overrightarrow{C_t}(0,t) = \overrightarrow{C_t}(1,t)$. If we denote unit normal to the curve by $\overrightarrow{N}$, the integral in (E.1) is equivalent to:

$$K(t) = \oint_{C} \left\langle \overrightarrow{N}, \overrightarrow{N} \right\rangle ds \tag{E.2}$$

By the relation $ds = \left\| \overrightarrow{Cp} \right\| dp$ between arc length term ds and its parametrized version dp, we rewrite equation the (E.2) as a function of t along the integral around $\overrightarrow{C}(p,t)$:

$$K = \int_0^1 \left\langle \overrightarrow{N}, \overrightarrow{N} \left\| \overrightarrow{Cp} \right\| \right\rangle dp \tag{E.3}$$

Using the same procedure and notation in Appendix E, K_t is found as

$$K_t = \int_0^1 \left\langle \overrightarrow{C_t}, \left(\nabla \cdot \overrightarrow{N} \right) \overrightarrow{N} \right\rangle ds. \tag{E.4}$$

It can be concluded from E.4 that K decreases most rapidly if $\overrightarrow{C_t} = -\left(\nabla \cdot \overrightarrow{N} \right) \overrightarrow{N}$. Since $\kappa = div \left(\frac{\nabla \phi}{\|\nabla \phi\|} \right)$, $\overrightarrow{C_t} = -\kappa \overrightarrow{N}$ defines a gradient flow.

APPENDIX F

MINIMIZATION OF AMBROSIO-TORTORELLI ENERGY

In order to find the minimum of the AT energy functional with respect to u, the Gâteaux derivative of the AT functional at u should be zero where δu represents a function of the same type as u:

$$\lim_{t\to 0}\frac{E_{AT}(u+t\delta u,v)-E_{AT}(u,v)}{t}=0. \tag{F.1}$$

The Gâteaux derivative of the first term in the AT functional is given by

$$\lim_{t\to 0}\int_{\Omega}\beta\left(\left(u+t\delta u-u_0\right)^2-\left(u-u_0\right)^2\right)dx. \tag{F.2}$$

Since $\left(u+t\delta u-u_0\right)^2=\left(u-u_0\right)^2+2t\left(u-u_0\right)\delta u+\left(t\delta u\right)^2$, taking limit we get:

$$\lim_{t\to 0}\int_{\Omega}\frac{\beta\left(\left(u+t\delta u-u_0\right)^2-\left(u-u_0\right)^2\right)}{t}dx=\beta\int_{\Omega}2t\left(u-u_0\right)\delta u. \tag{F.3}$$

For the second term we find Gâteaux derivative by

$$\lim_{t\to 0}\alpha\int_{\Omega}\frac{\left(v^2\left(\left|\nabla u+\nabla\left(t\delta u\right)\right|^2-\left|\nabla u\right|^2\right)\right)}{t}dx \tag{F.4}$$

where $\left|\nabla u+\nabla\left(t\delta u\right)\right|^2=\left(u_x+t\delta u_x\right)^2+\left(u_y+t\delta u_y\right)^2$ and $\left|\nabla u\right|^2=u_x^2+u_y^2$. Expanding the squares, we get

$$\lim_{t\to 0}\alpha\int_{\Omega}\frac{\left(v^2\left(u_x^2+2tu_x\delta u_x+t^2\delta u_x^2+u_y^2+2tu_y\delta u_y+t^2\delta u_y^2-u_x^2-u_y^2\right)\right)}{t}dx \tag{F.5}$$

Taking limit, we obtain $\alpha\int_{\Omega}2\left\langle v^2\nabla u,\nabla\delta u\right\rangle dx$.

Applying Green's formula (see the footnote in Appendix C) where n denotes the exterior normal to the boundary $\partial\Omega$ we get

$$\alpha \int_{\Omega} 2 \left\langle v^2 \nabla u, \nabla \delta u \right\rangle dx = -2\alpha \int_{\Omega} \nabla \bullet \left(v^2 \nabla u \right) \delta u dx + 2\alpha \int_{\partial\Omega} v^2 \frac{\partial u}{\partial n} \delta u ds. \quad \text{(F.6)}$$

Other terms do not depend on u. For $\forall \delta u$, $\lim_{t \to 0} \frac{E_{AT}(u + t\delta u, v) - E_{AT}(u,v)}{t} = 0$ holds, therefore

$$\nabla \bullet (v^2 \nabla u) - \frac{\beta}{\alpha}(u - u_0) = 0 \; in \; \Omega \quad \text{(F.7)}$$

$$\left. \frac{\partial u}{\partial n} \right|_{\partial\Omega} = 0. \quad \text{(F.8)}$$

These equations are solved by using the gradient descent technique. The PDE equation for minimizing the AT functional with respect to u is given in equation F.9. In addition, the equation F.10 is the Neumann boundary condition and the equation F.11 is the initial condition.

$$\frac{\partial u}{\partial t} = \nabla \bullet (v^2 \nabla u) - \frac{\beta}{\alpha}(u - u_0) \quad \text{(F.9)}$$

$$\left. \frac{\partial u}{\partial n} \right|_{\partial\Omega} = 0 \quad \text{(F.10)}$$

$$u(x, y, 0) = u_0 \quad \text{(F.11)}$$

In order to find the minimum of the AT functional with respect to v, the Gâteaux derivative of the AT functional at v should be zero where δv represents a function of the same type as v:

$$\lim_{t \to 0} \frac{E_{AT}(u, v + t\delta v) - E_{AT}(u, v)}{t} = 0. \quad \text{(F.12)}$$

The Gâteaux derivative of the second term in the AT functional at v is given by:

$$\lim_{t\to 0}\alpha\int_{\Omega}\frac{\left(\left|\nabla u\right|^{2}\left(\left(v+t\delta v\right)^{2}-v^{2}\right)\right)}{t}dx=2\alpha\int_{\Omega}\left(\left|\nabla u\right|^{2}v\delta v\right)dx \tag{F.13}$$

The Gateaux derivative of fourth term in the AT functional at v is given by:

$$\lim_{t\to 0}\frac{1}{2\rho}\int_{\Omega}\frac{\left(\left(1-v-t\delta v\right)^{2}-\left(1-v\right)^{2}\right)}{t}dx=\alpha\int_{\Omega}-\left(1-v\right)\delta v dx \tag{F.14}$$

Repeating the same procedure used in derivation of F.6, the Gâteaux derivative of the third term in the AT functional at v is found as

$$\lim_{t\to 0}\frac{1}{2}\rho\int_{\Omega}\left(\left|\nabla\left(v+t\delta v\right)\right|^{2}-\left|\nabla v\right|^{2}\right)dx=-\rho\int_{\Omega}\nabla\bullet\left(\nabla v\right)\delta v dx+\rho\int_{\partial\Omega}\frac{\partial v}{\partial n}\delta v ds \tag{F.15}$$

where n denotes the exterior normal to the boundary $\partial\Omega$.

Since for $\forall\ \delta v$, $\lim_{t\to 0}\frac{E_{AT}(u,v+t\delta v)-E_{AT}(u,v)}{t}=0$ should hold to get an extremal point of the functional, the Euler-Lagrange equation is obtained as follows: In Ω, $\rho\nabla^{2}v-2\alpha\left|\nabla u\right|^{2}v+\frac{1}{\rho}\left(1-v\right)=0$ and on $\partial\Omega$, $\frac{\partial v}{\partial n}=0$.

Applying the gradient descent technique, the PDE equation which minimizes the AT functional with respect to v is obtained as given in equation F.16. The chosen initial condition and boundary condition are given in equations F.17 and F.18, respectively.

$$\frac{\partial v}{\partial t}=\nabla^{2}v-\frac{2\alpha|\nabla u|^{2}v}{\rho}-\frac{v-1}{\rho^{2}} \tag{F.16}$$

$$v(x,y,0)=\frac{1}{1+2\alpha\rho\left|\nabla u_{0}\right|^{2}} \tag{F.17}$$

$$\left.\frac{\partial v}{\partial n}\right|_{\partial\Omega}=0 \tag{F.18}$$